Vortices in trapped bose - Einstein condensates

Brian Jackson

VORTICES IN TRAPPED BOSE-EINSTEIN CONDENSATES

Brian Jackson

A thesis submitted in partial fulfilment of the requirements
for the degree of Doctor of Philosophy at the
University of Durham

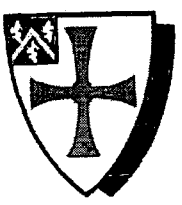

Department of Physics
University of Durham
September 2000

Vortices in Trapped Bose-Einstein Condensates

Brian Jackson

Abstract

In this thesis we solve the Gross-Pitaevskii equation numerically in order to model the response of trapped Bose-Einstein condensed gases to perturbations by electromagnetic fields. First, we simulate output coupling of pulses from the condensate and compare our results to experiments. The excitation and separation of eigenmodes on flow through a constriction is also studied.

We then move on to the main theme of this thesis: the important subject of quantised vortices in Bose condensates, and the relation between Bose-Einstein condensation and superfluidity. We propose methods of producing vortex pairs and rings by controlled motion of objects. Full three-dimensional simulations under realistic experimental conditions are performed in order to test the validity of these ideas. We link vortex formation to drag forces on the object, which in turn is connected with energy transfer to the condensate. We therefore argue that vortex formation by moving objects is intimately related to the onset of dissipation in superfluids. We discuss this idea in the context of a recent experiment, using simulations to provide evidence of vortex formation in the experimental scenario. Superfluidity is also manifest in the property of persistent currents, which is linked to vortex stability and dynamics. We simulate vortex line and ring motion, and find in both cases precessional motion and thermodynamic instability to dissipation.

Strictly speaking, the Gross-Pitaevskii equation is valid only for temperatures far below the BEC transition. We end the thesis by describing a simple finite-temperature model to describe mean-field coupling between condensed and non-condensed components of the gas. We show that our hybrid Monte-Carlo/FFT technique can describe damping of the lowest energy excitations of the system. Extensions to this model and future research directions are discussed in the conclusion.

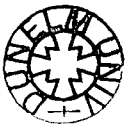

Acknowledgements

I owe a huge debt of gratitude to many people for their help and support over the course of my PhD. First of all I would like to thank Charles Adams, whose patient, insightful and enthusiastic supervision has made this work possible. I am also especially indebted to Jim McCann for his help, encouragement and for sharing his deep knowledge of science, and to Lydia Heck for maintaining the computers and unfailing assistance with my frequent computer problems. Thanks also to Thomas and Ifan for much help and many interesting discussions, to Mark for proof-reading, and to Richard and Hilary for (very) regular coffee breaks and for managing to put up with me for three years. Outside of work, I would especially like to thank Mark, Mark, Steve, Dave, Martin, Corinne, James, Adrian and Stephanie for many visits and top weekends away. Cheers also to Chris, Chris and Dave for being great house-mates, and to Paul for being such a good friend for so long.

Last but certainly not least, a big thanks to mam and dad and all of the family for their continued love, support and encouragement.

Contents

List of Figures

Statement of Copyright:

Chapter 1

Introduction

The first experimental observation of Bose-Einstein condensation (BEC) in magnetically trapped alkali atoms in 1995 [1, 2, 3] was a precursor to an explosion of interest in the properties of weakly-interacting Bose gases. The experimental progress since has been nothing short of spectacular [4, 5], not only in the expansion of the field to include many more groups from around the world (around twenty at the time of writing [6]), but also in the exciting avenues of research opened up, most notably in possibilities of constructing an atom laser and probing the fundamental nature of superfluidity. Theoretical understanding of Bose systems [7] has also been greatly enhanced by interaction with experiment and an influx of talented researchers from adjacent fields. Despite this, BEC still presents fresh challenges and opportunities, and one can be sure that many more surprises remain in the study of this rich system.

In several ways the first BEC experiments were a culmination of many years of experience in the fields of laser cooling and trapping of neutral atoms [8], and the search for BEC in spin-polarised hydrogen [9, 10]. From the former came methods for confining neutral alkali atoms, and cooling them to ultra-cold temperatures. To this one must add the atom optical techniques developed for manipulation of atomic clouds using electromagnetic fields that have proved so invaluable in BEC experiments, as will be discussed below. From the latter came the techniques of magnetic trapping and evaporative cooling [11, 12] where the most energetic atoms are selectively removed from the trap, potentially leading to the increase in phase-space density required to reach the BEC transition. The study of BEC itself possesses an illustrious history (see e.g. [13]) with roots in the original work of Bose and Einstein in the 1920s, and including the discovery of superfluidity in liquid helium. As this history has a direct bearing on the subject of this thesis, we shall now give a brief review.

Superfluidity and BEC

At very low temperatures helium possesses a unique property. Relatively weak interactions between atoms of small mass lead to helium remaining liquid at atmospheric pressure, even in the limit of absolute zero. Remarkable phenomena result, the most striking of which occurs for ^{4}He below a phase transition at $T_\lambda = 2.17\,\mathrm{K}$. This state, sometimes referred to as HeII, is marked by a complete lack of viscosity or thermal resistance, and was discovered in 1938 by Allen, Misener and Kapitza [14, 15]. Fritz London [16] immediately suggested a link between this *superfluid* phase and the work of S. N. Bose [17] and Einstein [18] on the quantum statistics of particles with integer spin. In contrast to Fermi-Dirac statistics, many bosons can occupy the same quantum state; moreover, bosons preferentially scatter into highly-occupied states. Thus, when the phase-space density is sufficiently high (or equivalently when $T < T_c$) bosons tend to congregate into a single state to form a Bose-Einstein condensate. The condensate exhibits long-range coherence, which is directly responsible for superfluidity. This picture was developed further by Tisza [19] and Landau [20] in the two-fluid model, which explained properties of HeII in terms of a condensate coupled to a 'non-condensed' or 'normal' fluid of quasiparticle excitations.

Particularly interesting in the context of our discussion is the response of superfluid helium to rotation and flow through a narrow constriction. In the former, the famous 'rotating bucket' experiment [21], one would expect that the irrotational superfluid would possess zero moment of inertia and remain stationary with respect to the laboratory frame. However, experiments demonstrate rigid-body rotation above some critical angular velocity. Similarly, in the case of superfluid flow through a channel dissipation is expected only above a critical velocity. According to Landau, viscosity in a quantum fluid arises due to the creation of elementary excitations (i.e. phonons and rotons), which occurs only when energetically favourable [20]. The critical velocity thus defined is found to be several orders of magnitude larger than that observed [22]. Feynman [23] explained both effects as arising due to the formation of quantised vortices. Superfluid rotation is accounted for by creation of a vortex lattice, which possesses a net angular velocity. In the latter case, dissipation arises from the motion of the vortices and their interaction with the normal component [24]. In both of the situations we have discussed, vortex formation may be thought of as being responsible for the 'breakdown' of superfluidity, revealing part of the fundamental nature of this phenomenon.

Problems arise when attempting to describe this vortex formation process in de-

tail. Although the two-fluid model is successful in explaining superfluid properties on a hydrodynamical level, for example in describing second sound [25], a satisfactory microscopic theory for ^{4}He is notoriously difficult to formulate. This is due to the strong interactions that result in an appreciable quantum depletion: indeed, typically only around 10% of atoms are in the condensate even at zero temperature [26]. In contrast, the fundamental many-body theory of BEC is well understood for a dilute, weakly-interacting system, where interactions can be treated within mean-field theory as a perturbation on the ideal gas case [27]. In particular, for such a system at very low temperatures where non-condensed atoms can be neglected, the condensate dynamics may be modelled using a nonlinear Schrödinger equation for the macroscopic wavefunction, or Gross-Pitaevskii (GP) equation [28, 29]. Fortunately, experiments on trapped alkali vapour condensates lie in this dilute, weakly-interacting regime, and evaporative cooling can be extended to obtain almost pure condensates. Thus, the GP equation provides an accurate description of trapped Bose condensates at low temperatures, and the system is ideal for elucidating some of the fundamental properties of quantum fluids.

It would be impossible to end a section concerning Bose-Einstein condensation without mentioning some of the other systems that display this phenomenon. Indeed, BEC is ubiquitous in nature, arising for example in neutron stars, amongst excitons in semiconductors, as a pairing of quarks and anti-quarks within elementary particles and the vacuum state, and as a BCS transition in ^{3}He [30]. In addition, a superconductor can be considered to be a Bose condensate of Cooper pairs of electrons, and shares many analogous features with superfluids (with additional complications due to the non-zero charge density). More generally, BEC is an example of a spontaneous symmetry-breaking phase transition, familiar in many areas of physics [31]. A particularly compelling example concerns the early universe. The phase transitions that accompanied symmetry-breaking as the universe cooled in the aftermath of the Big Bang may have been sufficiently rapid to produce topological defects. These include domain walls and cosmic strings (analogous to vortex lines in superfluids) which may have had a bearing on early structure formation. This process, known as the Kibble mechanism [32], is a subject of interest in liquid helium, where vortices are detected after a rapid quench though the phase transition [33]. Equivalent experiments have also been proposed in trapped Bose gases [34], though it remains to be seen whether this system can be used to shed further light on cosmology.

Trapped Bose-Einstein condensed gases

Apart from the existence of an accurate mean-field description, as mentioned in the previous section, a further advantage of trapped atomic systems is the wealth of techniques available to probe the condensate. The shape of the magnetic trap confining the atoms can be varied, allowing study of collective excitations of the condensate. Far-off resonance light has also been used to trap [35] and manipulate [4] condensates. For example, in a landmark experiment by Ketterle and co-workers at MIT [36], a condensate was split using the repulsive optical dipole force from a blue detuned laser, creating two independent condensates separated by an energy barrier. On release of the barrier interference fringes were observed, providing compelling evidence of long-range phase coherence in the condensate. Superfluidity is intimately linked to this phase coherence: indeed, the local superfluid velocity is proportional to the gradient of the phase.

Another enticing consequence of phase coherence is the possibility of constructing atom lasers. In analogy with optical lasers, the output consists of an intense beam of coherent atoms, or a matter wave. Potentially, this could revolutionise the field of atom optics. An atom laser requires two principal building blocks: a source of coherent atoms, and a way of extracting an output. The first output coupling scheme was developed at MIT [37] using radio-frequency (RF) radiation to excite a fraction of the atoms to an untrapped hyperfine level, where they were free to fall under gravity. This may be thought of as realising a simple pulsed atom laser, though subsequently more elaborate quasi-continuous schemes have been developed [38, 39]. RF radiation has also been of particular importance when creating multi-component condensates [35, 40, 41, 42]. Moreover, a modified form of this technique has been successfully employed to produce the first vortex state in a trapped Bose condensate [43, 44].

Structure of the thesis

In this thesis we shall explore some of the themes introduced in this chapter. In Chapter 2 we discuss the Gross-Pitaevskii equation within mean-field theory, and describe the numerical methods used to solve it. We utilise the GP equation to model condensate dynamics, in particular the output coupling of atoms [37] and flow through a constriction, where excited states can be created. This particular theme is developed further in Chapter 3, where we present simulations of flow of the condensate around an obstacle, formed for example using a focused far-off resonance

laser beam. We demonstrate vortex pair formation in both 2D and 3D simulations, and propose this mechanism as an experimental scheme to produce vortex lines. We also propose a method to create vortex ring states, whereupon two components of a trapped binary condensate mixture [40] are translated with respect to one another, as discussed in Chapter 4.

In Chapter 5 we discuss vortex line and ring dynamics in terms of the underlying fluid mechanics of the condensate, with particular reference to the Magnus force, and explain the observations of previous chapters in terms of this formalism. It also serves to introduce the concept of vortex energy, which is useful for the discussion in Chapter 6 of recent MIT observations [45] of condensate heating when perturbed by an oscillating laser beam. We explain the observed dissipation in terms of vortex formation above a critical velocity. This serves as a natural extension to the material of earlier chapters; however, the analysis is incomplete as strictly speaking simulations are valid only in the limit of zero temperature. We discuss in Chapter 7 a method to extend our simulations to finite temperatures, and apply it to model collective excitations. We finally conclude and highlight future research directions in Chapter 8.

The topics discussed in this thesis are also covered in the following publications:

B. Jackson, J. F. McCann, and C. S. Adams, "Vortex formation in inhomogeneous Bose-Einstein condensates," Phys. Rev. Lett. **80**, 3903 (1998).

B. Jackson, J. F. McCann, and C. S. Adams, "Output coupling and flow of a dilute Bose-Einstein condensate," J. Phys. B: At. Mol. Opt. Phys. **31**, 4489 (1998).

B. Jackson, J. F. McCann, and C. S. Adams, "Vortex rings and mutual drag in trapped Bose-Einstein condensates," Phys. Rev. A **60**, 4882 (1999).

B. Jackson, J. F. McCann, and C. S. Adams, "Vortex line and ring dynamics in trapped Bose-Einstein condensates," Phys. Rev. A **61**, 013604 (2000).

B. Jackson, J. F. McCann, and C. S. Adams, "Dissipation and vortex creation in Bose-Einstein condensed gases," Phys. Rev. A **61**, 051603(R) (2000).

Chapter 2

BEC and the Gross-Pitaevskii equation

Much of the theoretical work on weakly-interacting Bose condensates over the years has focused on solution of the Gross-Pitaevskii (GP) equation [7]. The long-range phase coherence fundamental to BEC allows a description in terms of a macroscopic wavefunction. The GP equation governs the evolution of this wavefunction at low temperatures, and follows from mean-field theory where interactions between atoms are modelled by a pseudopotential with an amplitude proportional to the s-wave scattering length. Early comparisons to experiment showed that the GP equation gives an accurate description of the shape [46] and dynamics [47, 48, 49, 50] of dilute condensates at low temperatures. As a result, the GP equation provides us with a powerful tool for elucidating the rich phenomena inherent in condensate dynamics. The present chapter introduces the equation and displays solutions in a 1D harmonic trap. We then discuss further applications concerning simulations of output coupling and flow through a constriction. First, however, we will discuss some of the more fundamental aspects of BEC.

2.1 Basic theory

2.1.1 Bose-Einstein condensation in an ideal gas

Quantum statistical mechanics divides the world into two types of particles: bosons, which possess integer spin; and fermions, which are characterised by half-integer spin. This results in widely divergent behaviour in the quantum degenerate regime where many particles can occupy a small region of phase space. Fermions obey the Pauli exclusion principle, where each quantum state may only be occupied by a maximum of one particle. This is fundamental to many diverse systems, ranging

from the structure of the atom to the structure of a white dwarf star. Bosons, in contrast, are subject to no such constraints, and in principle many particles can congregate into the same quantum state. In fact, Bose-Einstein statistics goes further in predicting that bosons will preferentially scatter into already highly-occupied states, an effect analogous to stimulated emission of light. As a result, macroscopic occupation of the lowest energy state is possible even at non-zero temperatures, on condition that the phase space density is sufficiently high. This phenomenon is known as Bose-Einstein condensation (BEC).

The transition temperature for BEC is readily calculated for an ideal, non-interacting system of particles. We start from the partition function for the grand canonical ensemble [31]:

$$Z_G = \mathrm{Tr}\left[e^{-\beta(\hat{H}-\mu\hat{N})}\right], \tag{2.1}$$

where μ is the chemical potential, while $\beta \equiv 1/k_B T$ is defined at the temperature T. Similarly, the Hamiltonian and number operator are represented by $\hat{H}$ and $\hat{N}$ respectively. Bose statistics and thermodynamic relations [27] yield the total number of atoms in terms of a sum over the mean occupation of states of energy ϵ_i:

$$N = \sum_i \frac{1}{\exp[\beta(\epsilon_i - \mu)] - 1}. \tag{2.2}$$

We now consider bosonic atoms confined within a trap. To a good approximation, the bottom (low energy region) of both magnetic and optical dipole traps is given by the harmonic form:

$$V_{\mathrm{trap}}(\mathbf{r}) = \frac{m}{2}(\omega_x^2 x^2 + \omega_y^2 y^2 + \omega_z^2 z^2). \tag{2.3}$$

Equation (2.2) now becomes a sum over eigenstates of the single-particle Hamiltonian, with energies:

$$\epsilon_{n_x,n_y,n_z} = \left(n_x + \frac{1}{2}\right)\hbar\omega_x + \left(n_y + \frac{1}{2}\right)\hbar\omega_y + \left(n_z + \frac{1}{2}\right)\hbar\omega_z. \tag{2.4}$$

In the classical limit, $-\beta\mu \to \infty$, yielding the usual Boltzmann distribution for (2.2). In the opposite limit, the population in the ground state becomes macroscopic when the chemical potential approaches the minimum energy, i.e. $\mu \to \mu_c = \epsilon_{000}$. Note that this differs from the case of a homogeneous system in the thermodynamic limit, where $\mu_c = 0$.

The number of particles outside the ground state in the quantum degenerate limit can now be calculated from (2.2) by replacing the discrete summation by an integral [7], which is valid under the assumption that the level spacing is much

smaller than the relevant excitation energies. Hence, this semi-classical approximation is expected to be good under the condition $k_B T \gg \hbar\bar{\omega}$, where $\bar{\omega}$ is the geometric mean of the trap frequencies, $\bar{\omega} = (\omega_x\omega_y\omega_z)^{1/3}$. Evaluating the integral then yields:

$$N - N_0 = \zeta(3)\left(\frac{k_B T}{\hbar\bar{\omega}}\right)^3, \tag{2.5}$$

where $\zeta(x)$ is the Riemann zeta function. The transition temperature T_c^0 readily follows by setting $N_0 = 0$:

$$k_B T_c^0 = \hbar\bar{\omega}\left(\frac{N}{\zeta(3)}\right)^{1/3}. \tag{2.6}$$

Inserting (2.6) into (2.5) gives the T dependence of the condensate fraction:

$$\frac{N_0}{N} = 1 - \left(\frac{T}{T_c^0}\right)^3. \tag{2.7}$$

The criterion (2.6) may be recast in terms of the phase space density, $n_0\lambda_T^3 > \zeta(3/2)$, where n_0 is the peak number density of the cloud whilst $\lambda_T = (2\pi\hbar^2/mk_BT)^{1/2}$ is the thermal wavelength. From this one realises the full scale of the task that faced experimenters when striving to obtain the first BEC in alkali vapours. Laser cooling techniques have been developed [8] with the ability to cool to sub-microkelvin temperatures. However, these optical schemes generally fail at the relatively high densities required for BEC due to reabsorption of spontaneously emitted photons and light-induced collisions, and conventional laser cooling schemes are typically only capable of reaching phase space densities five orders of magnitude away from quantum degeneracy.[1] Evaporative cooling bypasses these problems by using RF radiation to selectively induce spin flips in atoms at the edge of the trap. Atoms in a magnetic trap are spin-polarised in low-field seeking states, with those of highest energy tending to be found at the edge. Transitions to high-field seeking states expel these atoms, so that rethermalisation of the remaining atoms leads to a lower temperature. This technique eventually results in the required enhancement of phase space density with a relatively modest loss of atoms. In the first successful experiment on ^{87}Rb [1], condensation was achieved at $T_c \simeq 170\,\mathrm{nK}$ with $N \simeq 2 \times 10^4$ atoms, at a number density of $\sim 2.6 \times 10^{12}\,\mathrm{cm}^{-3}$. Subsequent experiments have produced condensates of up to $N \sim 10^7$ atoms at densities of around $10^{15}\,\mathrm{cm}^{-3}$ [6]. At these densities, interatomic collisions become increasingly important, with often

[1]Note that phase space densities of up to 0.1 have been achieved using special schemes, e.g. sub-recoil cooling or the intercombination transition in strontium (see [51] and references therein).

dramatic repercussions for the condensate properties. Fortunately, interactions remain sufficiently weak to allow a Hartree-Fock mean-field description, where each atom is treated as moving in a field composed of interactions with all of the other atoms, as will now be discussed.

2.1.2 The mean-field description and second quantisation

To simplify the discussion of the many-body problem, the method of second quantisation is often employed. In this formalism, field operators are defined as linear combinations of single-particle wavefunctions and creation and annihilation operators on the many-particle Hilbert space. The fields are written as $\hat{\psi}_\alpha(\mathbf{r})$, where α here represents any internal degrees of freedom (e.g. spin) while $\mathbf{r}$ indicates the position vector. Commutation and anti-commutation relations are satisfied: $[\hat{\psi}_\alpha(\mathbf{r}), \hat{\psi}^\dagger_\beta(\mathbf{r}')]_\mp = \delta_{\alpha\beta}\delta(\mathbf{r}-\mathbf{r}')$ and $[\hat{\psi}_\alpha(\mathbf{r}), \hat{\psi}_\beta(\mathbf{r}')]_\mp = 0$, where the upper (lower) sign refers to bosons (fermions). This highlights one of the major advantages of second quantisation, in that the quantum statistics is included in the field operator. We shall, however, restrict our attention to bosons here. Neglecting spin, the Hamiltonian of the system can be represented by:

$$\hat{H} = \int \mathrm{d}^3\mathbf{r}\, \hat{\psi}^\dagger(\mathbf{r}) \left[-\frac{\hbar^2}{2m}\nabla^2 + V_{\mathrm{trap}}(\mathbf{r}) \right] \hat{\psi}(\mathbf{r}) + \frac{1}{2}\int \mathrm{d}^3\mathbf{r}\, \mathrm{d}^3\mathbf{r}'\, \hat{\psi}^\dagger(\mathbf{r})\hat{\psi}^\dagger(\mathbf{r}')\mathcal{U}(\mathbf{r},\mathbf{r}')\hat{\psi}(\mathbf{r}')\hat{\psi}(\mathbf{r}), \tag{2.8}$$

where interactions between particles are represented by $\mathcal{U}(\mathbf{r},\mathbf{r}')$.

The single-particle density matrix can be expressed as a correlation function between fields at the points $\mathbf{r}$ and $\mathbf{r}'$:

$$\rho_1(\mathbf{r},\mathbf{r}') = \langle \hat{\psi}^\dagger(\mathbf{r})\hat{\psi}(\mathbf{r}') \rangle. \tag{2.9}$$

The diagonal elements simply give the density of the condensate, e.g. $\rho_1(\mathbf{r}) = |\psi(\mathbf{r})|^2$. However, the off-diagonal elements are of considerable interest in our discussion as they furnish the Penrose-Onsager criterion for Bose-Einstein condensation [30]:

$$\langle \hat{\psi}^\dagger(\mathbf{r})\hat{\psi}(\mathbf{r}') \rangle \overset{|\mathbf{r}-\mathbf{r}'|\to\infty}{\longrightarrow} \Psi^*(\mathbf{r})\Psi(\mathbf{r}'), \tag{2.10}$$

where $\Psi(\mathbf{r}) = \langle \hat{\psi}(\mathbf{r}) \rangle \neq 0$ is the condensate wavefunction, which is a complex number possessing a magnitude and phase. We see that the Hamiltonian (2.8) is invariant under a constant phase change of $\hat{\psi}(\mathbf{r})$; however, as the ensemble average of the field is non-zero, then a 'preferred' phase must be selected when the condensate forms. This concept is referred to as broken gauge symmetry. Furthermore, we see

that to satisfy the Penrose-Onsager criterion the phase of $\hat{\psi}(\mathbf{r})$ must be spatially correlated over the entire system. This phenomenon is known as off-diagonal long-range order (ODLRO).

In view of the previous discussion, the field operator can be written as a sum of the condensate wavefunction and an operator representing the non-condensed bosons:

$$\hat{\psi}(\mathbf{r}) = \Psi(\mathbf{r}) + \tilde{\psi}(\mathbf{r}), \tag{2.11}$$

where $\langle\tilde{\psi}(\mathbf{r})\rangle = 0$ by definition. Substituting into the density matrix (2.9) yields:

$$\rho_1(\mathbf{r},\mathbf{r}') = \Psi^*(\mathbf{r})\Psi(\mathbf{r}') + \langle\tilde{\psi}^\dagger(\mathbf{r})\tilde{\psi}(\mathbf{r}')\rangle. \tag{2.12}$$

We immediately see that a pure condensate exhibits perfect first order spatial coherence, which is related to its phase coherence over the entire system. Conversely, the non-condensate exhibits a rapid Gaussian decay to zero over a length scale equal to the thermal wavelength, λ_T [52, 53]. Thus, the off-diagonal elements of the density matrix tend at infinity to a value equal to the condensate fraction. A beautiful recent experiment [54] has demonstrated this by measuring the visibility of the interference pattern between two spatially separated regions of a trapped condensate.

2.1.3 The Gross-Pitaevskii equation

We now neglect the fluctuations of the field, and consider only the condensate wavefunction, $\Psi(\mathbf{r})$. This is valid near to $T = 0$ and for weak interactions, where the condensate depletion due to thermal and quantum fluctuations is negligible. In effect, this corresponds to treating the wavefunction as a classical field with well defined phase, though it remains 'quantum' in the sense that the wavefunction is still described by a Schrödinger equation. We discuss the generalisation to finite temperatures in Chapter 7.

A further approximation is to treat the interatomic potential as a hard-body sphere of infinitesimally small radius. This is valid for dilute condensates where the mean inter-particle separation far exceeds the range of interactions, also allowing us to treat only binary collisions. This assumption is a good one for the present BEC experiments. As we consider low temperatures, interatomic collisions are dominated by s-wave scattering. In this regime, the bosonic cross-section is $\sigma = 8\pi a^2$, where a is the scattering length. These assumptions allow us to treat interactions using a pseudopotential [55] of the form $\mathcal{U}(\mathbf{r},\mathbf{r}') = g\delta(\mathbf{r}-\mathbf{r}')$, with $g = 4\pi\hbar^2 a/m$.

Substitution into the Hamiltonian (2.8) yields:

$$\hat{H}(t) = \int \mathrm{d}^3\mathbf{r} \left(\Psi^*(\mathbf{r},t) \left[-\frac{\hbar^2}{2m}\nabla^2 + V_{\mathrm{trap}}(\mathbf{r},t) \right] \Psi(\mathbf{r},t) + \frac{g}{2}|\Psi(\mathbf{r},t)|^4 \right), \quad (2.13)$$

where we have re-introduced the time dependence. The evolution of the wavefunction is then found using the Heisenberg equation of motion for the field operator, $i\hbar\partial_t\hat{\psi} = [\hat{\psi}, \hat{H}]$. This gives:

$$i\hbar\frac{\partial}{\partial t}\Psi(\mathbf{r},t) = \left(-\frac{\hbar^2}{2m}\nabla^2 + V_{\mathrm{trap}}(\mathbf{r},t) + Ng|\Psi(\mathbf{r},t)|^2 \right) \Psi(\mathbf{r},t), \quad (2.14)$$

where we have renormalised Ψ to remove N, the number of atoms, in order that:

$$\int |\Psi|^2 \mathrm{d}^3\mathbf{r} = 1. \quad (2.15)$$

We see that (2.14) has the form of a Schrödinger equation, with an additional interaction term proportional to the number density, $n_c(\mathbf{r},t) = N|\Psi(\mathbf{r},t)|^2$. For this reason it is known as the time dependent nonlinear Schrödinger equation (NLSE), or Gross-Pitaevskii (GP) equation [28, 29].

2.2 Numerical solution of the GP equation

Given the GP equation (2.14), we now wish to solve it in order to determine the equilibrium properties of the condensate and to simulate the dynamics subject to a time dependent potential. In this section we describe the basic ideas underpinning our numerical methods, with further details given in the Appendix. After discussing scaled units, we briefly discuss time evolution, before presenting time independent solutions in Sec. 2.2.3.

2.2.1 Harmonic oscillator units (h.o.u.)

For ease of discussion, we will initially consider solution of the NLSE in 1D, where extension to 2D and 3D is conceptually straightforward, as discussed below. Moreover, it is convenient to rewrite the NLSE in terms of dimensionless units. For a trapped gas the most natural scale is the so-called harmonic oscillator length, $\ell = (\hbar/2m\omega_x)^{1/2}$, where ω_x is the trapping frequency introduced in (2.3). Similarly, the units of time and energy can be written in terms of ω_x. This yields harmonic oscillator units (h.o.u.) [56]:

$$x' = x/\ell = \left(\frac{\hbar}{2m\omega_x}\right)^{-1/2} x, \quad (2.16)$$

$$t' = \omega_x t, \tag{2.17}$$

$$E' = \frac{E}{\hbar\omega_x}, \tag{2.18}$$

where x', t', and E' now represent length, time and energy respectively. With the change in length scale, the normalisation of the wavefunction is modified. Thus, requiring that:

$$\int_{-\infty}^{\infty} |\Psi(x,t)|^2 \mathrm{d}x = \int_{-\infty}^{\infty} |\Psi'(x',t')|^2 \mathrm{d}x' = 1, \tag{2.19}$$

implies $\Psi'(x',t') = \ell^{1/2}\Psi(x,t)$.

With these re-scalings, the 1D NLSE becomes:

$$i\frac{\partial}{\partial t'}\Psi'(x',t') = \left(-\frac{\partial^2}{\partial x'^2} + \frac{1}{4}x'^2 + C|\Psi'(x',t')|^2\right)\Psi'(x',t'), \tag{2.20}$$

where we have introduced a nonlinear parameter, $C = 4\pi Na(2\hbar/m\omega_x)^{1/2}$, which will be of prime importance in this thesis. The form of C for higher dimensions is dependent upon the normalisation condition (2.19). In particular, denoting the number of simulation dimensions by γ, C can be shown to be:

$$C = \frac{4\pi\hbar Na}{m\omega_x}\left(\frac{2m\omega_x}{\hbar}\right)^{\gamma/2}. \tag{2.21}$$

Note that for $\gamma < 3$ the definition of N also changes, in order that C remains dimensionless. For 1D, N is defined as the number of condensate atoms per unit area in the $y-z$ plane, while for 2D it is the number per unit length along z. In general, we use lower numbers of dimensions for computational convenience as full 3D simulations can be time consuming. However, 3D will be used to check whether our 2D results are physical and to investigate behaviour not apparent in lower dimensions. An alternative is available when the problem possesses one or more rotational axes of symmetry. In these cases, full 3D simulations (in Cartesian coordinates) can be reduced to quasi-1D (spherical symmetry) or 2D (cylindrical symmetry) problems. We describe procedures for dealing with these situations in the Appendix.

For the remainder of the thesis, we shall drop the primes on the scaled units. Whether scaled or natural units are used shall be obvious from the context, and we will often indicate the conversion factors between the two systems when comparing with experiments.

2.2.2 Time evolution

We may write the scaled NLSE in the following form:

$$i\frac{\partial\Psi}{\partial t} = H_I\Psi, \tag{2.22}$$

in which case the evolution of the wavefunction over a short time Δt can be written in terms of a unitary evolution operator:

$$\Psi(\mathbf{r}, t + \Delta t) = e^{-iH_I(\mathbf{r},t)\Delta t}\Psi(\mathbf{r}, t) + \mathcal{O}(\Delta t^2). \tag{2.23}$$

The error arises due to the time dependence of the Hamiltonian, $H_I(\mathbf{r}, t)$. Numerical methods diverge in the way in which the evolution operator is represented. In the split-step method, the evolution operator is divided into kinetic and potential parts, where the former is dealt with using Fast Fourier Transform (FFT) routines. In Crank-Nicholson, the evolution operator and the kinetic part of the Hamiltonian are represented using finite differences. We discuss these methods in more detail in the Appendix.

2.2.3 Time independent solutions

The numerical methods discussed so far describe the time evolution of the wavefunction. However, it will be useful to be able to obtain time independent solutions by these techniques, in order to investigate the properties of the condensate in equilibrium as well as providing initial states in our simulations. Time independent solutions may be written in the form $\Psi(\mathbf{r}, t) = \Psi(\mathbf{r})e^{-i\mu t}$, so that the 1D time independent NLSE is given by:

$$\mu\Psi(x) = \left(-\frac{\partial^2}{\partial x^2} + \frac{1}{4}x^2 + C|\Psi(x)|^2\right)\Psi(x), \tag{2.24}$$

where μ is the chemical potential. At this juncture we should mention a useful approximation in the large C limit. In this situation the interaction term predominates, and the wavefunction curvature is sufficiently small so that the kinetic term can be neglected. Consequently, the wavefunction takes a parabolic form:

$$|\Psi(x)|^2 = \frac{\mu - x^2/4}{C}. \tag{2.25}$$

This has proved invaluable in analytical studies, and is commonly known as the Thomas-Fermi (TF) approximation [57]. This approximation also furnishes us with an estimate for the chemical potential. Substituting (2.25) into the normalisation condition (2.19) gives:

$$\mu_{\mathrm{TF}}^{\mathrm{1D}} = \left(\frac{3C}{8}\right)^{2/3}. \tag{2.26}$$

In 2D the trap potential can be written as $V_{\mathrm{trap}}(x, y) = \frac{1}{4}(x^2 + \eta y^2)$, where $\eta = \omega_y^2/\omega_x^2$. The chemical potential is thus:

$$\mu_{\mathrm{TF}}^{\mathrm{2D}} = \left(\frac{C\sqrt{\eta}}{2\pi}\right)^{1/2}, \tag{2.27}$$

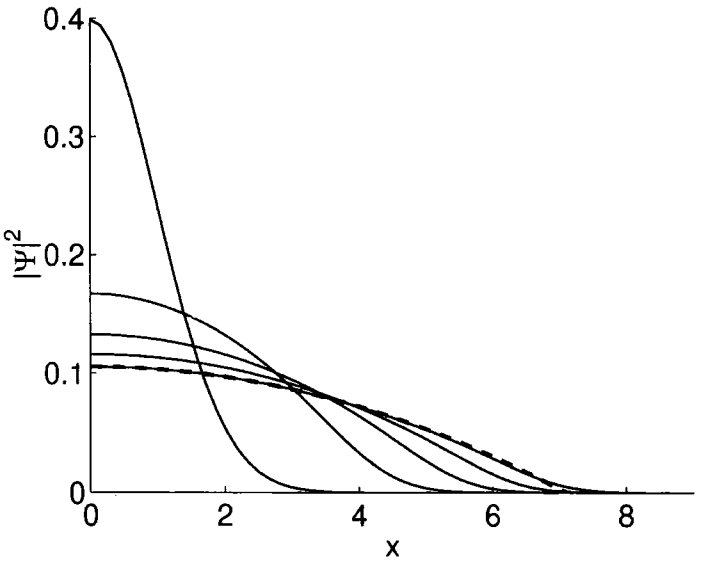

Figure 2.1: Condensate density $\propto |\Psi|^2$, plotted against position (in h.o.u.) for the ground state in 1D, with nonlinear coefficient $C = 0, 30, 60, 90, 120$. As C increases, the edges of the symmetric condensate spread out, until at high C the density tends towards the Thomas-Fermi profile (2.25), plotted as a dashed line for $C = 120$.

while 3D is characterised by a trap potential of $V_{\text{trap}}(x, y, z) = \frac{1}{4}(x^2 + \eta y^2 + \epsilon z^2)$, yielding:

$$\mu_{\text{TF}}^{\text{3D}} = \left(\frac{15C\sqrt{\eta\epsilon}}{64\pi}\right)^{2/5}. \tag{2.28}$$

To numerically obtain time independent solutions of (2.24), one can begin with an analytic ground or excited state solution in the absence of the nonlinear term. For a harmonic trapping potential the n-th order solution is simply written in terms of the Hermite polynomial, $H_n(\xi)$ [58]:

$$\Psi_n(x) = \frac{1}{(2^{2n+1}\pi(n!)^2)^{1/4}} e^{-x^2/4} H_n\left(\frac{x}{\sqrt{2}}\right). \tag{2.29}$$

The solution is then propagated through real time using the Split-Step Fourier method, while at each time-step the value of the nonlinear constant is increased adiabatically ('ramped') until reaching the desired value of C. In practice, this consists of inserting a time dependent pre-factor $P(t) = [1 - \cos(\pi t/\tau_r)]/2$ in front of the nonlinear term [56], where the ramp time $\tau_r \gg 1$.

This method can be used to evaluate ground and excited states for a range of C, yielding the wavefunctions shown in Fig. 2.1, 2.2 and 2.3. We consider here only positive C, corresponding to repulsive interactions. As a result, the wavefunction tends to spread out as C increases, the ground state solution approaching the TF parabolic profile (2.25) at high C (apart from a small region near to the condensate

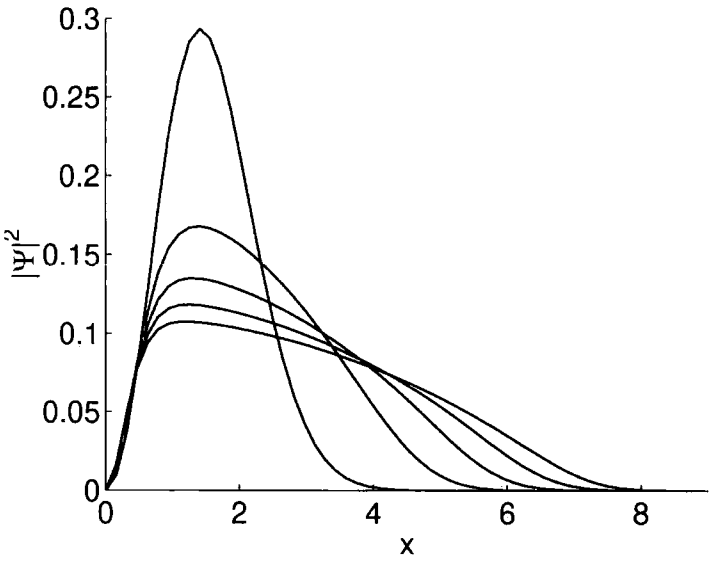

Figure 2.2: Condensate density $\propto |\Psi|^2$ against position (in h.o.u.) for the first excited state of a 1D harmonic trap, with nonlinear coefficient $C = 0, 30, 60, 90, 120$. As repulsive interactions increase the condensate edges spread out; however, the width of the central node remains virtually unchanged.

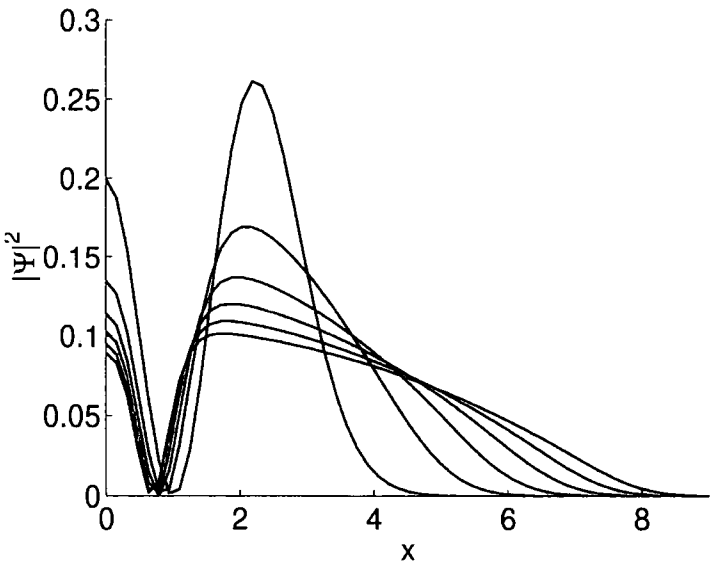

Figure 2.3: Condensate density $\propto |\Psi|^2$ against position for the second excited state for 1D, with nonlinear coefficient $C = 0, 30, 60, 90, 120, 150$. As interactions increase the nodes of the symmetric condensate converge, tending towards a fixed separation at high C.

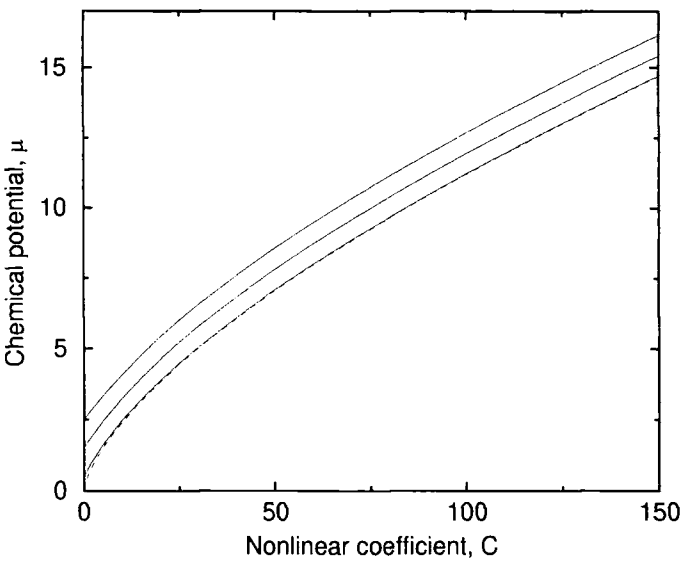

Figure 2.4: Chemical potential, μ (in units of $\hbar\omega_x$) as a function of C for a 1D harmonic trap. The first three energy levels are plotted with solid lines, where the ground state converges to the Thomas-Fermi result (dashed line, 2.26) at high C.

edge). This asymptotic behaviour is also evident in the chemical potential versus C plot of Fig. 2.4; the 1D ground state μ increases from the bare harmonic trap value of $\mu = 1/2$ (in units of $\hbar\omega_x$) to the TF value (2.26) at the high C limit. In addition, the level spacing decreases from $\mu = 1$ at $C = 0$ towards a limiting value of $\Delta\mu \simeq 0.7$ at large C. This is similar to the energy of solitons in 3D condensates [59]: indeed, the first excited state in 1D can be thought of as containing a stationary dark soliton at the trap centre. The behaviour of the excited state energies can be understood in terms of the wavefunctions. As seen in Fig. 2.2 and 2.3, the edges spread out as C increases in a similar fashion to the ground state. However, for the first excited state the width of the central node barely changes as C increases, while in the second excited state the two nodes asymptotically approach a fixed separation, $\Delta x \sim 1$. In Sec. 2.4 we will demonstrate how such modes could be excited by flow of a condensate through a constriction.

The procedure described above is difficult to implement for $C > 150$, requiring long computation times—a problem compounded in 2D and 3D. An alternative scheme for finding ground state solutions is to propagate in imaginary time, $t \to -i\tilde{t}$. In contrast to real time, the resulting time evolution operator is nonunitary, so that the wavefunction must be renormalised after each time-step. Simpson's rule integration was found to be sufficiently accurate for this purpose. The ratio of the

norms then provides a convenient estimate for the chemical potential:

$$\mu = \frac{1}{2\Delta t} \ln \left[\frac{\int |\Psi(\mathbf{r}, t)|^2 \mathrm{d}^3\mathbf{r}}{\int |\Psi(\mathbf{r}, t + \Delta t)|^2 \mathrm{d}^3\mathbf{r}} \right]. \tag{2.30}$$

In imaginary time excitations are exponentially damped, so that the adiabatic ramping required in real time is unnecessary, and both Ψ and μ rapidly converge to a stationary solution (typically in $t < 10$). In general this is the ground state, unless one applies special constraints, as will be discussed for vortex states in Chapter 5. In the case of excited states, sometimes a more convenient technique is to rewrite the time independent GP equation using finite differences, and solve the resulting simultaneous nonlinear equations using an iterative scheme (e.g. Newton's method). In general we shall not use this method in this thesis; however, it has proved useful for studying uniform flow solutions (see [60] for more details). Importantly for our purposes, it also provides a convenient test of the numerics, and we find that the values of μ obtained by this method agrees with the results of imaginary time within a very high precision.

2.3 The output coupler

The last section described how one can obtain stationary solutions of the GP equation, which are useful as initial conditions in simulations. For the remainder of this chapter we will describe two applications. First, we model a MIT experiment demonstrating output coupling of Bose condensed ^{23}Na atoms from a magnetic trap [37], by driving an RF transition to a untrapped state. Previous theoretical studies of RF output coupling have considered 1D motion without gravity [61], or have modelled the process by neglecting kinetic energy [62] or interaction terms [63] in the GP equation. Here we solve coupled GP equations in 2D, with the inclusion of gravity, to model the evolution of both an output pulse and the condensate remaining in the trap.

2.3.1 The coupled Gross-Pitaevskii equations

For ^{23}Na (or ^{87}Rb) condensates, the $F = 1$ ground state is composed of the trapped state $M_F = -1$, the magnetically insensitive level $M_F = 0$, and the anti-trapped state $M_F = 1$. Condensed atoms in each state may be represented by a Bose wavefunction $\Psi_i(\mathbf{r}, t)$, where $i \in \{-1, 0, +1\}$. Given that the magnetic substates are orthogonal, the conservation of probability can be expressed as:

$$\int \mathrm{d}^3\mathbf{r} \sum_i |\Psi_i(\mathbf{r}, t)|^2 = 1 \tag{2.31}$$

The Hamiltonian of the system can now be constructed in a similar manner to (2.8), including gravitational and magnetic trapping potentials, hyperfine interactions, and the RF coupling term $-\boldsymbol{\mu}\cdot\mathbf{B}(\mathbf{r},t)$. Using the Heisenberg equation of motion, or equivalently by applying the variational principle, one can obtain a set of coupled equations describing the dynamics of the parent (Ψ_{-1}) and daughter condensates (Ψ_0, Ψ_1):

$$i\hbar\frac{\partial}{\partial t}\Psi_k(\mathbf{r},t) = \left[-\frac{\hbar^2}{2m}\nabla^2 + V_k(\mathbf{r}) + N\sum_j\langle\Psi_j|\mathcal{U}|\Psi_j\rangle\right]\Psi_k(\mathbf{r},t) + \hbar\sum_{j\neq k}\Omega_{kj}\Psi_j(\mathbf{r},t), \tag{2.32}$$

where $V_k(\mathbf{r})$ represents the sum of the gravitational and trap potentials in the substate k, and Ω_{kj} is the Rabi frequency describing coupling between sublevels, defined by $\hbar\Omega_{kj} = \langle\Psi_k| - \boldsymbol{\mu}\cdot\mathbf{B}|\Psi_j\rangle$. Atom-atom scattering appears as the matrix element $\langle\Psi_j|\mathcal{U}|\Psi_j\rangle$. Assuming that scattering lengths between all atoms are the same, we can replace the interaction with a pseudopotential, as we did for the single-component case.

In the experiment, the RF pulse was of short duration and small area [37], leading to the following simplifications. First, due to the small area ($|\int\Omega_{+1,0}dt| \ll 1$) coupling to the $M_F = +1$ state is small and may be safely ignored, and also back-coupling (i.e. Rabi oscillations) are negligible. An example of strong coupling, where Rabi oscillations are important, has been considered by Ballagh *et al.* [61] in a 1D weightless model. Secondly, the short pulse duration, T, results in broadband excitation, so that we may assume resonant coupling across the trap and neglect the spatial dependence of the coupling term, $\Omega(\mathbf{r},t)$. In addition, we may assume that the parent condensate is 'frozen' during the interaction ($\omega_x T \ll 1$), in which case the daughter condensate is created suddenly as a shadow of the parent, i.e.:

$$|\Psi_0(\mathbf{r},T)|^2 \approx \left|-i\int_0^T dt'\Omega(\mathbf{r},t')\Psi_{-1}(\mathbf{r},t')\right|^2 \approx f|\Psi_{-1}(\mathbf{r},0)|^2, \tag{2.33}$$

and,

$$|\Psi_{-1}(\mathbf{r},T)|^2 \approx (1-f)|\Psi_{-1}(\mathbf{r},0)|^2, \tag{2.34}$$

where f, the fraction of atoms coupled out of the trap, is equal to the square of the pulse area.

Subject to these simplifications, we obtain a pair of coupled time dependent GP equations in 2D:

$$i\partial_t\Psi_{-1} = (-\nabla^2 + \tfrac{1}{4}(x^2+y^2) + C[|\Psi_{-1}|^2 + |\Psi_0|^2])\Psi_{-1}, \tag{2.35}$$

$$i\partial\Psi_0 = (-\nabla^2 + Gy + C[|\Psi_0|^2 + |\Psi_{-1}|^2])\Psi_0, \tag{2.36}$$

where $G = (m/2\hbar\omega_x^3)^{1/2}g$. Note that gravity is absent from Eq. (2.36), as the term simply gives rise to a constant shift in the energy and centre-of-mass of the trapped condensate. With initial conditions given by Eq. (2.33) and (2.34), equations (2.35) and (2.36) are solved to model the dynamical behaviour of the parent and daughter condensates for $t > T$. At each time-step the equations are propagated sequentially, which is accurate so long that Δt is sufficiently small. We now discuss the results of the simulations.

2.3.2 Results

To simulate the MIT experiment we consider the parameters $C = 200$ and $G = 3.0$, corresponding to trap frequencies of $\omega_x = \omega_y \simeq 2\pi \times 200$ Hz and $N \approx 2 \times 10^4$ ^{23}Na atoms per h.o.u. respectively. Density plots of the output pulse (for $f = 0.2$) are presented in Fig. 2.5. After creation, the output pulse is subject to gravity, a repulsive internal force, and a strong repulsion from the residual parent condensate. We see in Fig. 2.5 that even at early times, a combination of these effects dramatically changes the shape of the output. The curvature of the daughter condensate is found to be less pronounced for weaker interaction strengths. At later times the output pulse expands freely, resulting in a 'crescent-shaped' density profile, characteristic of the MIT experiment (see Fig. 2.6) [4, 37]. This suggests that the zero-temperature approximation, inherent in the coupled Gross-Pitaevskii equations, is appropriate for modelling the dynamics of the output. The curvature of the output pulse was not observed in previous theoretical studies [63], due to a different trap geometry and subsequent neglect of the interaction term in the axial direction.

The mutual repulsion between parent and daughter leads to a small recoil of the more massive, trapped condensate. The subsequent motion of the parent can be inferred by studying its centre-of-mass, given by $Y = \int y|\Psi|^2 \mathrm{d}x\mathrm{d}y$. Simulations of a condensate in free-fall show that calculations of the centre-of-mass agree with the classical result, $Y = -Gt^2$, to five significant figures. The centre-of-mass coordinate of the parent condensate along with its acceleration, $\ddot{Y}$, are displayed in Fig. 2.7. The repulsive force from the output pulse reaches a maximum at $t \sim 0.75$. Subsequently, as the coupling term falls to zero due to the decreasing overlap, the parent undergoes harmonic motion at the trap frequency, as expected. Fig. 2.7 also illustrates that the recoil is less for smaller output fractions. Given that the output coupling for small f does not seriously perturb the parent, further coherent pulses may be produced, and one would expect that the recoil on the parent would be negligible for slow, continuous output coupling [38].

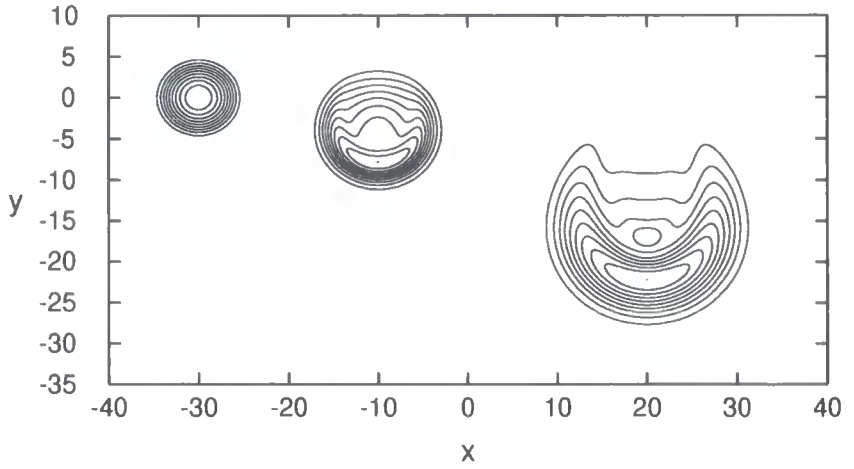

Figure 2.5: Contour plots of $|\Psi(x,y,t)|^2$ for an output coupled Bose condensate falling under gravity, with $C = 200$, $f = 0.2$, and $G = 3.0$, at times $t = 0$ (offset $x \to x-30$), $t = 1.2$ (offset $x \to x-10$) and $t = 2.4$ (offset $x \to x+20$). Nine equally spaced contours are drawn for each time-frame, up to peak densities of $|\Psi(0,0,0)|^2 = 5.67\times10^{-3}$, $|\Psi(0,-7.81,1.2)|^2 = 2.36\times10^{-3}$, and $|\Psi(0,-22.19,2.4)|^2 = 1.25\times10^{-3}$. The repulsive force from the condensate remaining in the trap, combined with free expansion under gravity, creates a characteristic 'crescent shaped' output profile (see Fig. 2.6).

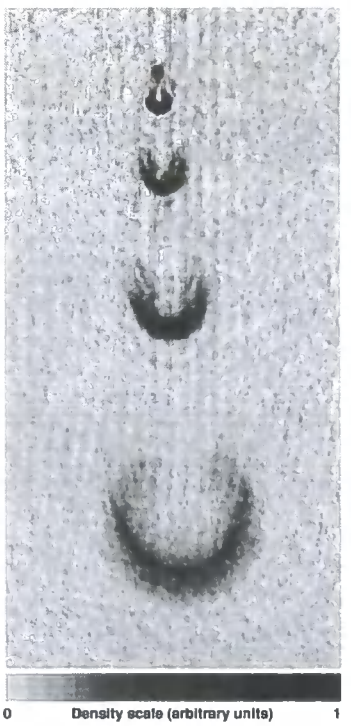

Figure 2.6: Images taken from the output coupling experiment [37], for comparison to results of our simulations (Fig. 2.5). A pulse is created every 5 ms, so that our simulations model behaviour at the beginning of the output process (top of image). Courtesy of the MIT BEC group home page (http://amo.mit.edu/~bec/).

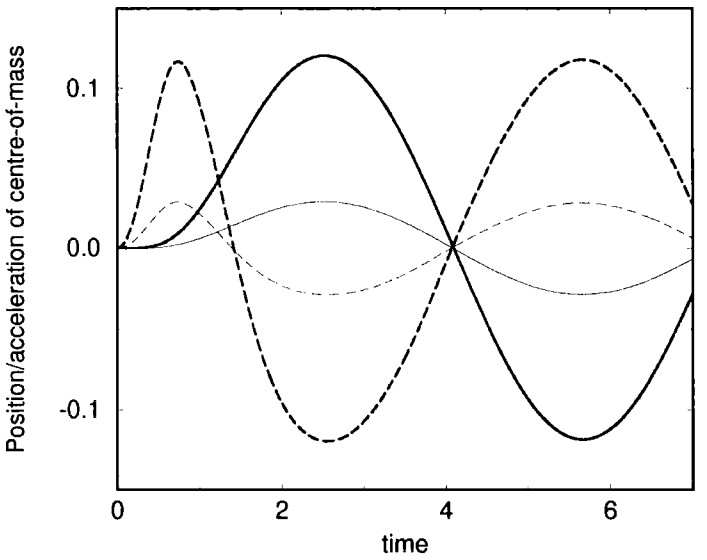

Figure 2.7: Vertical position (Y, full curve) and acceleration ($\ddot{Y}$, broken) of the centre-of-mass of the trapped parent condensate ($C = 200$ and $G = 3.0$) as a function of time. Repulsion from the output pulse induces a recoil, which excites the parent into oscillatory motion (dipole mode). Results are presented for $f = 0.2$ (heavy curves) and $f = 0.05$ (light curves).

Given the agreement between these dynamical simulations and experiment, we surmise that the same numerical methods can be employed to model the dynamics of the condensate in other interesting situations. An example is discussed in the following section, while applications to vortex formation and motion will be the subject of much of this thesis.

2.4 Flow through a constriction

We now consider the flow of a weakly-interacting condensate through a constriction. In the 2D simulations presented here, the condensate is released from an isotropic trap and falls under gravity down a focused, far-off resonance laser beam. The beam is approximated by a harmonic potential in which the spring constant varies with position along y. Any variation in potential along the y-axis (e.g. due to an increase in intensity near to the focus) is neglected. This situation may be realised using a blue detuned doughnut mode laser (see e.g. [8]). The model also assumes that there is no delay between release from the trap and switching on the laser beam. Under this model, for $t > 0$, the evolution of the condensate is given by the equation:

$$i\partial_t \Psi = \left(-\nabla^2 + \frac{1}{4} \left[\frac{1 + (y_m^2/y_0^2)}{1 + (y - y_m)^2/y_0^2} \right]^2 x^2 + Gy + C|\Psi|^2 \right) \Psi, \qquad (2.37)$$

so that the horizontal oscillation frequency, $\omega = (y_0^2+y_m^2)/[y_0^2+(y-y_m)^2]$, is matched to the initial trap frequency at the 'release' position, $y = 0$, and increases by a factor of $[1 + (y_m/y_0)^2]$ at $y = y_m$. The limit $y_0 \to \infty$ corresponds to a collimated laser beam. In this case, the simulations demonstrate that the laser acts as a waveguide for output-coupled condensates.

An interesting situation arises when the laser is tightly-focused. Fig. 2.8 displays results of the simulation for a small nonlinear coefficient ($C = 10$). The density plot at $t = 2.0$ illustrates that three peaks are formed above the constriction. By rescaling, one finds that the peaks approximately match the positions of the maxima in Fig. 2.3, suggesting that the second excited state is populated. The probability that the condensate will be excited from the ground state is related to the rate of change in the Hamiltonian compared to the excitation spectrum [64]. For example, in the adiabatic regime the upper limit to the probability of excitation between eigenstates a and b is given by:

$$P_{ba} \leq \frac{4|\langle\Psi_b|\frac{\partial H}{\partial t}|\Psi_a\rangle|^2}{\hbar^2\omega_{ba}^4}. \tag{2.38}$$

One immediately sees that because $\partial H/\partial t$ is an even function, then the excitations connects only states with the same parity. In addition, mode excitation is more probable for small constrictions and higher C, where a rapid variation in the Hamiltonian is induced. Conversely, for wider constrictions, the Hamiltonian changes slowly and the fluid can adjust adiabatically.

At subsequent times ($t = 2.5$ in Fig. 2.8) the excited 'tail' remains above the constriction, while the 'bulk' of the condensate in the ground state continues to fall. To understand this separation of eigenmodes, consider the simple case of a non-interacting condensate, $C = 0$. As the condensate falls into the constriction, the increase in oscillation frequency, $\delta\omega$, leads to a rise in the chemical potential by $\delta\mu = (n + 1/2)\,\delta\omega$. This increase in energy is offset by a change in the gravitational potential, Gy. Equating the energies gives an expression for the equilibrium position, y_e:

$$y_e = y_m + \frac{\left(n+\frac{1}{2}\right)}{2G} + \sqrt{\frac{\left(n+\frac{1}{2}\right)^2}{4G^2} - \frac{y_m\left(n+\frac{1}{2}\right)}{G} - y_0^2}. \tag{2.39}$$

So, for the n-th mode to be trapped, the following inequality must hold:

$$n \geq 2G\left(y_m + \sqrt{y_m^2 + y_0^2}\right) - \frac{1}{2}. \tag{2.40}$$

In the case of Fig. 2.8, equation (2.39) predicts $y_e \simeq -4.3$ for $n = 2$, just below the actual position as expected, because the small nonlinearity tends to push the

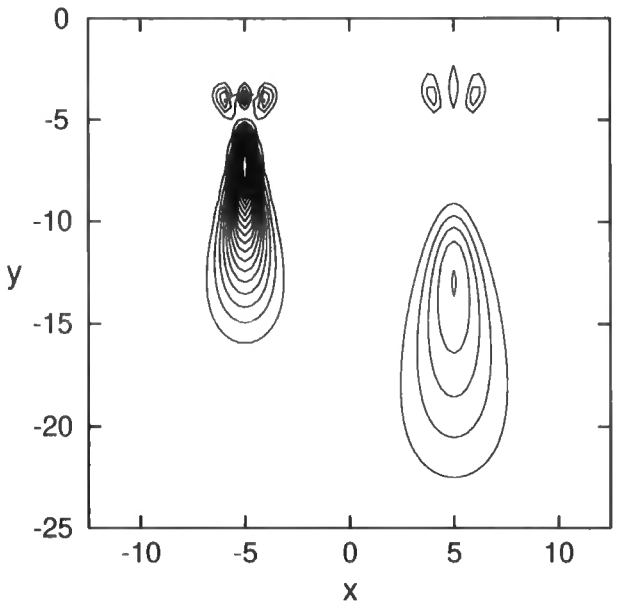

Figure 2.8: Flow of a weakly interacting condensate ($C = 10$, $G = 3.0$) through a constriction, where the horizontal oscillation frequency increases by a factor of 11.5 between $y = 0$ and $y_m = -6$. Density contours are shown at $t = 2.0$ (offset left) and $t = 2.5$ (offset right). The excited 'tail' of the condensate remains above the constriction while the ground state falls under gravity, leading to spatial separation of eigenstates. The contours are drawn with an equal spacing of 7×10^{-3}.

mode upwards. In addition, the inequality (2.40) gives $n > 1.2$, confirming that only excited states are trapped above the constriction. The constriction thus acts as a mode 'filter', and could provide a convenient means to generate and study the decay of excitations. However, for a light-induced potential this would require tight-focusing: typically spot sizes of 1 μm or less.

For large C, the interaction term in the chemical potential dominates. Thus, in addition to the rise in energy due to the changing ω, there is an increase in the density and therefore the interaction energy. As a result, the relative difference between eigenvalues is much lower than for $C = 0$, and mode separation tends not to occur. In Fig. 2.9, one can see that, for $C = 200$, two maxima form above a wide constriction. Parity is still conserved, but the 'tail' in this case consists mainly of a superposition of ground and second excited states. If narrower constrictions are used many modes are excited, and the situation becomes increasingly complex.

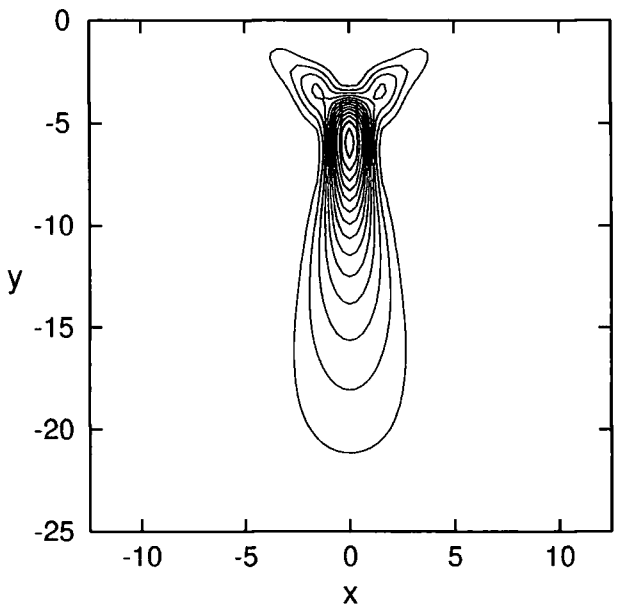

Figure 2.9: Flow of a condensate ($C = 200$, $G = 3.0$) through a constriction at a time $t = 2.0$, where the horizontal trap frequency increases by a factor of 2.5 between $y = 0$ and $y_m = -6$. Similarly to the weakly interacting case, the potential induces excitations in the condensate. Contours are drawn with an equal spacing of 3.03×10^{-3}.

Chapter 3

Superfluidity and vortex formation

In the previous chapter we related how spontaneous symmetry-breaking below the BEC transition leads to phase coherence, and hence to a macroscopic wavefunction which represents the condensate. The properties of the wavefunction can be described in terms of the Gross-Pitaevskii equation, which we solved for ground and excited states. However, the GP equation also admits solutions that are topologically non-trivial, in that they cannot be continuously deformed to the ground state. In these states, the wavefunction phase forms a singularity, corresponding to a defect in the order parameter. Defects can take various forms, ranging from domain walls to monopoles. However, vortices take centre stage in our discussion, where a non-zero fluid circulation is accompanied by a zero in the condensate density. Importantly, the single-valuedness of the wavefunction constrains the circulation to possess multiple values of h/m; in other words, vortices are quantised, a unique feature intrinsic to quantum fluids [22].

This chapter describes a technique for creating vortex-antivortex pairs using a moving object. In some ways the process is analogous to the turbulence that develops in classical fluids when the Reynolds number exceeds some critical value, and indeed vortices are nucleated within the superfluid only above a critical flow velocity. However, the special significance of this process can only be understood by first realising that the condensate is a quantum fluid, which according to Landau [20] can transfer or absorb energy solely in quantised units corresponding to the excitations of the condensate. Hence dissipation, and therefore viscosity or friction, can arise only as a result of the creation of vortices, phonons, or (in HeII) rotons. In the presence of interactions among particles, excitations become energetically favourable above a critical velocity. Thus, superfluidity is a consequence of the quantum nature of the fluid, coupled with the dispersion law of the excitations

(hence an ideal condensate is not superfluid). The important point is that both for superfluid helium and for dilute Bose gases the critical velocity for vortex formation is generally lower than that for phonons or rotons. The creation of vortices is therefore responsible for dissipation and the 'breakdown' of superfluidity in these scenarios.

In trapped Bose gases the 'object' can be created using the repulsive potential arising from a blue detuned far-off resonance laser beam. The beam is focused at the centre of the trap, producing a toroidal condensate. It is then swept out towards the edge at a constant velocity. Here we present 2D and 3D simulations that demonstrate vortex pair formation by the object; first, however, we will briefly review superfluidity and quantised vortices in BEC.

3.1 Superfluidity and quantised vortices

3.1.1 The Bogoliubov spectrum

Much of our present understanding of the relation between BEC and superfluidity is due to the pioneering work of Bogoliubov [65] on the excitation spectrum of dilute Bose condensates. The essential idea is that the Hamiltonian (2.8) can be diagonalised by expressing the field operator $\tilde{\psi}$ as a linear combination of quasiparticle operators α_j and $\alpha_j^\dagger$:

$$\tilde{\psi} = \sum_j [u_j(\mathbf{r})\alpha_j(t) - v_j^*(\mathbf{r})\alpha_j^\dagger(t)]. \tag{3.1}$$

This leads to the Bogoliubov equations:

$$\hbar\omega_j u_j(\mathbf{r}) = [H_0 - \mu + 2Ng|\Psi(\mathbf{r})|^2]u_j(\mathbf{r}) - Ng\{\Psi(\mathbf{r})\}^2 v_j(\mathbf{r}), \tag{3.2}$$

$$-\hbar\omega_j v_j(\mathbf{r}) = [H_0 - \mu + 2Ng|\Psi(\mathbf{r})|^2]v_j(\mathbf{r}) - Ng\{\Psi^*(\mathbf{r})\}^2 u_j(\mathbf{r}), \tag{3.3}$$

where $H_0 = -\hbar^2\nabla^2/2m + V_{\text{ext}}(\mathbf{r})$. Solving the set of coupled equations yields the excitation frequencies ω_j, while the eigenfunctions satisfy the normalisation condition:

$$\int \mathrm{d}\mathbf{r}[u_i^*(\mathbf{r})u_j(\mathbf{r}) - v_i^*(\mathbf{r})v_j(\mathbf{r})] = \delta_{ij}, \tag{3.4}$$

which follows from the constraint that the operators α_j and $\alpha_j^\dagger$ satisfy Bose commutation rules.

In a uniform gas, u and v can be rewritten as plane waves and the Bogoliubov dispersion law follows from (3.2) and (3.3):

$$(\hbar\omega)^2 = \left(\frac{\hbar^2k^2}{2m}\right)\left(\frac{\hbar^2k^2}{2m} + 2gn_c\right), \tag{3.5}$$

where $\mathbf{k}$ is the wave vector of the excitation. For large momenta the spectrum coincides with the free-particle energy $\hbar\omega = \hbar^2 k^2/2m$, while at low momenta the dispersion takes the phonon form $\omega = c_s k$, where:

$$c_s = \sqrt{\frac{gn_c}{m}}, \tag{3.6}$$

is the sound velocity. This simple form for the quasiparticle spectrum in a dilute, homogeneous condensate is modified most notably for liquid ^{4}He and for trapped gases. In the former case the interaction potentials are particularly strong, so that they play an important role when excitations are of a wavelength comparable to the interatomic spacing. As a result the dispersion curve possesses a so-called 'roton minimum' at high frequencies.

In trapped Bose gases the finite size of the condensate discretises the excitation spectrum. This is particularly important when the excitation wavelengths are comparable to the condensate size, so that the lowest energy modes are standing wave phonons dubbed *collective excitations.* The dispersion law for collective excitations was determined analytically in a seminal paper by Stringari [50], and was found to agree very accurately with experimental results at low temperatures [47, 48]. This has been taken to be excellent confirmation of the accuracy of mean-field theory (and by extension, the GP equation) in this regime. The lowest energy collective excitations include the dipole modes (simply rigid-body centre of mass oscillations at the trap frequency), monopole 'breathing modes', and quadrupole oscillations. At higher frequencies phonons propagate through the condensate in a similar manner to sound waves [66, 67], with a velocity equal to the Bogoliubov result (3.6). These modes have been observed experimentally in a quasi-1D geometry [68]. Finally, excitations can take on a single particle character, though the simple energetic dividing line with phonons is more blurred in a trap than in the Bogoliubov spectrum, because low-energy single particle excitations can exist in the low density regions of the cloud [69].

3.1.2 The Landau criterion

The elementary excitations discussed in the previous section take on a particular importance when considering superfluid flow in a channel, or equivalently, around an object. Recall that, according to Landau, dissipation can arise only by creation of elementary excitations with energy ϵ and momentum p. If we consider a frame co-moving with the fluid at a constant velocity v, and perform a Galilean transformation with respect to the laboratory (object) frame, then excitations become

energetically favourable only when $v > \epsilon/p$. This immediately yields the Landau criterion for the critical flow velocity:

$$v_c = \left(\frac{\epsilon}{p}\right)_{\min}. \tag{3.7}$$

For superfluid helium, the critical velocity is determined from the roton minimum, which yields $v_c \simeq 58\text{ms}^{-1}$ [26]. In a dilute Bose condensate, by contrast, the phonon part of the dispersion curve suggests that $v_c = c_s$. We will return to this case later, especially with respect to recent experiments at MIT [45, 70]. However, the important point to note at this stage is that experiments on superfluid He flow though narrow channels yield critical velocities two or more orders of magnitude lower than that expected for rotons. Feynman [23] postulated the existence of another branch of the spectrum, which described the creation of topological rather than elementary excitations. These quantised vortices are the subject of the next subsection.

3.1.3 Quantised vortices

The first step in our discussion of superfluid vortices is to use the Madelung transformation [22] to represent the condensate order parameter in terms of its density $n_c(\mathbf{r}, t)$ and phase $S(\mathbf{r}, t)$, so that:

$$\Psi(\mathbf{r}, t) = \sqrt{\frac{n_c}{N}} e^{iS}. \tag{3.8}$$

The superfluid velocity can then be calculated using the usual quantum mechanical expression:

$$\mathbf{v}_s = \frac{\hbar}{2im|\Psi|^2}(\Psi^*\nabla\Psi - \Psi\nabla\Psi^*), \tag{3.9}$$

which yields the important relation:

$$\mathbf{v}_s = \frac{\hbar}{m}\nabla S. \tag{3.10}$$

Thus there is an explicit link between the superfluid velocity and gradient of the phase. If we consider an arbitrary closed loop in the fluid, then the phase change on traversing the loop is constrained to $2n\pi$, where n is an integer. Hence, the circulation is:

$$\kappa = \oint_C \mathbf{v} \cdot \mathrm{dl} = \frac{nh}{m}. \tag{3.11}$$

This quantisation of circulation is extremely important, as amongst other things it implies that there is an energy barrier between non-vortex and vortex states. The

superfluid therefore prefers to remain irrotational everywhere except at singular points (2D) or lines (3D), so that $|\nabla \times \mathbf{v}_s| = \sum_i 2\pi n_i \delta(\mathbf{r} - \mathbf{r}_{0i})$. These correspond to the centres of point vortices or vortex lines at $\mathbf{r} = \mathbf{r}_{0i}$, and we can define a circulation vector $\boldsymbol{\kappa}$ on the vortex axis, which has magnitude κ and a direction parallel to $\nabla \times \mathbf{v}_s$.

The above constraint on the phase immediately leads to an expression for the tangential velocity:

$$v = \frac{n\hbar}{mr_\perp}, \tag{3.12}$$

where $r_\perp$ is the distance of a point from the vortex centre. The centrifugal forces associated with this circulation field leads to a density zero at the core, which increases to the bulk value over a length-scale of order the healing length [57]:

$$\xi = \frac{1}{(8\pi n_c a)^{1/2}}. \tag{3.13}$$

Thus, a vortex is evident as a density 'hole' within the condensate.

The properties discussed so far are a consequence of the quantised nature of circulation in this system. However, superfluid vortices share many properties with their counterparts in classical hydrodynamics [71]. For example, circulation within any closed fluid loop is conserved, a result known as Kelvin's theorem. In addition, vortices are subject to Helmholtz's theorems. The first states that the vortices cannot terminate in the fluid: they must be closed or terminate on boundaries. The second implies that a vortex moves with the surrounding fluid, although an important exception arises when an external force acts on the fluid. We see in Chapter 5 that the vortex motion can then be described in terms of classical fluid mechanics using a Magnus force argument.

Feynman [23] calculated the minimum superfluid velocity required to create a single vortex ring in a channel of diameter D, which from the Landau criterion (3.7) gives:

$$v_c = \frac{2\hbar}{mD} \ln\left(\frac{4D}{\xi}\right). \tag{3.14}$$

This expression is an improvement on the roton v_c in ^{4}He, as its value lies closer to measurements. It also increases as the channel size decreases, something which is generally observed. However, this simple energetic argument ignores the nucleation mechanism of the vortex, which is of importance in describing the experimental dependence of v_c on temperature and surface roughness [26]. As we shall see later, these arguments are also inadequate for describing analogous effects in trapped condensates. We shall begin to investigate this case in the next section.

3.2 Vortex formation

3.2.1 Background

Experimental progress has recently culminated in the detection of vortices in trapped Bose-condensed gases. The first observation was made at JILA in 1999 [43], where the condensate was excited between two hyperfine states while a laser beam rotating around the periphery of the cloud imparted angular momentum [44]. The final result was a two component condensate, with one component containing a vortex. A subsequent experiment at ENS [72] also used a rotating beam, though here it acted to introduce a trap anisotropy in the radial plane. Above a critical angular velocity this rotation led to a vortex line. Still higher angular velocities resulted in vortex arrays, reminiscent of the rotating bucket experiment of liquid helium [21]. Recent exciting experiments have begun to probe some of the properties of rotating condensates, in particular vortex dynamics and lifetimes [73, 74], and measurements of angular momenta [75].

In addition to this experimental activity, other schemes have been proposed theoretically for creating vortices in trapped BECs. Marzlin and Zhang [76] suggested utilising a configuration of four far-detuned laser beams, where frequency differences result in a rotating light force that transfers angular momentum to the condensate. An alternative approach involves using a Laguerre-Gaussian mode of a laser, where a Raman scheme is employed to avoid spontaneous emission [77, 78]. However, initially resonant Raman pulses may become non-resonant during the interaction owing to nonlinearities within the condensate. Adiabatic tuning of the pulse was proposed in [79] to circumvent this problem. A different route was followed by Dobrek *et al.* [80], where far-off resonance light was passed through an absorption plate in order to 'imprint' the required phase winding onto the condensate. Recently, a similar method was successfully employed experimentally to generate dark solitons [81, 82]. Finally, Caradoc-Davies *et al.* [83] suggested that vortex states could be produced by stirring the condensate with a laser beam.

An alternative scheme proposed here is to focus a blue detuned far-off resonance laser beam within the trapped condensate. The net effect is that of a repulsive conservative potential, so that one can consider the beam to be equivalent to a Gaussian 'object'. Motion of the object can lead to the formation of vortex pairs within the condensate. In this respect, the behaviour is close to that of 2D simulations of homogeneous superfluid flow past cylindrical obstacles [84, 85, 86], where vortex formation was observed above a critical velocity of $v_c \sim 0.4c_s$. In particular, for an impenetrable cylinder with a radius much larger than ξ, a simple argument [84]

leads to $v_c/c_s \simeq \sqrt{2/11}$. However, for the inhomogeneous condensate and penetrable object treated here, the situation is considerably more complex because both the critical velocity and the sound speed are functions of position. Consequently, the conditions for vortex creation depend upon the shape of the condensate and form of the object potential. For example, even for low object speeds, vortices are nucleated towards the edge of the condensate due to the decrease in the speed of sound.

3.2.2 Two dimensional simulations

In general, we solve the usual form of the GP equation in scaled units:

$$i\partial_t\Psi = (-\nabla^2 + V + C|\Psi|^2)\Psi, \tag{3.15}$$

where V represents a time dependent "object" potential superimposed upon a stationary trap: $V = V_{\rm trap} + V_{\rm ob}$. In these 2D simulations we have that:

$$V_{\rm trap} = \frac{1}{4}(x^2 + y^2), \tag{3.16}$$

$$V_{\rm ob} = \alpha \exp\{-\beta[x^2 + (y - vt)^2]\}. \tag{3.17}$$

This potential could correspond experimentally to a quasi-2D configuration where a laser beam propagates along the minor axis of a 'disk'-shaped condensate, though we provide a detailed comparison to realistic situations when discussing our 3D simulations in Sec. 3.4. Here we present results for $C = 500$, $\alpha = 30$ and $\beta = 3$. Most of the calculations were performed using a square box of side 10 divided into a grid of 256×256 points. A larger grid (side 20, 512×512 points) was used to check for edge effects.

We first calculate the wavefunction with a stationary object centred at (0,0) and then begin to propagate the solution at $t = 0$. Instantaneous extinction of the object potential excites sound waves, which propagate with speed $c_s = \sqrt{2C|\Psi|^2}$ (in h.o.u.). For the parameters considered here, $c_s \simeq 4.3$ at the peak density of an unperturbed condensate. Translation of the object displaces the condensate centre of mass, and leads to vortex pair creation as illustrated in Fig. 3.1. At $t = 3$, the object and vortex pair are centred at (0, 6) and ($\pm$2, 3.5) respectively. We observe that the densities at the vortex centres vanish to zero, within a tolerance defined by the grid.

One can gain insight into the process of vortex formation by studying the evolution of the fluid velocity and the phase of the wavefunction. Fig. 3.2 shows a quiver plot of the fluid velocity (3.9) in the vicinity of the object, for the same time

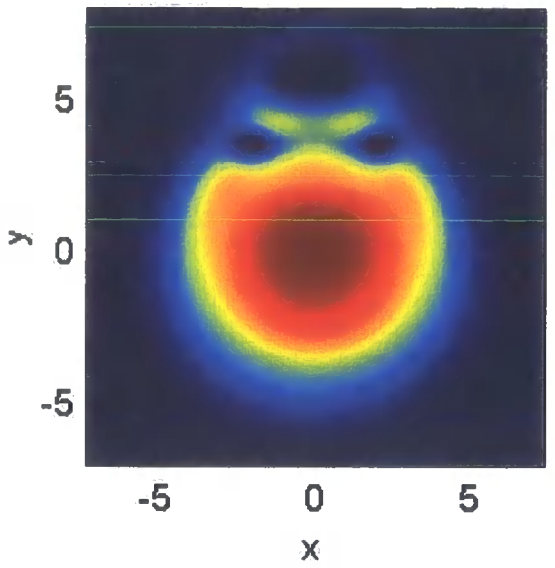

Figure 3.1: Condensate density $|\Psi(x,y)|^2$ for $v = 2.0$ at time $t = 3.0$. The object and vortex pair are centred at (0.0, 6.0) and (±2.0, 3.5) respectively.

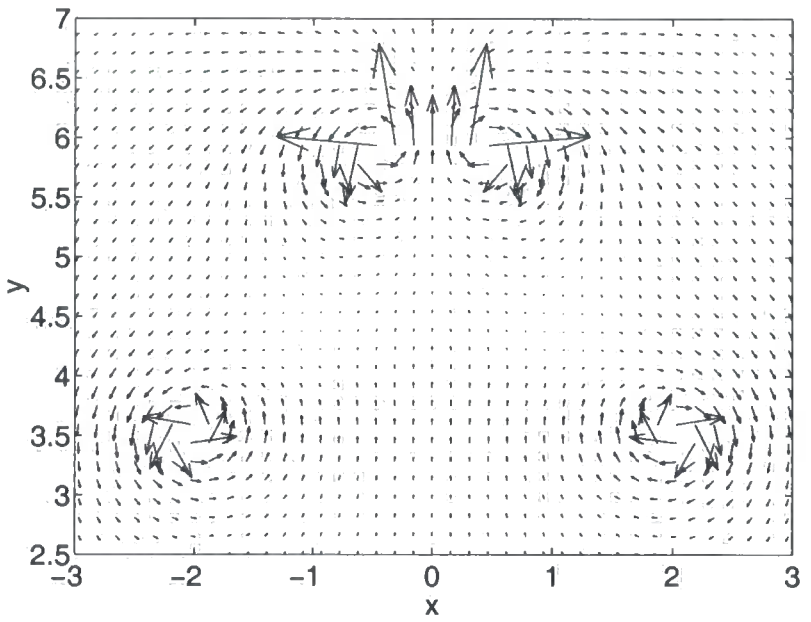

Figure 3.2: Plot showing the fluid velocity field, v_s, in the vicinity of the object, for the same parameters as Fig. 3.1. The characteristic circulation patterns of vortices are clearly evident.

as plotted in Fig. 3.1. One sees that vortices are formed in pairs with opposing vorticity, and that the circulation velocity is inversely proportional to the distance from the vortex core, as expected from (3.12). Two pairs are discernible in Fig. 3.2: one at $y = 3.5$, which corresponds to the density zeros in Fig. 3.1, and a second at $y = 5.9$ (not visible in Fig. 3.1 because the vortices are yet to separate from the object). The second pair appears due to the rapid accumulation of phase slip at the edge of the condensate, as discussed below.

By calculating the wavefunction phase, $S(x, y, t)$, one can verify that the phase changes by 2π on circulation of the vortex, confirming that they are singly quantised. Moreover, the evolution of the phase illustrates the time scale for vortex formation. At $t = 0$ the phase is uniform. Subsequently, the motion induces a dephasing or 'phase slip' centred on the object. The phase slip between two neighbouring points along the y-axis is defined as:

$$\Delta S(y, t) = \arg\{\Psi(0, y + \Delta y, t)\} - \arg\{\Psi(0, y, t)\}, \tag{3.18}$$

with $-\pi < \arg\{z\} \leq \pi$. The maximum phase slip, $\Delta S_{\max}$, occurs at a y-coordinate directly behind the centre of the object. Fig. 3.3 plots the time dependence of $\Delta S_{\max}$ for various object speeds. For $v = 2$ and $v = 3$, the phase slip accumulates gradually, reaching a value of π before changing sign. The sign change coincides with a reversal of the flow, and may be taken to define the moment of vortex creation. The rate of change of the phase slip is related to the speed of sound, which determines the time scale over which the condensate can respond to an external perturbation. For a smaller C, i.e. lower sound velocity, the phase slip accumulates more rapidly and the vortex pair is created earlier (compare curves for $C = 200$ and $C = 500$ in Fig. 3.3). After the vortices are created, the phase slip builds again until a second pair forms, and so on. For low object speed (e.g. $v = 1.3$, upper plot in Fig. 3.3) the phase slip initially saturates before increasing as the object approaches the edge of the condensate, where the density and therefore the local speed of sound are lower. This explains the sudden formation of a vortex pair as the object leaves the condensate (e.g. the second pair for $v = 2$ which appears in Fig. 3.2 and 3.3).

The evolution of the velocity field during vortex formation is illustrated in Fig. 3.4. Before formation (top) the on-axis flow is in a direction opposing the object motion, as the fluid tries to fill the void left by the departing object. However, the fluid velocity is limited by the local speed of sound, and the resulting chemical potential imbalance leads to a phase slip along the y-axis, as shown in Fig. 3.3. When the phase slip reaches π, the on-axis flow reverts to a forward direction, creating the dipolar pattern illustrated in Fig. 3.4 (centre). The wavefunction nodes

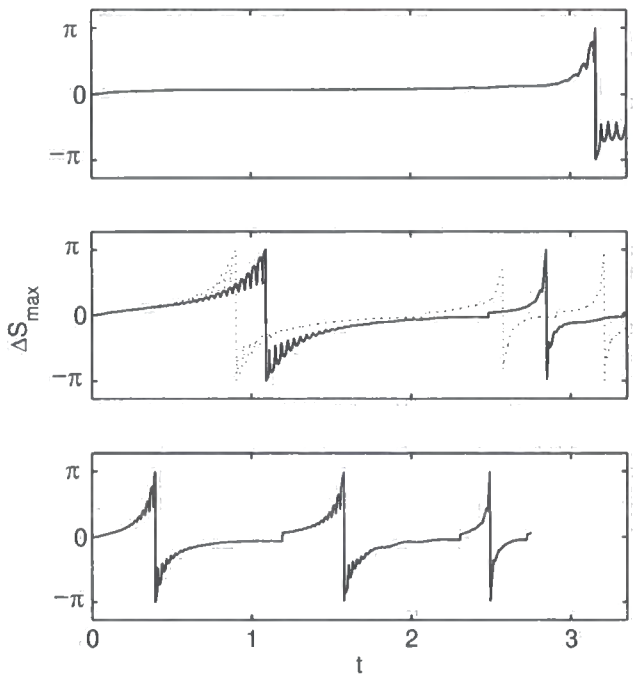

Figure 3.3: Time evolution of the maximum phase-slip, $\Delta S_{\max}$, for $v = 1.3$ (top), $v = 2.0$ (middle), and $v = 3.0$ (bottom). Simulations are performed at $C = 500$; however, for $v = 2.0$ we display an additional curve for $C = 200$ (dotted) which illustrates that the vortex shedding frequency increases as the speed of sound decreases. Note that the 'fringes' evident on some of the curves are artifacts of the finite grid size.

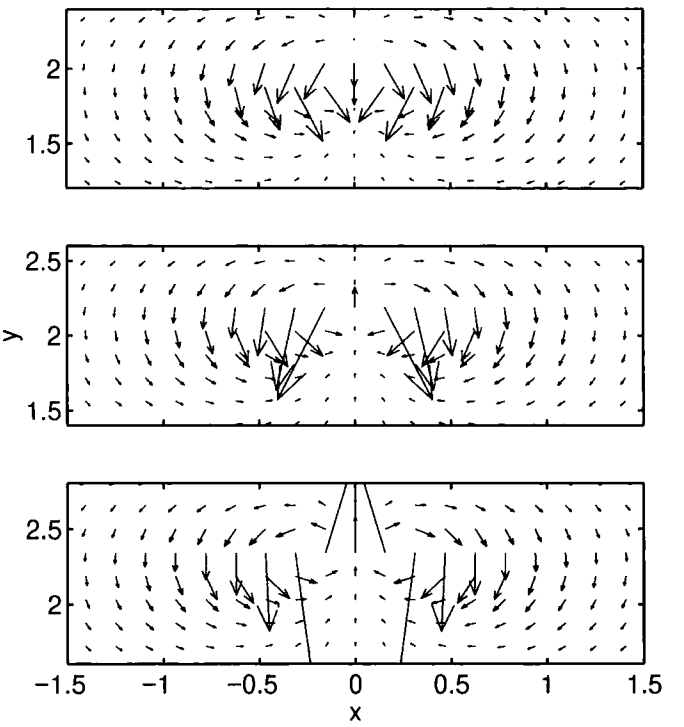

Figure 3.4: Plot showing the velocity field in the vicinity of the object for $v = 2.0$, at times spanning the instant of vortex formation: $t = 1.0$ (top), $t = 1.1$ (middle) and $t = 1.2$ (bottom).

(separated by less than a grid point at this stage) are pulled apart due to the gradient in the object potential. In the bottom plot, their separation is comparable to the healing length, and the pattern of vortex flow is beginning to emerge.

The time evolution of the density is plotted as cross-sections in Fig. 3.5. The repulsive beam initially creates a density minimum at the condensate centre. On translation of the object, a transient sound wave is produced, which is evident as a density dip behind the beam and a peak in front. This simply arises due to the finite compressibility of the condensate. Importantly, the condensate density at the object then rapidly evolves to zero. Vortex pairs are nucleated from this point of zero density. In fact, this is a general requirement following from Kelvin's theorem, in order to conserve vorticity within an arbitary closed loop. For infinitely high potentials [84, 86] vortex pairs are nucleated at the surface on opposite sides of the obstacle, so that naively one could say that the vorticity within a loop intersecting the surface is not conserved. However, this loop is not closed, as fluid particles cannot enter into the object. Hence, Kelvin's theorem is not violated in this case.

As a matter of interest, we also note that vortex formation also occurs in simulations of a red detuned laser, as illustrated in Fig. 3.5 (bottom). In this case

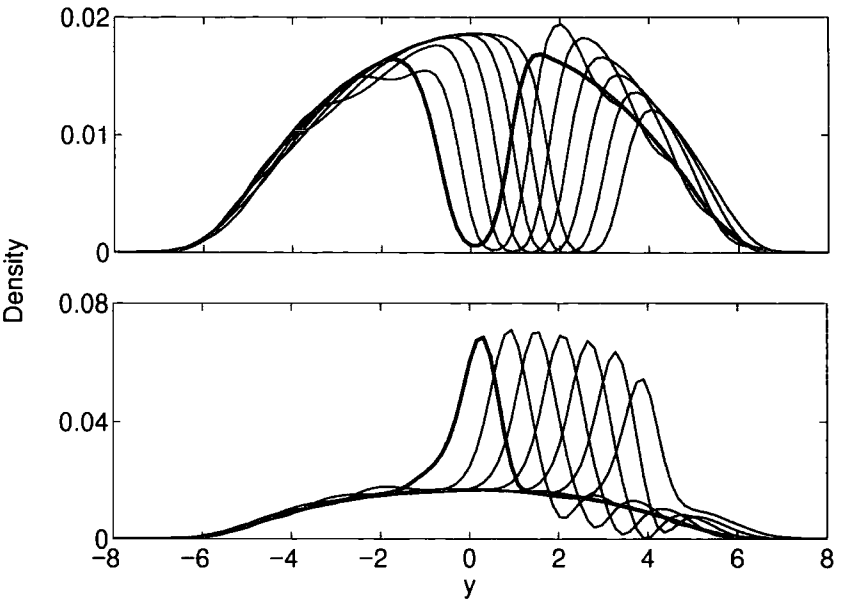

Figure 3.5: Time evolution of the density in 2D simulations, illustrated by $x = 0$ cross-sections for $\alpha = 30.0$, $v = 2.0$ (top) and $\alpha = -30.0$, $v = 3.0$ (bottom). The bold curves plot the density at $t = 0.1$, while subsequent curves are plotted in steps of 0.2 up to $t = 1.3$.

the attractive potential creates an enhanced peak in the condensate. However, on translation a trough is created immediately in front of the beam. The amplitude of the trough increases with time, and a vortex pair is created when its density reaches zero. In this respect the behaviour is similar to that of a repulsive object, and strongly suggests that vortex formation is a general consequence of some kind of 'wavefunction instability' within the GP equation. We shall return to this point in Chapter 6.

3.2.3 Three dimensional simulations

In the previous section we studied vortex formation using 2D simulations of a moving laser beam. In this section, we present 3D results which more accurately reflect experimental situations. We find that vortex pairs are still produced, which can be imaged using standard experimental techniques. We also investigate the dynamics of vortex formation in 3D trap geometries.

Our simulations employ a full 3D cartesian grid (typically with $128 \times 128 \times 32$ points) to solve (3.15) with the generalised potentials:

$$V_{\text{trap}} = \frac{1}{4}(x^2 + \eta y^2 + \epsilon z^2), \tag{3.19}$$

$$V_{\rm ob} = \frac{U_{\rm ob}}{\sigma} \exp\left\{\frac{-2[x^2 + (y - vt)^2]}{\sigma \tilde{w}_0^2}\right\}. \tag{3.20}$$

where $\tilde{w}_0 = w_0(2m\omega_x/\hbar)^{1/2}$ is the beam waist at $z = 0$ while $\sigma = 1 + (z/z_0)^2$ [87]. The Rayleigh range is $z_0 = \pi\tilde{w}_0^2/\lambda$, where λ is the laser wavelength. The potential at the centre of the focus (0,vt,0) is given in h.o.u. by:

$$U_{\rm ob} = -\frac{P}{4\pi w_0^2 \Delta\tau^2 I_{\rm sat}\omega_x}, \tag{3.21}$$

where τ and $I_{\rm sat}$ are the atomic lifetime and saturation intensity respectively, while P and Δ are the laser power and detuning [8]. Typical parameters for our simulations are $C = 500$, $U_{\rm ob} = 50$ and $\tilde{w}_0 \simeq 1.22$, which correspond to $N = 5 \times 10^4$ ^{23}Na atoms with $P \simeq 12.0\mu$W and and a beam waist of 8.43μm for $\omega_x = 2\pi \times 4.6$Hz. Note that experimentally this represents a rather 'loose' trap; however this has the advantage of expanding the length scale, so that a less tightly focused laser beam can be used. Additionally, we use a laser wavelength of $\lambda = 500\,\text{nm} \simeq 7.23 \times 10^{-2}$ h.o.u. and $\eta = 1$, corresponding to an isotropic trap in x-y plane, a general feature of existing experiments.

First, we perform simulations for $\epsilon = 9$, corresponding to a 'disk'-shaped condensate. Fig. 3.6 shows results for six different time-frames up to $t = 3.0$. The column density is plotted, which is defined by:

$$n_{\rm col}(x, y, t) = \int_{-\infty}^{\infty} {\rm d}z |\Psi(x, y, z, t)|^2. \tag{3.22}$$

This is intended to model experimental observations, where imaging techniques probe the density along a line-of-sight. We see that at later times vortices are clearly discernible as dark regions, representing density minima within the condensate. Strictly speaking, the plots in Fig. 3.6 would correspond to phase-contrast images [88], where the condensate is probed *in situ*. The healing length in this simulation is equivalent to $\xi \sim 2.7\,\mu$m, so direct imaging of the cores may be possible. Alternatively, vortices can also be imaged after a period of ballistic expansion, where the vortex cores expand at approximately the same rate as the condensate [89, 90]

The dynamics of vortex formation in the 3D configuration is also of interest. We can study the line motion in our simulations by detecting the minima of the wavefunction, and recording their position (x, y) as a function of z and t. Quadratic interpolation between grid-points is used to estimate the positions more accurately. We find that the inhomogeneity of the light intensity and the condensate density along the axis of the beam results in emergence of the vortex pair at different times

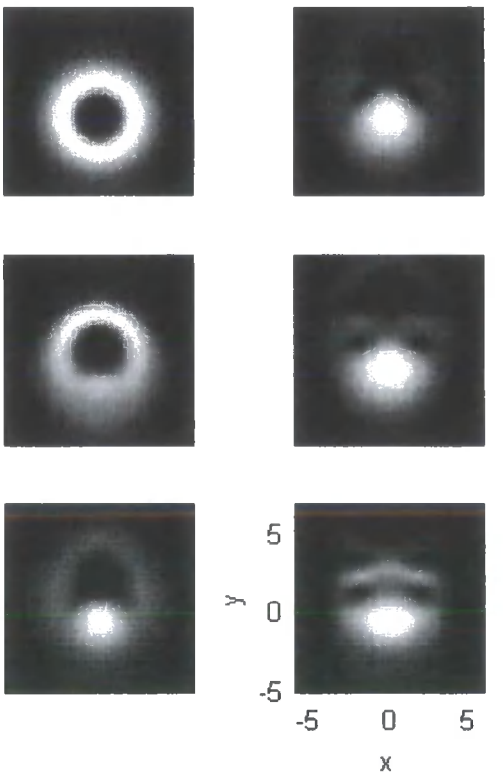

Figure 3.6: Results of 3D simulations of a moving laser beam with $\epsilon = 9.0$ and $v = 2.0$, plotted as column densities integrated along the z-direction. The plot on the top left shows the density at $t = 0$, while subsequent frames are plotted in steps of $t = 0.6$. Vortices are clearly evident at later times (right).

along z. In this case, the lines separate first near to $z = 0$ at $t \simeq 0.46$, before the formation extends out to the edge. However, as we shall discuss below, the form of this process is heavily dependent on the details of the beam focusing and trap geometry. The result is the formation of curved vortex lines, which subsequently separate in the x-direction. Inhomogeneities in the condensate lead to the curvature becoming more pronounced, so that a velocity is induced at each point by the remainder of the line. This results in propagation of helical Kelvin waves along the vortices [22].

The fundamental Kelvin mode can be studied by comparison of the x, y coordinates of the vortex minima at $z = 0$ and near to the edge, and is plotted in Fig. 3.7. This shows an elliptical motion of the line. The sense of the rotation can be understood by arguments based upon the Magnus effect, as we shall see in Chapter 5. Despite the importance of Kelvin waves, it is likely that their experimental detection will be very difficult. This can be discerned from Fig. 3.6, where one might expect to observe a modulation in the density in the region of an oscillating vortex. However, because the vortex curvature is slight and is most pronounced in low-density parts of the cloud, then any variation is difficult to detect. Ballistic expansion would make detection even more troublesome, with a tendency to stretch the line. One solution to this problem is to create more highly curved lines. With this aim in mind we repeated our calculations with the parameters $U_0(0)/\hbar\omega = 200$, $\epsilon = \eta = 1$ and $\tilde{w}_0 \simeq 0.217$, corresponding to a spherical condensate pierced by a tightly-focused laser beam. Plots of the line minima are displayed in Fig. 3.8, showing that highly curved lines are created. Note that in this case the lines initially separate near to the condensate edge. The vortices then undergo wave motion in a similar manner as previously.

We find that the subsequent vortex motion is very complicated—not only does the condensate inhomogeneity and line curvature contribute to the dynamics, but there is induction from the anti-vortex, as well as any other pairs that are created further along the path of the beam. It is therefore simpler, as well as more instructive, to study a case with intrinsic cylindrical symmetry, effectively reducing the problem to 2D. Such a system will be considered in Chapter 5.

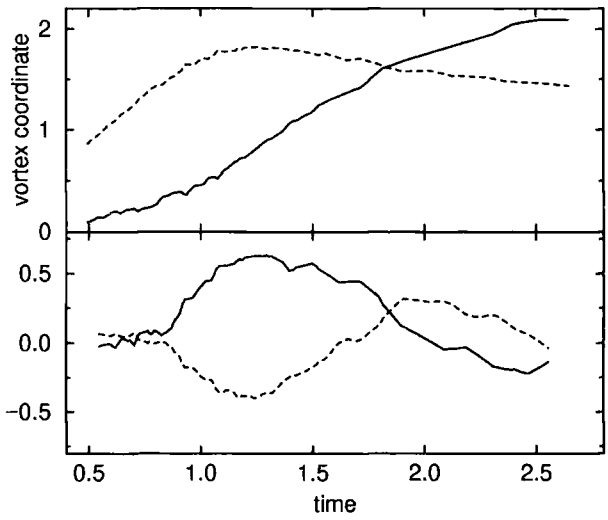

Figure 3.7: Vortex position as a function of time after creation, where $\epsilon = 9.0$ and $v = 2.0$. The upper plot shows x- (solid) and y- (dashed) positions at $z = 0$, while the lower plot displays the x- and y- positions at $z = 1.75$ minus those at $z = 0$.

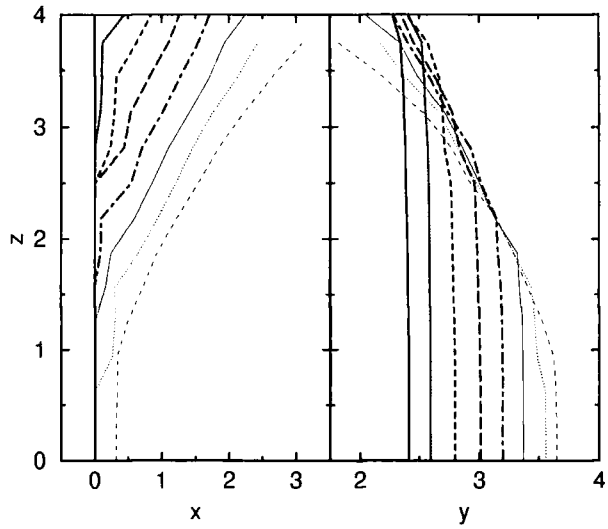

Figure 3.8: Evolution of a vortex line after creation by a moving beam, where the position of the density minimum at z is plotted as as a function of x (left) and y (right). Parameters are given in the text, with $U_0(0)/\hbar\omega_x = 200$, $\epsilon = 1.0$, and $v = 2.0$. Each line represents the following times: $t = 1.2$ (solid), 1.3 (dotted), 1.4 (dashed), 1.5 (long dashed), 1.6 (dot-dashed), 1.7 (faint, solid), 1.8 (faint, dotted), and 1.9 (faint, dashed). Note that only a single vortex is plotted above $z = 0$, as the system is invariant under reflections in the x- and z- axes.

Chapter 4

Two-component condensates, mutual drag, and vortex rings

In the previous chapter we discussed vortex pair formation by a localised object moving within a trapped Bose-Einstein condensate. We proposed that such an object could be formed using a focused far-detuned laser beam. In general, the laser Rayleigh length is much larger than the cloud radius, so that the object is approximately cylindrical. This symmetry is responsible for the creation of vortex pairs rather than, for example, vortex rings, where the ends of the line join together to form a closed loop. To nucleate rings, a object of roughly spherical symmetry should be used. In this chapter, we describe how such structures could be produced by manipulating a two-component condensate, where a small 'object' condensate is dragged through a larger, more loosely confined condensate, the 'fluid.' The process is analogous to ring nucleation by moving ions in superfluid ^{4}He [91], albeit on a much larger scale. Moreover, we find that this realises an attractive system for studying drag and its relation to vortex formation. As we shall show, the drag is related to the centre-of-mass motion of the condensate, which could be measurable in current experiments.

However, we shall begin by discussing the general properties of multi-component condensates. We then show that we can accurately model these systems by simulating an experiment at JILA [42], which studied the dynamics of component separation after creation by a two-photon transition. In some ways this is similar to the simulations of output coupling discussed in Chapter 2 in that we utilise coupled GP equations to describe each component. However, the results differ markedly because both condensates remain in the trap. The component separation in this case arises from inter-condensate repulsion and an offset in the equilibrium positions of the condensates within the magnetic field. We observe the formation of structures, in good agreement with the experiment. We also attempt to explain the observed

experimental damping in terms of mode mixing and finite temperature effects.

4.1 Multi-component condensates

Production of multi-component mixtures of Bose-Einstein condensates involves simultaneously trapping atoms in more than one spin state. This is possible, for example, in optical dipole traps [35] which can confine atoms in any spin state, allowing study of so-called spinor condensates [92, 93]. Spin therefore comprises an additional degree of freedom, and the order parameter is a vector rather than a scalar quantity. A two-component system was first realised at JILA [40], where a magnetic trap confined the $|F = 2, M_F = 2\rangle$ and $|F = 1, M_F = -1\rangle$ hyperfine states of ^{87}Rb. In the small-field limit, the magnetic energy of a state characterised by a magnetic moment $\boldsymbol{\mu}$, in a field $\mathbf{B}$, is:

$$U = -\boldsymbol{\mu} \cdot \mathbf{B} = g_F M_F \mu_B B. \tag{4.1}$$

States for which the product $g_F M_F$ is positive minimise their energy in low fields, and may be trapped in the minimum of a magnetic field. For ^{87}Rb, this leads to three trappable states: the $|2, 2\rangle$ and $|2, 1\rangle$ states in the $F = 2$ hyperfine manifold (where $g_F = +1/2$) and the $|1, -1\rangle$ state in the $F = 1$ manifold (where $g_F = -1/2$). The positions of the condensates are dependent on gravity and their respective magnetic moments, which determines how tightly confined they are. This means that the $|2, 2\rangle$ and $|1, -1\rangle$ clouds 'sag' under gravity by different amounts, so to enhance the spatial overlap of the components the $|2, 1\rangle$ and $|1, -1\rangle$ states were used in later JILA experiments. The transition between the two states was driven with a two-photon RF/microwave pulse. This facilitated interesting studies of, for instance, relative condensate phases [94] and vortex states [43]. Subtle behaviour arising from the rotating magnetic field of the TOP trap [95] allowed experimenters to vary the relative positions of the condensates. For example, the centres of the two components could be aligned to obtain the maximum spatial overlap.

Many properties of the system can be understood in terms of identical and distinguishable particle collisions. If we denote the states by $|1\rangle$ and $|2\rangle$, then scattering lengths between atoms in the same hyperfine level can be signified by a_1 and a_2, while a_{12} represents scattering between hyperfine states. The configuration of the system is then determined by the relative strengths of the interactions. As an example, consider the case where the condensate centres coincide, and $a_{12} > 0$ (i.e. repulsive interactions). For small a_{12}, the condensates intermingle, while for larger a_{12} phase separation occurs, where the two components occupy different regions

of space. To minimise the energy of the configuration, the state with the larger scattering length tends to form a low density shell around the other species [96, 97]. This behaviour is related to the critical value for instabilities (negative eigenvalues) in the excitation spectrum, a_{12}^c, which can be estimated within the Thomas-Fermi approximation [98]:

$$|a_{12}^c| \simeq \sqrt{a_1 a_2}. \tag{4.2}$$

Numerical studies [99] confirm this result. For an attractive inter-species potential $a_{12} < 0$, such that $|a_{12}| > |a_{12}^c|$, the instabilities are associated with collapse of the system, analogous to a single condensate with attractive interactions [3]. For repulsive interactions, the condition $a_{12} > |a_{12}^c|$ corresponds to the phase separation process described above. More generally, the repulsion results in breaking of the spatial symmetry of the system, either spontaneously [100] or by the trapping fields. In the case of the experiment described in [42] the equilibrium position of the two condensates differed slightly, breaking symmetry along the direction of gravity. The inter-component repulsion thus excited oscillatory motion of the centre-of-masses, in addition to structures within the condensates. We will simulate this scenario in the following section.

4.2 Dynamics of component separation

As in Section 2.3 we employ the 2D coupled dimensionless GP equations:

$$i\partial_t \Psi_i = \left[-\nabla^2 + V_i + C\left(\alpha_i|\Psi_i|^2 + |\Psi_j|^2\right)\right]\Psi_i, \tag{4.3}$$

where $i, j = 1, 2$ $(i \neq j)$. We define the ratios between the scattering lengths as $\alpha_1 = a_1/a_{12}$ and $\alpha_2 = a_2/a_{12}$. We assume that a condensate initially in a state $|1\rangle$, with trapping potential $V_1 = (x^2+\epsilon y^2)/4$, is subject to an interaction which transfers 50% of the population into state $|2\rangle$. The latter experiences a displaced potential $V_2 = [x^2 + \epsilon(y - y_0)^2]/4$, where y_0 is the offset. Parameters in our simulations are chosen to reflect closely those in the experiment [42]. In particular, $\epsilon = 8$, $\omega_x = 2\pi \times 59/\sqrt{8}$, $C = 3160$ and $y_0 = 0.24 \simeq 0.4\,\mu$m. Ratios of the scattering lengths are taken to be $\alpha_1 = 1.03$ and $\alpha_2 = 0.97$, where $a_{12} = 5.5$ nm for ^{87}Rb.

The displaced potential causes the two components to separate and subsequently oscillate at large amplitudes. Nonlinear mixing [56, 101, 102, 103] leads to excitation of higher order modes, that appear as structures in the density profiles (Fig. 4.1). Comparison with the experimental images reveals remarkable agreement for early times. At later times higher order structures start to appear in our simulations, which are also shown in a density cross-section at $t = 8.52$ (corresponding to 65 ms)

in Fig. 4.2(a). However, in the experiment most of the structure had disappeared by this time. This disparity may be due to Landau damping at finite temperatures, where condensate excitations are absorbed by the thermal cloud. More explicitly, the damping mechanism involves processes in which an excitation (ν) of low energy ($E_\nu \ll \mu, T$) and a high energy thermal excitation (γ) are annihilated, to create another thermal excitation (γ'):

$$\nu + \gamma \leftrightarrow \gamma'. \tag{4.4}$$

As indicated, the inverse process is also possible. To simulate this effect phenomenologically, we propagate the GP equations (4.3) in complex time $t \rightarrow (1 + i\Lambda)\tilde{t}$ [104]. The GP equations then become:

$$i\partial_t \Psi_i = (1 + i\Lambda)[-\nabla^2 + V_i + C(\alpha_i|\Psi_i|^2 + |\Psi_j|^2) - \mu_i]\Psi_i, \tag{4.5}$$

where the imaginary part represents dissipation in the system. Thus, components with an energy E decay exponentially at a rate proportional to the damping constant, $\Lambda < 0$, and to $E - \mu_i$, in agreement with theory for the collisionless low-energy regime [105, 106, 107, 108]. Higher frequency excitations are preferentially damped, reducing the density variations within the condensate [Fig. 4.2(b)]. Note that to compare simulated lifetimes to physical results, we excited quadrupolar modes in a single condensate and propagated in complex time. Using this procedure, we estimate that a damping rate of $\Lambda = -0.01$ corresponds to typical experimental values [47, 109]. However, we present results for $\Lambda = -0.025$, to clearly illustrate the physical effects of Landau damping.

Fig. 4.3 shows the centre-of-mass position, $Y_i(t)$ of the two condensates as a function of time. Population of the high-energy excitations results in damping of the dipole mode, in agreement with previous work [110]. However, this mechanism alone is insufficient to explain the observed experimental damping. Propagation in complex time results in further damping, but at a relatively slow rate. We also investigate the effect of an offset in the x direction, which may arise as a consequence of the experimental geometry [111]. Due to the anisotropy of the trap, the dipole mode corresponding to oscillations along the 'slow' x-axis possesses a lower energy than along y. Displacement of the trap initially leads to oscillations along the 'fast' axis as above; however, the broken symmetry now results in transitions that gradually populate the lower level. This 'mode-mixing' effect may be more significant than finite-temperature effects in explaining the observed damping (see Fig. 4.3), although it is likely that a combination of these mechanisms is responsible.

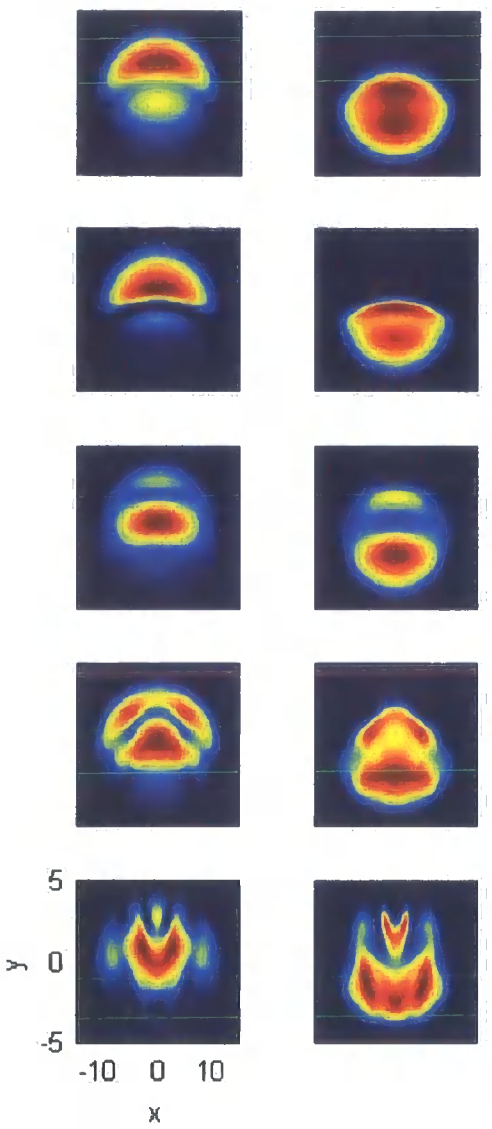

Figure 4.1: Density profiles for components $|1\rangle$ (left) and $|2\rangle$ (right). Time-frames are shown for (top to bottom) $t = 1.5$ h.o.u., $t = 2.0$, $t = 3.3$, $t = 5.2$, and $t = 8.52$. For the experimental trap frequency, $w_x \simeq 131\text{s}^{-1}$, these times would correspond to $t \simeq 11$, 15, 25, 40, and 65 ms respectively.

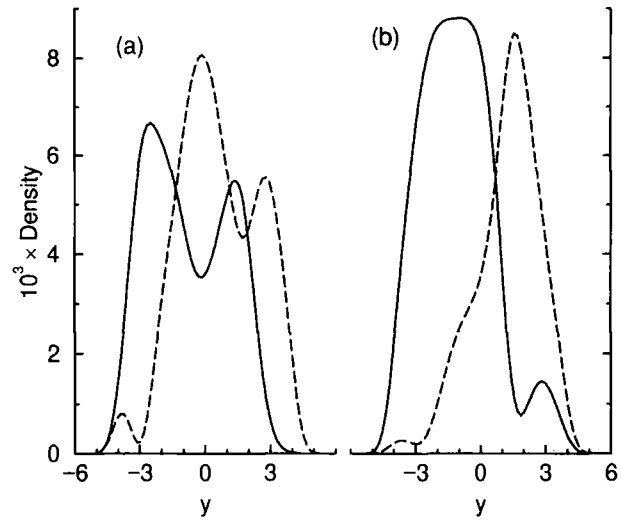

Figure 4.2: Cross-sections through 2D density profiles, $|\Psi_1|^2$ (dashed) and $|\Psi_2|^2$ (solid), at $x = 0$ and $t = 8.52$, showing results of (a) undamped, and (b) damped ($\Lambda = -0.025$) propagation.

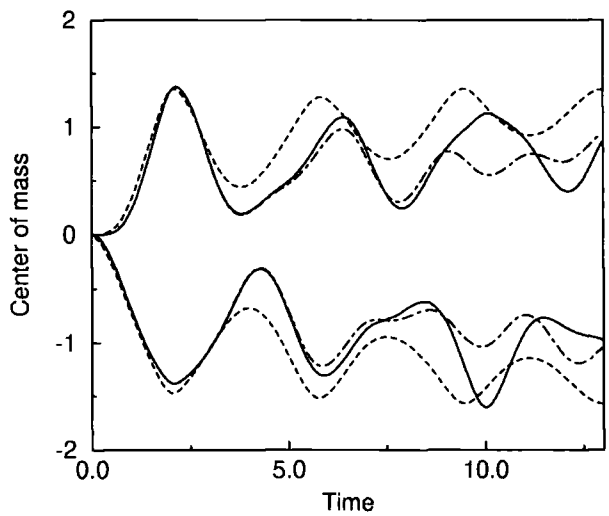

Figure 4.3: Centre-of-mass oscillations, $Y_i(t)$, in $|1\rangle$ (top) and $|2\rangle$, for undamped (solid) and damped $\Lambda = -0.025$ (dashed) propagation. The dot-dashed lines show the effect on undamped propagation of an additional offset, $x_0 = 0.240$, where decay of the oscillations are more marked than even a large Landau damping.

4.3 Vortex ring formation and mutual drag

As is apparent in Fig. 4.3, over short timescales ($t < 2$) thermal damping is negligible and the undamped GP equations provide a reliable model of two-component dynamics. We now turn to the situation where one condensate flows through the other, in direct analogy with an object moving through a fluid. This may be realised experimentally by using a magnetic trap to confine atoms in state $|2\rangle$, whilst an optical dipole trap, moving with relative velocity $-v$, loosely confines atoms in a magnetically insensitive level $|1\rangle$. We employ the coupled equations (4.3), with $V_1 = (x^2 + y^2)/4$ and $V_2 = V_1 + (x^2 + (y - vt)^2)$. As our conclusions are unaffected by the relative values of the scattering length, we set $\alpha_1 = \alpha_2 = 1$. The repulsive mean field arising from the 'object' ($|2\rangle$) creates a local minimum in the centre of the density profile of the 'fluid' ($|1\rangle$) [96]. The depth of the minimum depends on the interaction strength C, and on the fraction of atoms in the fluid, f.

Displacement of the object potential (V_2) at $t > 0$ induces motion of the object, which leads to the minimum in the background fluid becoming progressively deeper at a rate which increases with v (see Fig. 4.4). When the density minimum reaches zero, it evolves into a vortex ring. This behaviour is reminiscent of that illustrated in Fig. 3.5: the main differences are that here the object is deformable and of finite mass. In the next chapter we shall discuss the vortex ring motion after its creation, while the remainder of this chapter will concentrate on the issue of drag. The motion of the object creates a response in the fluid implying a back action, or drag, on the object. We derive an expression for the drag in the next section and discuss its relationship to the centre-of-mass motion of the object.

4.3.1 Quantum fluid mechanics and drag

In this subsection we will invoke the fundamental connection between the GP equation and the equations of classical fluid mechanics. For example, it is well known that by performing the Madelung transformation (3.8) one can derive a continuity equation and a modified Bernoulli equation [22] from the GP equation. These 'hydrodynamical equations' have proved to be very useful in studies of both homogeneous and trapped Bose condensates: for instance, they were employed by Stringari to elucidate the low-lying collective modes of the condensate [50]. Here we shall use fluid mechanical equations to derive the drag force on a moving object. This may be considered to be a generalisation to a trapped condensate of the result for homogeneous flow around an impenetrable obstacle [84, 86].

We begin by defining the mass density $\rho \equiv mN|\Psi|^2 = mn_c$ and the momentum

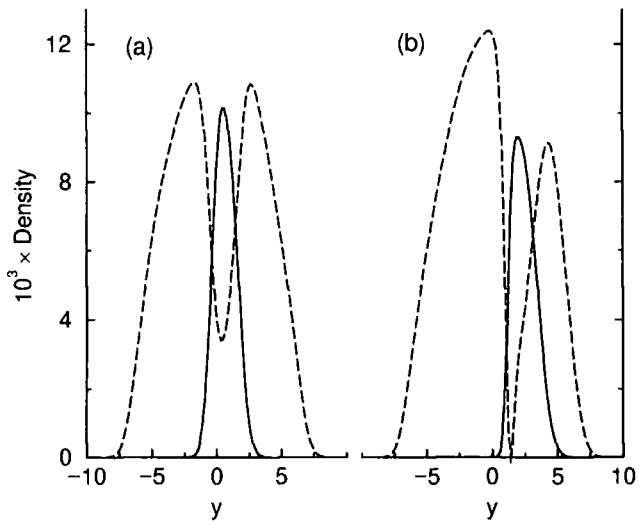

Figure 4.4: Cross-sections through 2D density profiles at $x = 0$. Condensate $|2\rangle$ (the 'object', solid line) moves through $|1\rangle$ (the 'background fluid', dashed), due to displacement of trap potentials at constant velocity, $v = 3$; $C = 1050$, $f = 0.95$ (where f is the fraction of atoms in $|1\rangle$). Two time-frames are shown: (a) $t = 0.75$, where drag arises from a process analogous to phonon emission from the accelerating object, (b) $t = 1.3$, where deformation of the object and surrounding fluid leads to an additional drag.

current density **J**. If the index k denotes the vector component, then $J_k = \rho v_k$, where from (3.9):

$$J_k = \frac{N\hbar}{2i}(\Psi^*\partial_k\Psi - \Psi\partial_k\Psi^*). \tag{4.6}$$

Taking the spatial derivative of J_k, and using the GP equation (2.14) for Ψ and Ψ^* yields:

$$\partial_t\rho + \partial_k J_k = 0, \tag{4.7}$$

while considering the time derivative of J_k gives:

$$\partial_t J_k + \partial_j T_{jk} + \rho\partial_k\left(\frac{V}{m}\right) = 0. \tag{4.8}$$

Equations (4.7) and (4.8) can be immediately recognised as fluid mechanical equations of conservation of mass (i.e. the continuity equation) and momentum [112], where the momentum flux density tensor takes the form:

$$T_{jk} = \frac{N\hbar^2}{4m}(\partial_j\Psi^*\partial_k\Psi - \Psi^*\partial_j\partial_k\Psi + \text{c.c.}) + \frac{N^2 g}{2}\delta_{ij}|\Psi|^4. \tag{4.9}$$

The force on an obstacle moving through a condensate can be calculated from the rate of momentum transfer to the fluid. By integrating equation (4.8), one finds that the k-th component of the force:

$$F_k \equiv \partial_t\int_\Omega \mathrm{d}\Omega\, J_k = -\int_S \mathrm{d}S\, n_j T_{jk} - \int_\Omega \mathrm{d}\Omega\,\rho\partial_k\left(\frac{V}{m}\right), \tag{4.10}$$

where S is a control surface, Ω is the volume enclosed by S, and n_j is the j-th component of the normal vector to S. In the case of homogeneous flow past an impenetrable object, the wavefunction vanishes on the object surface and the potential is uniform elsewhere: hence, only the first term contributes. In contrast, for a penetrable object in a trapped condensate considered here, Ω may be taken to encompass the entire fluid, and the first term is found to be negligible compared to the second. In this case, the drag force creates a back-action on the condensate, which excites centre-of-mass motion in the trap. In particular, choosing S to be the 'surface' of the condensate (where $\rho \to 0$) at some particular instant of time, the centre-of-mass acceleration is related to the drag by $F_k = Nm\ddot{R}_k$. This implies the important relation:

$$\ddot{R}_k(t) = -\frac{1}{m}\int_V \mathrm{d}^3\mathbf{r}\,|\Psi|^2\partial_k V = \frac{1}{m}\int_V \mathrm{d}^3\mathbf{r}\,V\partial_k|\Psi|^2, \tag{4.11}$$

where because $|\Psi|^2 = 0$ at infinity the integration can be taken over all space.

In our 2D simulations on coupled condensates, the potential for component i in h.o.u. is $V = V_i + C|\Psi_j|^2$, where the first term is the trap potential while the

second arises from mean field interactions with the other component. Thus, the acceleration can be treated as being made up of two separate contributions (where motion is considered in the y direction):

$$\ddot{Y}_{i,\mathrm{trap}}(t) = -2 \int \int |\Psi_i|^2 \frac{\partial V_i}{\partial y} \mathrm{d}x \, \mathrm{d}y, \tag{4.12}$$

and,

$$\ddot{Y}_{i,\mathrm{mut}}(t) = -2C \int \int |\Psi_i|^2 \frac{\partial}{\partial y} |\Psi_j|^2 \mathrm{d}x \, \mathrm{d}y. \tag{4.13}$$

The integrations can be evaluated numerically on our computational grid, as the wavefunction is very small at the edges. Considering one condensate as the 'object', the mutual acceleration (4.13) is seen to be particularly interesting in addressing the issue of drag. For steady flow of a homogeneous fluid without vorticity, the drag (4.10) vanishes [84, 86], implying superfluidity. However, for a finite inhomogeneous system there is no steady state and a different criterion should be sought. We now present results for the mutual drag in the case of the coupled two-component system.

4.3.2 Results

Fig. 4.5 shows the calculated mutual acceleration as a function of time. At later times ($t > 2$) the condensates repel due to the inhomogeneity in the background fluid. For $t < 2$ the acceleration is negative, implying an effective attraction, or equivalently a drag on the object. For $t < 1$ and low velocities, Fig. 4.5 (inset), the force results from the slow response of the fluid to the object acceleration. The object moves to the front of the potential well it creates in the mean field of the fluid, resulting in a restoring force which persists until the fluid can respond (Fig. 4.4(a)). The maximum attractive drag (i.e. the minima in Fig. 4.4) is plotted as a function of velocity in Fig. 4.6. This process, which is equivalent to phonon emission by an accelerating object, is responsible for the linear section of the drag curve.

For velocities near to the speed of sound in the object, $c_2 = \sqrt{2C|\Psi_2|^2}$, the object begins to deform, with the result that the overlap between the two fluids is reduced behind and enhanced in front (Fig. 4.4(b)). This increases the drag, producing the additional minima at $t > 1$ in Fig. 4.5 (inset). The onset of this process is rapid with increasing velocity, giving rise to a sharp transition in the drag curve. This transition can be compared to that between superflow and normal flow in the homogeneous system [84, 86]. However, due to the finite size of the background fluid there is no steady flow condition, and drag is produced even at low velocities.

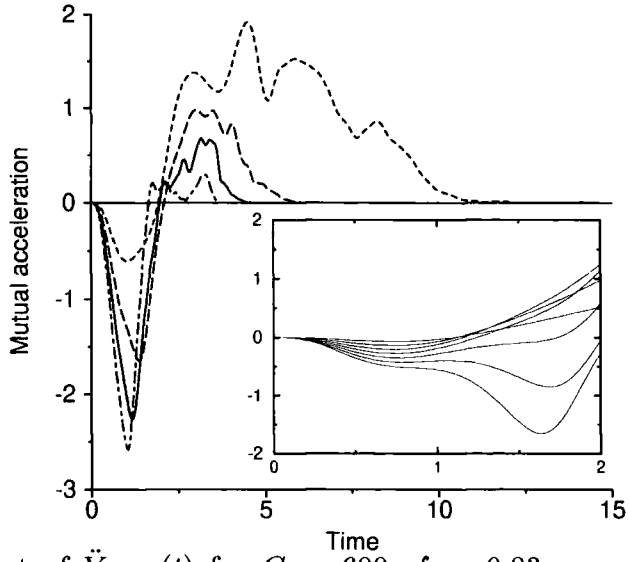

Figure 4.5: Plot of $\ddot{Y}_{2,\mathrm{mut}}(t)$ for $C = 600$, $f = 0.83$; $v = 1, 2, 3, 4$. The 'drag' is evaluated from the minima of the curves, which increases in magnitude as the velocity rises. Inset shows a similar plot ($C = 1050$, $f = 0.95$) for $v = 0.25$ to $v = 1.75$ in steps of 0.25. At low v the local minima arise due to the finite response of the background fluid, $|1\rangle$. At higher v an additional minimum appears at $t > 1$ due to the compressibility of the object. The position of each minimum coincides with the moment of vortex formation.

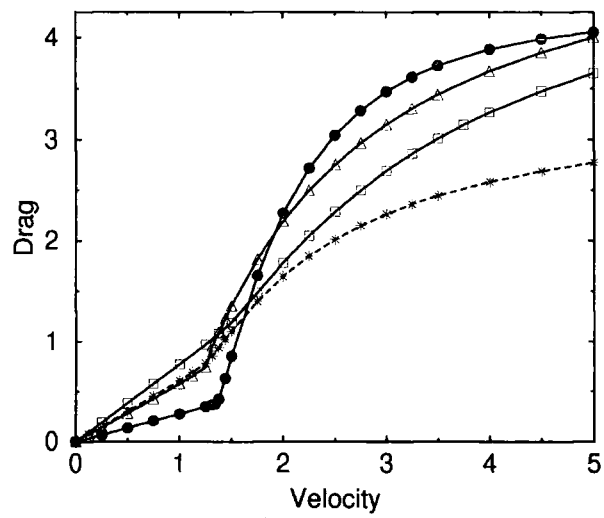

Figure 4.6: Peak mutual attraction (drag) as a function of velocity. Curves are shown for: $*$ $C = 600$, $f = 0.83$; $\triangle$ $C = 1100$, $f = 0.91$; $\square$ $C = 1200$, $f = 0.83$; $\bullet$ $C = 1050$, $f = 0.95$. The curves show linear dependence of drag at low velocities, and enhanced drag at high velocity due to the compressibility of the condensates. The magnitude of the additional drag is enhanced for highly compressible object condensates i.e. when $1 - f$ is small, or when the mean-field interaction between condensates is large.

The drag force increases with time until the local minimum in the background fluid reaches zero (Fig. 4.4(b)), from which a vortex ring is formed. Subsequent expansion of the ring results in the condensate minimum being filled, thereby decreasing the pressure imbalance across the object. The object returns to a more symmetric shape, and the drag decays, as is apparent in Fig. 4.5. Hence, vortex formation in this context tends to limit or reduce the drag.

In summary, we simulate a scheme where one condensate is pulled through another, and identify mutual drag effects, and vortex ring creation which acts to suppress drag. Although vortex rings would be difficult to detect directly, we have shown that they produce a significant change in the mutual drag which could be observable. In principle, the system could also be used for studying superfluidity; however, as we have seen the analysis is complicated by the creation of excitations in the object. In Chapter 6 we will return to the case of a laser beam object, studying the drag as it oscillates within the condensate. In this scenario the object moves along the long axis of the condensate, so that it remains in regions of approximately constant density. This allows us to determine the critical velocity, as well as relating the drag to the rate of energy transfer from the object to the condensate. In addition, the object is now incompressible, so that the transition in the drag-velocity curve is directly associated with the onset of vortex formation.

Chapter 5

Vortex line and ring dynamics

In the last two chapters we have focused on vortex formation by moving objects. In this chapter, by contrast, we will be concerned with the question of what happens to the vortices after their formation. To be exact, we will study the dynamics of quantised vortices in trapped condensates. This subject was touched upon at the end of Chapter 3 where we observed the curved vortex lines undergoing elliptical motion over short timescales after creation. This so-called 'Kelvin wave' is just one example of the normal modes of the vortex, apparent as a spectrum of positive eigenfrequencies when one solves the Bogoliubov equations (3.2) and (3.3) for a vortex state [113, 114, 115]. However, for trapped condensates an eigenmode appears in the excitation spectrum which possesses negative energy with respect to the ground state [under the condition of a positive norm (3.4)]. The existence of this mode therefore implies thermodynamical instability, as the system can arbitrarily lower its energy by creating quasiparticles for that mode. However, some kind of 'reservoir' is required to conserve energy and angular momentum, i.e. a non-condensed cloud. It follows that a vortex in a pure condensate is metastable.

This so-called 'anomalous' mode [116, 117] can be understood physically by realising that the spatial inhomogeneity of the condensate results in a variation of the vortex energy as a function of its position, with a maximum at the centre of a non-rotating trap. As will be discussed later in this chapter, the vortex motion can be related to classical hydrodynamics, with particular reference to the Magnus effect [112]. As a consequence, a single vortex precesses around the condensate centre, which corresponds to the aforementioned anomalous mode. Since the vortex energy decreases as it nears the edge, dissipation at finite temperature will lead to its eventual expulsion from the cloud [118, 119]. This is the physical origin of the thermodynamic instability of the vortex.

This precessional mode tends to be one of highest amplitude and therefore great-

est importance compared to, for example, the Kelvin modes. In this chapter we will study this mode for vortex lines and rings, by numerical solution of the GP equation. First, we will look at the vortex energy as the function of position in non-rotating and rotating frames, and relate this to 2D and 3D measurements of the precession frequency using a Magnus force argument. We will then consider vortex rings, where we find that they also perform a cyclical motion. A stationary state can be found which corresponds to a ring with maximum energy. This point of unstable equilibrium is equivalent to that of a single vortex line in the centre of a non-rotating condensate. We apply this knowledge in order to understand the motion of a vortex ring after formation by an object, as introduced in Chapter 4.[1]

5.1 The vortex state

Before discussing vortex motion, we will continue our introduction to quantised vortices begun in Section 3.1.3. Recall that a superfluid is irrotational everywhere apart from vortices at $\mathbf{r} = \mathbf{r}_{0i}$. In a trapped condensate, a stationary state exists for a single vortex line at $\mathbf{r}_0 = 0$. If for simplicity we assume a non-rotating cylindrically symmetric trap, $V_{\rm trap} = (m\omega_x^2/2)[r^2 + \epsilon z^2]$, then this state can be represented by (3.8) in terms of the quantum number n:

$$\Psi(r, \phi, z) = \sqrt{\rho(r, z)}\mathrm{e}^{in\phi}, \tag{5.1}$$

where here $\rho = |\Psi|^2$. Substitution into the polar form of (2.14) gives:

$$\frac{\partial^2 f}{\partial \tilde{r}^2} + \frac{1}{\tilde{r}}\frac{\partial f}{\partial \tilde{r}} + \frac{\partial^2 f}{\partial \tilde{z}^2} - \frac{n^2 f}{\tilde{r}^2} - \frac{\hbar^2\omega_x^2}{4\mu}(\tilde{r}^2 + \epsilon\tilde{z}^2)f + f - f^3 = 0, \tag{5.2}$$

where $\tilde{r} = (2m\mu)^{1/2}r/\hbar$, $\tilde{z} = (2m\mu)^{1/2}z/\hbar$, and $f = (Ng\rho/\mu)^{1/2} = (\rho/\rho_0)^{1/2}$. Equation (5.2) yields the following asymptotic forms:

$$\rho \simeq \rho_0 \left(\frac{r}{\xi}\right)^{2n^2}, \qquad r \ll \xi, \tag{5.3}$$

$$\rho \simeq \rho_0 \left(1 - \left(\frac{n\xi}{r}\right)^2 - \left(\frac{r}{R_\perp}\right)^2 - \left(\frac{z}{R_z}\right)^2\right), \qquad \xi \ll r < R_\perp, \tag{5.4}$$

and $\rho = 0$ for $r \geq R_\perp$ and $|z| \geq R_z$, where $R_\perp^2 = 2\mu/m\omega_x^2$ and $R_z^2 = 2\mu/m\omega_z^2$. Equation (5.4) is presented in [118, 120, 121] and is analogous to the TF approximation for the ground state in the large Ng limit. However, this approximation

[1] Movies illustrating some of the work covered in this and the next chapter can be found at the web page http://massey.dur.ac.uk/bj/.

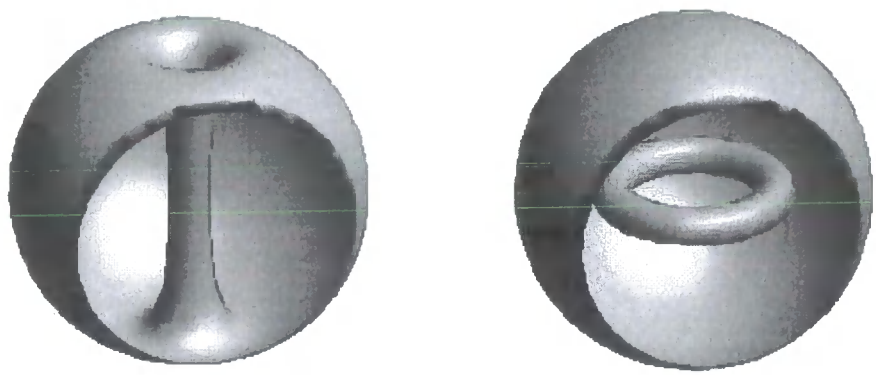

Figure 5.1: Density isosurface plots of $C = 1000$ condensates in isotropic traps ($\epsilon = 1$), where the surface is drawn at $|\Psi|^2 = 1.25 \times 10^{-3}$. Portions of the surfaces are removed to reveal a vortex line (left) and a vortex ring (right).

provides a poor description of the vortex core structure. For the special case $n = 1$, Eqs. (5.3) and (5.4) can be interpolated by a simple function, which generalised to a straight, off-axis vortex at $\mathbf{r}_0$ is:

$$\rho \approx \rho_0 \left(\frac{|\mathbf{r} - \mathbf{r}_0|^2}{|\mathbf{r} - \mathbf{r}_0|^2 + \xi^2} \right) \left(1 - \left(\frac{r}{R_\perp} \right)^2 - \left(\frac{z}{R_z} \right)^2 \right), \tag{5.5}$$

where $\rho = 0$ when the right-hand side is negative.

Imaginary time propagation is used to find the vortex state numerically. A $2n\pi$ phase winding is imposed during the first few time-steps, i.e.:

$$S(x, y, z) = n \arctan\left(\frac{y}{x}\right). \tag{5.6}$$

This imprints the characteristic circulation pattern of a vortex, so that a low density core region rapidly develops in the wavefunction due to centrifugal effects. A three-dimensional isosurface plot in Fig. 5.1 shows the vortex line structure. The core size increases as one moves towards the low-density edge, due to an increase in the healing length ξ (3.13). Off-axis vortices can also be produced using this phase winding technique—however in this case the wavefunction is not a stationary solution, so that the vortex will tend to drift towards the edge in imaginary time. This may be overcome by imposing the phase at all time-steps. Fig. 5.1 also shows a vortex ring, which can be created in cylindrical polar coordinates using this technique. We will discuss ring dynamics in Sec. 5.3.

Fig. 5.2 shows a cross section of a vortex line at $y = 0$, $z = 0$. Equation (5.5) is also plotted for comparison, and is seen to provide a good estimate for

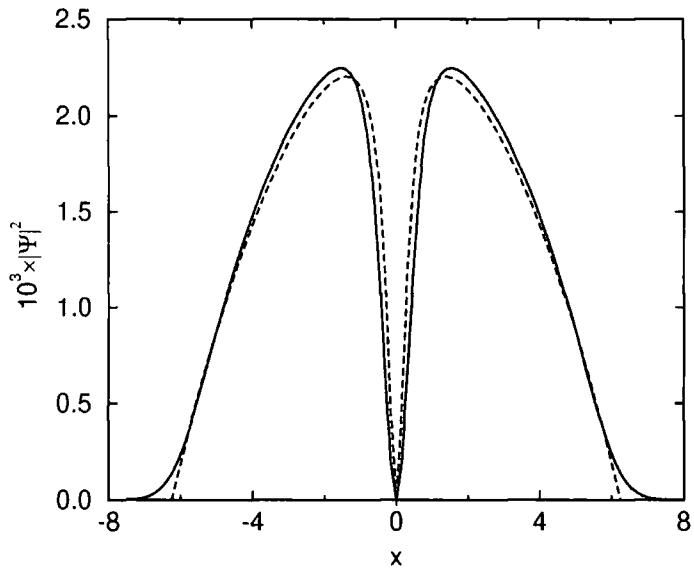

Figure 5.2: Cross-section through a singly quantised vortex line, showing the condensate density as a function of position. The solid line plots the exact 3D wavefunction as calculated from imaginary time propagation of Eq. (5.7), for $C = 4000$, $\Omega = 0$ and $\epsilon = 1$. The dashed line represents the analytic approximation (5.5), with $\rho_0 \simeq 2.443 \times 10^{-3}$, $\xi \simeq 0.3199$, $r_0 = 0$, and $R_\perp = R_z \simeq 6.252$. These parameters are calculated from the Thomas-Fermi chemical potential $\mu_{\rm TF}^{\rm 3D}$ (2.28).

the condensate density, especially in the high N limit. In a similar manner to the TF approximation, the analytical expression breaks down at the outer edges of the condensate, and in addition slightly underestimates the core size. Nevertheless, we will use Eq. (5.5) in our analytical studies later in the chapter.

5.2 Single vortex motion

5.2.1 Two dimensions

In this section we study the dynamics of a singly quantised ($n = 1$) vortex line in a non-rotating condensate. We first generalise our discussion of the previous section to the case of a rotating trap. We consider a frame rotating about the z axis with angular velocity Ω, where the angular momentum operator is given by $L_z = i(y\partial_x - x\partial_y)$. The GP equation in this frame then becomes:

$$i\partial_t\Psi = (-\nabla^2 + V + C|\Psi|^2 - \Omega L_z)\Psi. \tag{5.7}$$

A vortex state can be found using the imaginary time method described previously, but with the rotation operator represented by finite differences (we use a hybrid

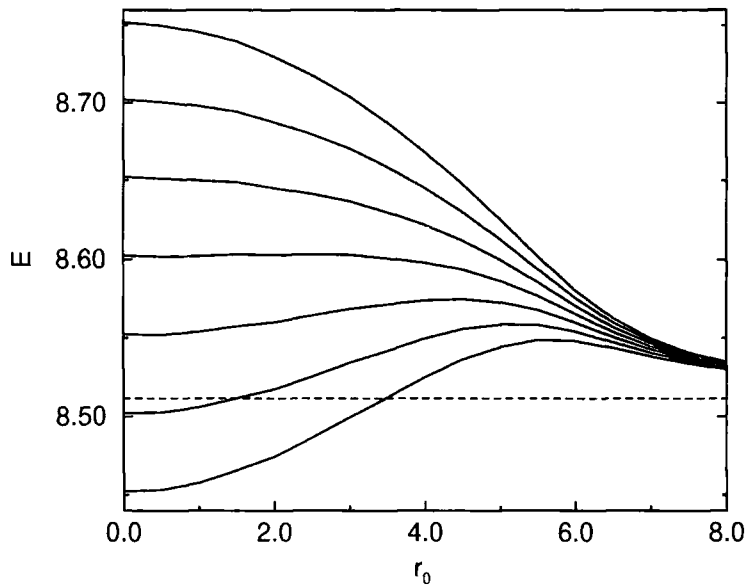

Figure 5.3: Energy, E, as a function of $n = 1$ vortex displacement, in a 2D condensate rotating with angular frequency, Ω ($C = 1000$). The top solid curve corresponds to $\Omega = 0$, where Ω increases in steps of 0.05 as one moves towards the lowest curve. The dashed line marks the energy of the condensate without a vortex, so that the critical angular velocity for a central vortex to become energetically favourable is $\Omega_c = 0.24$.

FFT/Crank-Nicholson code for this purpose—see the Appendix for details). We are also interested in the free energy per particle of the condensate:

$$E = \int \mathrm{d}^3\mathbf{r} \left(|\nabla\Psi|^2 + V|\Psi|^2 + \frac{C}{2}|\Psi|^4 - \Omega\Psi^* L_z \Psi \right). \tag{5.8}$$

For a stationary solution it can be simply shown from (5.7) and (5.8) that:

$$E = \mu - \frac{C}{2}\int \mathrm{d}^3\mathbf{r}\, |\Psi|^4, \tag{5.9}$$

where imaginary time propagation minimises the chemical potential, μ.

If we consider a vortex at position $\mathbf{r}_0$ relative to the axis of a non-rotating trap, then the free energy of the system, Eq. (5.8), is found to attain a maximum when $\mathbf{r}_0 = 0$ (see Fig. 5.3). So, a vortex initially at the origin will remain stationary, but is unstable to infinitesimal displacements. The GP equation implies that the system is Hamiltonian, and therefore an off-axis vortex will follow a path of constant energy corresponding to precession around the trap centre (Fig. 5.4). The presence of dissipation will lead to drift towards lower energies, causing the vortex to spiral out of the condensate [118, 119]. Note that vortex precession in a non-uniform light

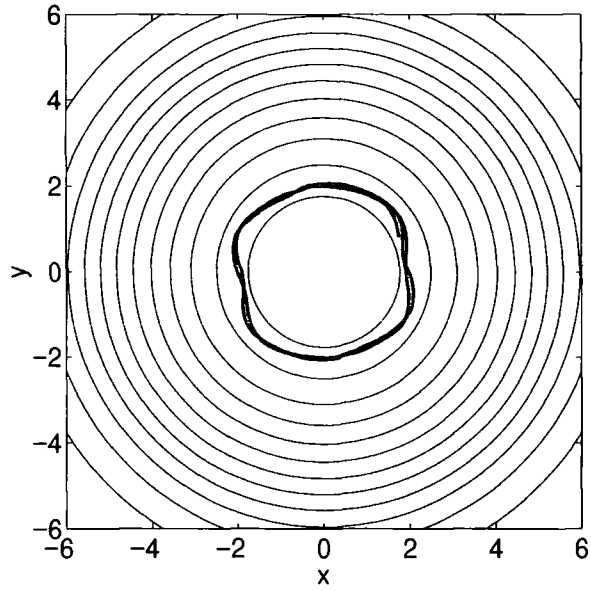

Figure 5.4: Vortex energy in a 2D condensate ($C = 1000$) as a function of position in a non-rotating trap. Twelve energy contours are plotted, equally spaced between 8.5479 and 8.7349. The bold line illustrates the motion of the vortex, which precesses around the energy maximum. The small oscillations in the precession radius is due to centre-of-mass motion of the underlying condensate.

beam has recently been observed and discussed in terms of the nonlinear Schrödinger equation [122].

If the trap is rotated with angular velocity, Ω, then the energy of a central vortex, $E_{\rm rot}$, decreases such that $E_{\rm rot} = E_n - n\Omega$ (see Fig. 5.5 and [115]). This effect is reminiscent of Zeeman splitting in atomic hyperfine levels, where the rotation is analogous to the magnetic field while the condensate angular momentum replaces the magnetic moment of the atom. The appearance of a vortex becomes energetically favourable when $E_{\rm rot} < E_0$, so that the critical angular velocity is simply:

$$\Omega_c = \frac{E_n - E_0}{n\hbar}. \tag{5.10}$$

For $n = 1$ in the TF limit [116, 120, 123]:

$$\Omega_c = \frac{5\hbar^2}{8\mu}(\omega_x^2 + \omega_y^2) \ln\left(\frac{R_\perp}{\xi}\right). \tag{5.11}$$

For $|\Omega| > \Omega_c$, an on-axis vortex attains global stability; however, there remains an energy barrier for vortices entering from the edge (see Fig. 5.3).

Inspection of Fig. 5.3 reveals that above an angular velocity Ω_m, the vortex attains a local minimum, so a vortex is metastable when $\Omega_m < |\Omega| < \Omega_c$. In the TF limit, $\Omega_m = 3\Omega_c/5$ [116], while in the non-interacting limit $\Omega_m \to \Omega_c$ [117]. In

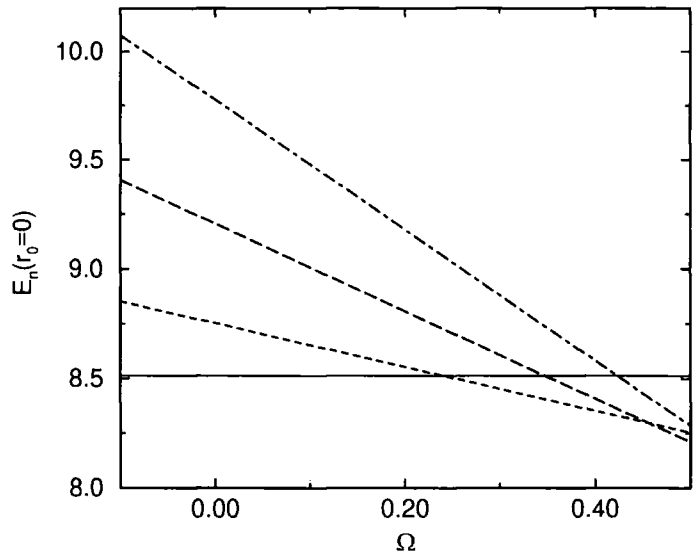

Figure 5.5: Vortex energy at the trap centre, $E_n(r_0 = 0)$, as a function of rotation angular frequency Ω. Results are shown for a singly quantised vortex ($n = 1$, dashed), $n = 2$ (long dashed) and $n = 3$ (dot-dashed), where one can see in each case that $E_{\rm rot} = E_n - n\Omega$. The solid line indicates the energy of the condensate without a vortex.

both the weak and strong coupling limits, $\Omega_m \simeq -\omega_a$, where ω_a is the frequency of the so-called 'anomalous' mode obtained from solution of the Bogoliubov equations [113, 114, 116, 117]. It is thought that ω_a corresponds to the frequency of vortex precession, thus linking vortex dynamics and instability.

First, we consider the simplest case of a vortex in two dimensions, which corresponds experimentally to a condensate confined in an axisymmetric cylindrical trap (where $\epsilon \to 0$). For $\Omega = 0$, simulations show that an off-centre vortex accelerates from its initial condition, soon attaining a near-constant angular velocity ω around the trap centre, such that the instantaneous velocity is $\mathbf{v}_L = \omega\hat{\boldsymbol{\kappa}} \times \mathbf{r}$. The angular velocity, ω, is plotted as a function of interaction strength and initial position in Fig. 5.6. For small C, ω is averaged over a few cycles (e.g. 3 revolutions for $C = 200$). However, for higher C, numerical instabilities arising from the FFT method can restrict the simulations to less than a half-cycle: the error bars reflect the resulting uncertainty.

The precession frequency decreases as a function of increasing interaction strength, C. An intuitive semi-analytical argument for this behaviour can be formulated in terms of the Magnus effect, familiar from classical hydrodynamics and in superfluids and superconductors [124, 125]. When the background fluid flows past the circulat-

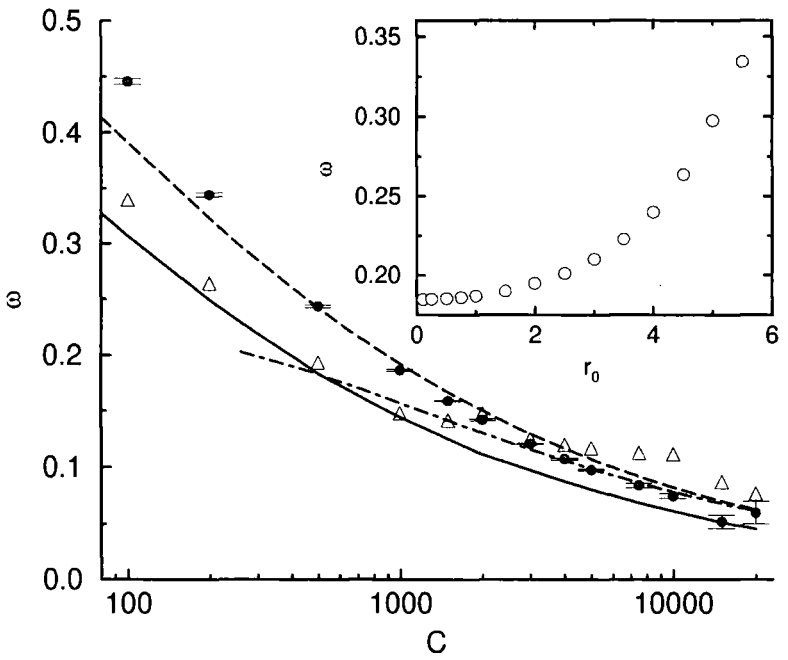

Figure 5.6: Vortex precession frequency, ω, in a 2D condensate at $r_0 = 0.5$, as a function of C. Filled circles show the results of numerical simulations. The triangles indicate the Magnus force estimates, obtained from the gradient of the numerical values of E_0. The analytical Magnus force estimate, Eq. (5.15), and Eq. (5.16) are plotted with dot-dashed and dashed lines, respectively. The TF vortex metastability frequency, $\frac{3}{5}\Delta E$, is plotted as a solid line. Inset: ω as a function of vortex position r_0, for $C = 1000$.

ing fluid connected with the vortex, a pressure imbalance is created perpendicular to the direction of the background flow. The resulting Magnus force must balance the force due to the variation of energy E with position, i.e.:

$$\frac{\partial E}{\partial r_0} = m\rho\boldsymbol{\kappa} \times \mathbf{v}_L, \tag{5.12}$$

where $\mathbf{v}_L$ is the velocity of the vortex line relative to the ambient condensate. Note that the Magnus force can also be produced by flow of the condensate around a stationary vortex, as in a rotating trap. So, one expects that $\omega \simeq \Omega_m$.

We find E by evaluating the functional, Eq. (5.8), using a wavefunction grown in imaginary time with $\Omega = 0$. Performing the Madelung transformation, the first term splits into a 'quantum pressure' and a 'kinetic energy' term: $|\nabla\Psi|^2 = (\nabla\sqrt{\rho})^2 + \rho(\nabla S)^2$. A numerical differentiation of E with respect to r_0 gives an estimate for ω using the Magnus force argument (plotted as triangles in Fig. 5.6). However, these estimates are sensitive to small numerical errors in the energy. To obtain an analytical estimate, we observe that μ is approximately constant at small r_0 and high C. This may be shown by using the decomposition $\Psi(x,y) = \Phi(x,y)\Theta(x,y)$, where an off-set vortex core (Φ) is imprinted on the TF ground-state (Θ), as implied by Eq. (5.5). Starting from the GP equation (2.14), and noting that in the TF limit Θ is slowly varying (i.e. $\nabla^2(\Theta\Phi) = \Theta\nabla^2\Phi$), then it is a simple matter to show that:

$$-\frac{\hbar^2}{2m}\nabla^2\Phi + \mu_{\mathrm{TF}}|\Phi|^2\Phi = \mu\Phi, \tag{5.13}$$

where $\mu_{\mathrm{TF}} = V + Ng|\Theta|^2$. As the Laplacian is spatially invariant, it follows that μ is independent of the offset at small r_0. This can also be justified numerically, though the approximation only becomes valid at high C. Using Eq. (5.9) it follows that:

$$\frac{\partial E}{\partial r_0} \approx -\frac{C}{2}\frac{\partial}{\partial r_0}\left[\int \rho^2 \mathrm{d}^2\mathbf{r}\right]. \tag{5.14}$$

Substituting Eq. (5.5) for ρ then gives an estimate for the precession frequency (to logarithmic accuracy):

$$|\omega| \approx \frac{\hbar\omega_x^2}{\mu}\left[\ln\left(\frac{R_\perp}{\xi}\right) - \frac{5}{4}\right]. \tag{5.15}$$

This result may be compared to the expression obtained by Svidzinsky and Fetter [116], using an asymptotic matching technique and a time dependent variational analysis:

$$|\omega| = \frac{3\hbar\omega_x^2}{4\mu}\ln\left(\frac{R_\perp}{\xi}\right), \tag{5.16}$$

again valid for small r_0. These expressions are plotted together with the numerical results in Fig. 5.6. In addition, we plot $\Omega_m = \frac{3}{5}\Delta E$, where ΔE is the energy

difference between the ground and $n = 1$ vortex states. Recall that one expects that $\omega \simeq \Omega_m$ in the TF limit, and we see a convergence of the frequency data towards the Ω_m curve in the limit of large C. In addition, all of the curves reproduce the correct functional dependence at high C. Note that these expressions are only valid for small r_0; the vortex precesses faster as it nears the edge of the condensate, as shown in Fig. 5.6 (inset).

Compressibility effects become important when the vortex is accelerating or when the velocity is an appreciable fraction of the speed of the sound. In an infinite compressible fluid, phonons may be emitted by a moving vortex, leading to a drift of the vortex to lower energies [126]. On the other hand, no net drift is expected in a finite condensate where excitations remain confined in the region of the vortex. At the beginning of the simulations, we observe an increase in radius of precession, together with excitation of an elliptical centre-of-mass mode at the trap frequency. In addition, surface waves are created when the vortex is near the condensate edge. However, as expected we do not observe a sustained vortex drift (for times up to 110, corresponding to ~ 6 full cycles for $C = 200$). A drift to lower energies would be expected where a thermal cloud damps the motion (i.e. at finite temperatures). Nevertheless, theory predicts long vortex lifetimes, especially for large numbers of atoms [119]. This conclusion is supported by recent experiments, where the lifetime was measured to be approximately 1s in the ENS experiment [72] and exceeding 10s at JILA [74, 127].

5.2.2 Three dimensions

Vortex dynamics become more complex in 3D, as the vortex line can deform along its length. In classical and quantum fluids, this results in the propagation of waves along the line—the so-called Kelvin modes [22]. In simulations of 3D vortex motion, we have observed line deformation and oscillations. However, the inhomogeneity of the condensate complicates matters, and the motion is difficult to resolve into simple Kelvin waves characteristic of the bulk condensate. The amplitude of the oscillations are typically small, and as a consequence waves are likely to be difficult to detect experimentally. Moreover, it is worth noting that the energy of the vortex increases as it lengthens. Hence, in the presence of the dissipation the line will tend to straighten, effectively damping the Kelvin modes.

Fig. 5.7 compares numerically measured values of the precessional frequency with the TF result of Svidzinsky and Fetter, Eq. (5.16) [116]. It can be seen that the frequency dependence is well described; however, the numerical results

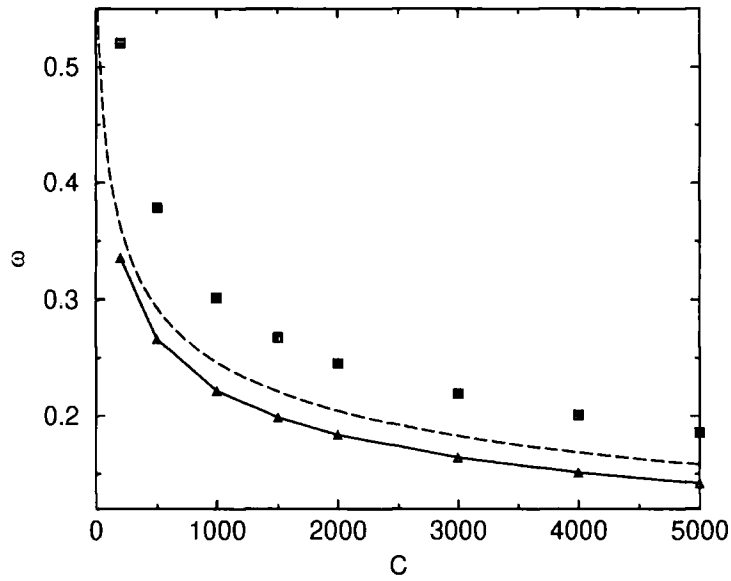

Figure 5.7: Vortex line frequency, ω, in an oblate, spheroidal 3D condensate ($\epsilon = 9$) at $r_0 = 0.5$, plotted as a function of C. Squares display numerical results, while the dashed line plots Eq. (5.16). The solid line shows the TF metastability frequency, $\frac{3}{5}\Delta E$.

are significantly higher ($\sim$ 20%), but converge slowly to the analytical expression towards high C. This disparity may be due to effects resulting from the curvature of the line, which will modify predictions that assume a rigid line motion. Numerical values of the TF metastability frequency, $\frac{3}{5}\Delta E$, are also found to be lower than the observed precession frequencies.

5.3 Vortex ring motion

The motion of a vortex ring in a trapped BEC may be understood in terms of a sum of two contributions to the velocity of each element in the ring. First, the precession due to the inhomogeneity of the condensate, as discussed for a single vortex in the previous section; and second, the velocity induced by the remainder of the ring, $v_{\rm in}$, which is directed along its axis (defined as the z-axis). For a spherical condensate, the total velocity on each element is given by:

$$\mathbf{v} = v_{\rm in}\hat{\mathbf{z}} + \omega\hat{\boldsymbol{\kappa}} \times \mathbf{r}, \tag{5.17}$$

where $\hat{\boldsymbol{\kappa}}$ defines the direction of the circulation at the element, and ω is the precession frequency. In a homogeneous Bose fluid $v_{\rm in} = (\hbar/2mR_r)[\ln(8R_r/\xi) - 0.615]$

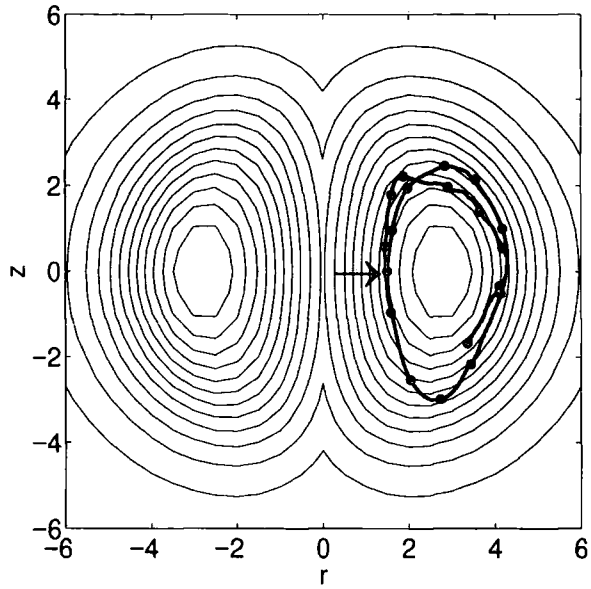

Figure 5.8: Vortex ring energy in a cylindrically symmetric condensate ($\epsilon = 1$, $C = 2000$) as a function of radius, r, and z-position. The energy contours are equally spaced between 5.6179 and 6.1159. The bold line shows the motion of one element of the vortex ring, where the circles represent the position at equally-spaced times (every $T = 1$). The ring begins at $(1.5, 0)$, marked by an arrow, and cycles around the energy maximum in a clockwise direction.

[128], where R_r is the ring radius. Consider a ring at $z = 0$, $r = R_r$. If the radius is small, the induced velocity dominates and the ring moves in the $+\hat{\mathbf{z}}$ direction, while if R_r is large the precession dominates and it travels backwards. In addition, the precessional term leads to ring expansion for $z > 0$ and contraction for $z < 0$. Thus, the two terms produce an oscillatory motion of the ring.

One can also understand the ring motion as a trajectory around an energy maximum, in analogy with the single line vortex. To demonstrate this, we plot the energy of an on-axis ring as a function of its radius, r, and z-position in Fig. 5.8. Without dissipation one would expect the ring motion to follow an energy contour. As is apparent in Fig. 5.8 this is not entirely correct. Acceleration of the ring at the beginning of its motion results in a back-action on the condensate, exciting a centre-of-mass mode, and the subsequent ring dynamics are complicated by the underlying motion of the condensate. In addition, for small C we observe a decay of the ring to lower energies over the first cycle of its motion. As for a single vortex, this effect is associated with the compressibility of the condensate, which results in acoustic emission from the oscillating ring [129].

The energy maximum at $r = R_{\rm eq}$, $z = 0$, corresponds to the point where the two velocity contributions in (5.17) are equal and opposite, leading to a ring in unstable

equilibrium. To obtain an analytical estimate for this position, we approximate the ring energy by taking the energy of a single 2D vortex, E_v, and integrating around a circle of radius R_r, such that $E_r = 2\pi R_r E_v$. The dominant contribution to E_v is given by the kinetic energy, so $E_v = (m/2)\int \mathrm{d}^2\mathbf{r}\rho v_s^2$. Taking $\mathbf{v}_s = \boldsymbol{\kappa} \times \mathbf{r}/2\pi r^2$, where we translate the cylindrical coordinate system so that the origin lies on the vortex axis, and using (5.5) gives:

$$E_r \approx \frac{2\pi^2\hbar^2\rho_0 R_r}{m}\left[\left(1-\frac{r_0^2}{R_\perp^2}\right)\ln\left(\frac{\sqrt{R_\perp^2-r_0^2}}{\xi}\right)+\frac{r_0^2}{R_\perp^2}-\frac{1}{2}\right], \tag{5.18}$$

neglecting terms of order ξ^2 and higher. For a ring of radius R_r at z_0, $r_0^2 = R_r^2 + z_0^2$. This expression describes the qualitative features of Fig. 5.8; however, it tends to over-estimate the energy near to the peak ($\sim 10\%$ at $C = 2000$) and is a poor approximation as $R_r \to 0$. Nevertheless, we can obtain an estimate for the equilibrium position from Eq. (5.18), which yields $z_0 = 0$ and:

$$R_{\mathrm{eq}} \approx R_\perp\sqrt{\frac{\ln(\beta R_\perp^4)-1}{3\ln(\beta R_\perp^4)-4}}, \tag{5.19}$$

where $\beta = (m\omega_x/\hbar)^2$. In the TF limit ($R_\perp \to \infty$), $R_{\mathrm{eq}} \approx R_\perp/\sqrt{3} \simeq 0.577R_\perp$, which is close to the results from numerical solution, where $R_{\mathrm{eq}} \sim 0.54R_\perp$ at high C (Fig. 5.9).

An experimental technique for ring production was proposed in Chapter 4. Recall that the method utilises a two-component BEC, such that when the smaller component, $|2\rangle$, is translated with respect to the other, vortex rings are created in the larger condensate $|1\rangle$. We will now study the subsequent dynamics of the ring by solution of the coupled GP equations (4.3) in cylindrical coordinates. An example of the motion is illustrated in Fig. 5.10. The trajectories roughly follow a contour of constant energy (see Fig. 5.8). The ring is created from zero radius at $t \approx 1.6$ and $y \approx 1.8$. It then expands and travels forward, before turning and progressing backwards along the edge of the condensate. Finally, it turns again and collapses to a point, where the ring is annihilated. The annihilation produces a sound wave, which decreases in amplitude as it propagates along the z-direction. The sound wave then disappears at the edge of the cloud. Note that, in general, annihilation will eventually occur for any ring in the presence of dissipation as a culmination of a decay to lower energies. This is equivalent to the instability mechanism for a single vortex line (Sec. 5.2).

The expansion of the ring immediately after creation is due to the density depression created by the object, which means that the vortex ring energy increases

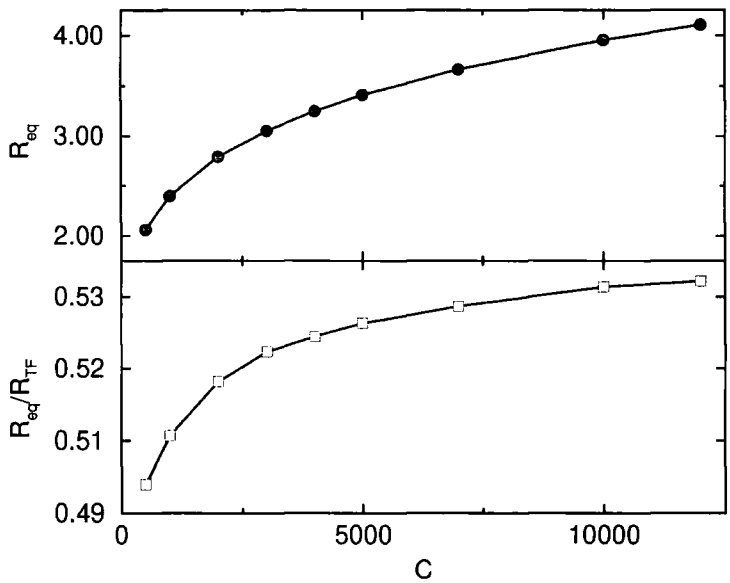

Figure 5.9: The equilibrium ring radius, $R_{\rm eq}$, as a function of C in a spherically symmetric condensate. The lower plot shows the ratio of $R_{\rm eq}$ to the Thomas-Fermi radius, $R_{\rm TF} \equiv R_\perp = (2\mu_{TF}/m\omega_x^2)^{1/2}$.

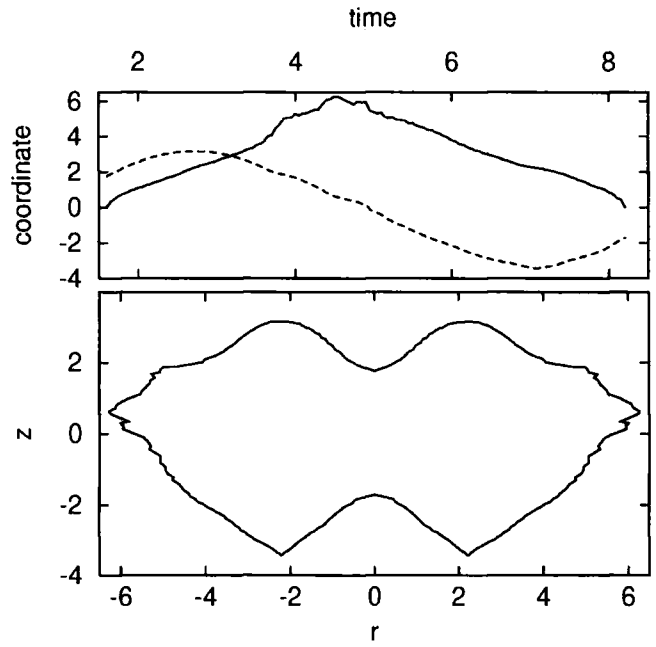

Figure 5.10: Vortex ring motion in a condensate ($\epsilon = 1$) after creation by an object. The trajectory of the ring is determined by solving Eq. (4.3), with $v = 1.75$, $C = 1100$ and $f = 10/11$. The upper plot shows the ring radius (solid line) and z-coordinate (dashed) as a function of time, while a parametric plot (bottom) displays the ring radius, r, against position z.

as one moves away from the object axis. The ring is nucleated behind the axis so that the sense of precession leads to ring expansion. However, after a short time the ring cannot keep pace with the object, so that it no longer influences the vortex motion. The effect of the object is perhaps more clearly illustrated for a single vortex, where near to the object $\partial E_0/\partial r_0 > 0$ rather than $\partial E_0/\partial r_0 < 0$ as in Fig. 5.4. The vortex precession is therefore in the opposite direction to that shown in Fig. 5.4, and the vortex is now stable. This is the basis of proposals to use a laser beam to stabilise a vortex line (see e.g. [130])

Vortex ring detection is likely to present considerable challenges to experimentalists. Absorption imaging after a period of ballistic expansion presents one possibility. However, for rings the density minima at the cores would be obscured by the rest of the condensate along any line-of-sight. A solution would be to view slices of the expanded condensate using light sheets to selectively 'pump' atoms to the desired state. As discussed in the previous chapter, rings may also be detected indirectly by studying the centre-of-mass motion of the coupled condensates, yielding details of the mutual drag that reveal vortex ring formation. One could also speculate whether a vortex ring could significantly change the frequencies of other collective modes. For example, a vortex line lifts the degeneracy of counter-rotating quadrupole modes of the condensate [121, 131]. This results in a precession of the quadrupolar breathing mode (consisting of a superposition of $m = -2$ and $m = 2$ modes) which was utilised in a recent experiment to measure the angular momentum of vortex states [75]. Unfortunately, this scheme is unlikely to work for vortex ring detection as in this case the condensate does not possess a net angular momentum.

Note that the ring dynamics described here are qualitatively similar for vortex pairs, because the energy of a pair also increases as they separate. Our 2D simulations (as discussed in Sec. 3.3) also reveal a vortex precession and eventual annihilation at later times. However, in 3D the dynamics become more complicated due to the ability of the line to stretch and deform (see Sec. 3.4). If more than one pair is produced by the object then they may interact, introducing another layer of complexity to the problem. These issues become relevant in the next chapter, where we return to the scenario of pair formation by a laser beam object.

Chapter 6

Vortex creation and dissipation

This chapter extends our previous simulations to address a recent experiment at MIT by Raman *et al.* [45], where the condensate was probed by an oscillating laser beam. The laser was detuned far above the atomic resonance to produce a repulsive Gaussian potential. The condensate fraction was measured after approximately one second of probing, which indicated significant heating of the cloud only above a critical velocity and therefore a transition to a dissipative regime. The heating was found to depend upon the existence of a condensate, indicating that it must be due to the production of excitations that subsequently populate the non-condensed fraction.

The observation of a critical velocity might suggest the creation of vortices, as shown by our simulations of Chapter 3. However, vortices were not observed in the experiment, probably due to the small core sizes resulting from the high density of the condensate. More indirect evidence must therefore be sought, such as the heating rate and the low value of the critical velocity ($v_c \ll c_s$). The aim of this chapter is to attempt to clarify the role of vortices in the experiment by presenting 2D and 3D simulations of an oscillating repulsive potential in the condensate. The motion transfers energy to the condensate and we observe that the transfer rate increases significantly above the critical velocity for vortex formation. We relate the energy transfer to the drag on the object and characterise transfer below and above the transition as 'phonon' and 'vortex' heating respectively. We also present predictions of the critical velocity as a function of system parameters, furnishing possible experimental tests that could provide further evidence of vortex formation. Finally, we show that the low value of v_c measured experimentally is due to the 3D geometry of the condensate, where vortices are first nucleated at the low density edge. We compare our simulations to other theoretical models of the system, with particular emphasis on the question of critical velocities.

Before describing the results of our simulations we should note that the MIT experiment [45] is just one of several recent studies of superfluidity in trapped Bose gases. For example, vortex formation seems to be possible only for 'macroscopic' objects, and the MIT group has observed suppression of collisions from microscopic impurities below the Landau critical velocity for phonons [70]. Observation of vortices [43, 72] can be seen as a manifestation of the superfluid property of persistent currents, while a scissors mode experiment at Oxford provides a striking demonstration of the irrotational nature of condensate flow [132]. All of these experiments are complementary in pointing towards the existence of superfluid behaviour in these systems: however, as we shall discuss when concluding in Chapter 8, our definition of superfluidity may have to be slightly modified in order to incorporate these new results.

6.1 Simulations

Our simulations are similar to those described in Sec. 3.2, in that we solve the GP equation (3.15) with the object potential given by the Gaussian form (3.20). The position of the centre of the focus in this case is generalised to (0,$y'(t)$,0). To recover the essential physics behind the experiment of Raman *et al.* [45], we describe the oscillatory motion by:

$$y'(T) = \begin{cases} \alpha - vT & \text{if } T < 1/2f, \\ vT - 3\alpha & \text{if } 1/2f \leq T < 1/f, \end{cases} \tag{6.1}$$

where $T = t - s/f$ and s is the number of completed oscillations. The velocity between the motion extrema is constant, $\mathbf{v} = \pm 4\alpha f \hat{\mathbf{y}}$, where α is the amplitude and f is the frequency. The condensate is anisotropic, with its long axis along y ($\eta < 1$). As a result, for small α the beam moves through regions of near-constant density. The initial condition contains the object at $y = \alpha$, which in time dependent simulations nucleates vortices when $v > v_c$.

The creation of phonons or vortices increases the energy of the condensate, which was calculated numerically using the energy functional (5.8). The energy is related to the drag force on the object $\mathbf{F}_{\rm ob}$ by:

$$\frac{\mathrm{d}E}{\mathrm{d}t} = \mathbf{F}_{\rm ob}.\mathbf{v}. \tag{6.2}$$

The drag can be calculated independently over the whole condensate using $\mathbf{F}_{\rm ob} = -\langle \rho \nabla V_{\rm ob} \rangle$ (see Sec. 4.3), allowing a numerical check. Superfluidity corresponds to the situation where E remains constant when $V_{\rm ob}$ is time dependent; i.e. when there

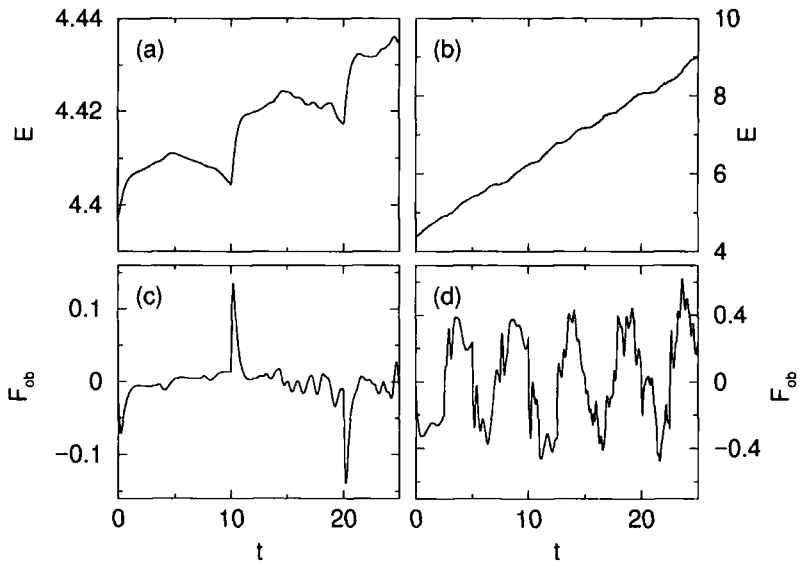

Figure 6.1: Time dependent 2D simulations of laser beam oscillation, with grid spacing of 0.156 (512 × 128 points) and parameters $C = 1000$, $\eta = 0.0625$, $\alpha = 4$, $U_{ob} = 20$ and $\tilde{w}_0 = 1.0$. Condensate energy as a function of time are plotted for (a) $f = 0.05$ and (b) $f = 0.2$. The drag F_{ob} is also plotted for both frequencies in (c) and (d) respectively.

is no drag on the object. Fig. 6.1 shows the energy and drag as a function of time, as calculated for two different frequencies in 2D simulations. At low frequency, the energy transfer is relatively small and characterised by 'jumps' at the motion extrema, whereas at the higher frequency the energy transfer is two orders of magnitude larger and more continuous. Further insight can be gained by considering the drag. At low f, there is little drag except at the motion extrema [Fig. 6.1(c)], while at high f appreciable drag is observed at all times [Fig. 6.1(d)].

To measure the average rate of energy transfer, a linear regression analysis is performed on the energy-time data. The gradients are plotted against v in Fig. 6.2. It can be seen that the curves are characterised by two different regimes. Small energy transfer at low v gives way to enhanced heating above the critical velocity, v_c. At high v, the three plots follow a single linear curve.

Energy transfer below v_c arises due to emission of sound waves at the motion extrema. This process (henceforth referred to as phonon heating) is found to approximately scale with v^3, indicating that at each extremum (which are reached at a rate $\propto v$) a sound wave with energy $\sim v^2$ is emitted. Note that phonon emission by the object is not inconsistent with Landau's criterion. In particular, the Landau argument relies on use of Galilean invariance (Sec. 3.1.2) which breaks down when the condensate density varies, or when the velocity changes abruptly. The process

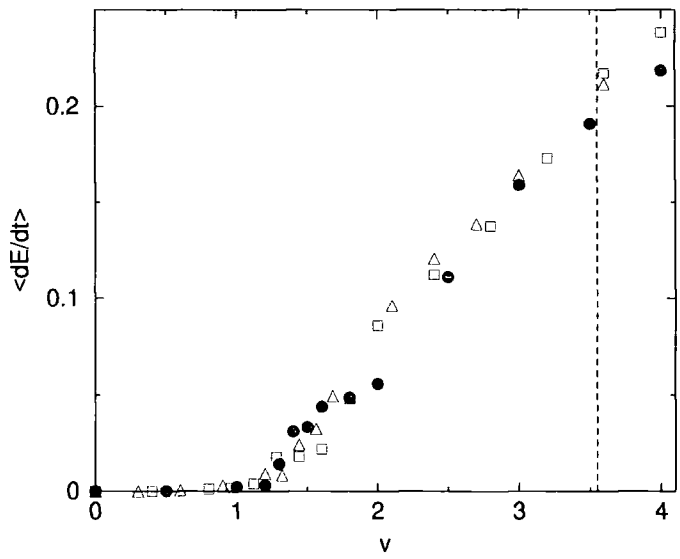

Figure 6.2: Mean rate of energy change as a function of velocity, for $\alpha = 3$ (triangles), $\alpha = 4$ (squares) and $\alpha = 5$ (bullets). Otherwise, parameters are the same as in Fig. 6.1. The dashed line shows the speed of sound in the condensate centre, $c_s = \sqrt{2\mu} \simeq 3.55$. The plot shows a sharp transition between phonon heating (low v) and vortex heating at $v_c \simeq 0.4c_s$.

can also be viewed from the perspective of drag. For constant motion [Fig. 6.3(a)] the fluid is distributed symmetrically around the object, and the net drag is zero. When the object accelerates [Fig. 6.3(b)] the fluid fails to respond rapidly enough to the abrupt change in velocity, and the asymmetry in the overlap between the fluid and the object leads to drag. The fluid then relaxes by the emission of a sound wave.

For the parameters we have explored, phonon heating is found to be relatively small compared to the energy transfer from vortex formation above v_c. The heating rate in the latter regime is found to scale approximately linearly with v. This implies that the drag force is constant. Indeed, we observe that the drag saturates at high v (see Fig. 6.4). This behaviour contrasts with that of steady flow, where the drag $\propto v^k$ (where $k \sim 1$ at v close to v_c, and $k \to 2$ for $v > c_s$) [84, 86]. The difference arises from the oscillatory motion: as the object travels back through its own wake, a large pressure imbalance across the object does not develop.

We can also study the vortex heating process by counting the number of vortices formed above the critical velocity within a fixed time. We find that the shedding frequency scales roughly linearly with v (Fig. 6.5). Fig. 6.6 plots the mean energy transferred against the number of vortex pairs. The energy transfer per vortex pair is approximately constant, leading to estimates of the pair energy plotted as a

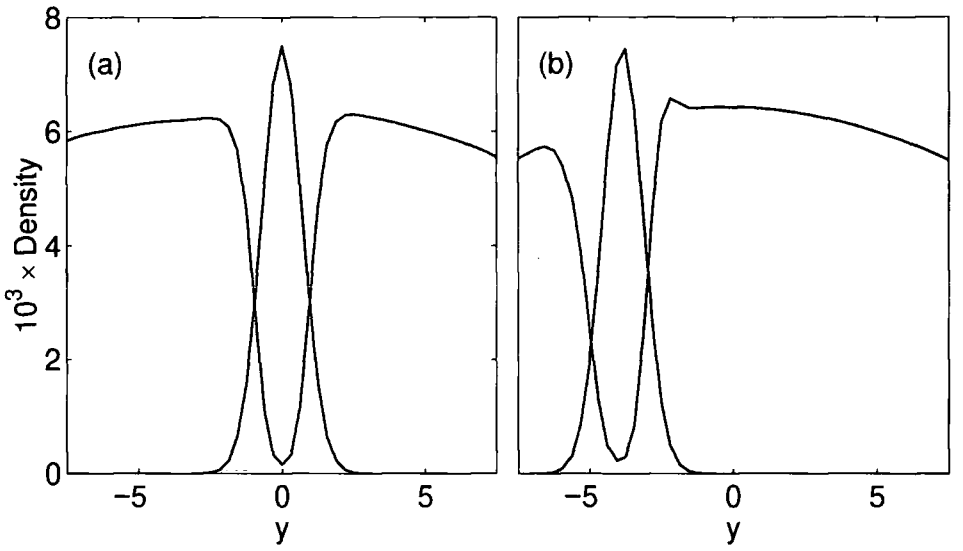

Figure 6.3: Cross-section through the 2D condensate pierced by a Gaussian laser beam 'object' (also shown). (a) If the object is moving with constant velocity $v = v_c$, the fluid density is symmetric around the object, and the drag is zero. (b) When the object accelerates at the motion extremum the fluid cannot adjust sufficiently rapidly, leading to an asymmetric fluid distribution around the object which produces drag (i.e. the second peak in Fig. 6.1(c)).

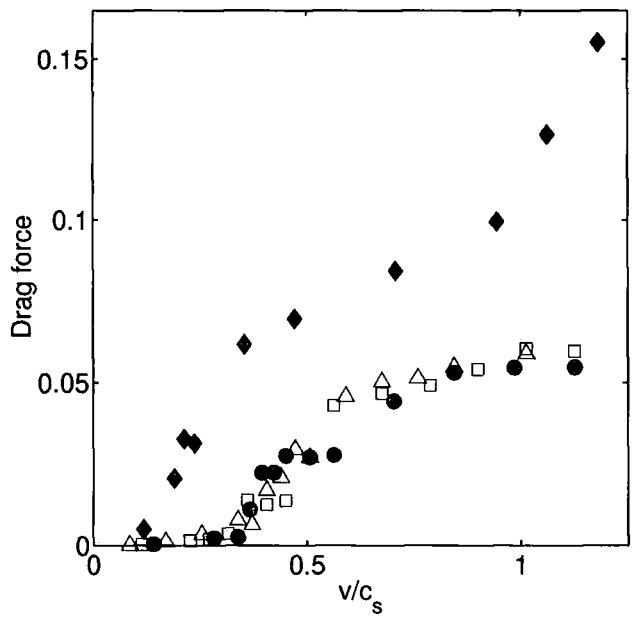

Figure 6.4: The drag force, $\langle \mathrm{d}E/\mathrm{d}t \rangle / v$, as a function of velocity for a $C = 1000$ condensate and $U_{\mathrm{ob}} = 20$ beam. The triangles, squares and bullets correspond to 2D simulations with different oscillation amplitudes (see Fig. 6.2). The diamonds represent 3D simulations.

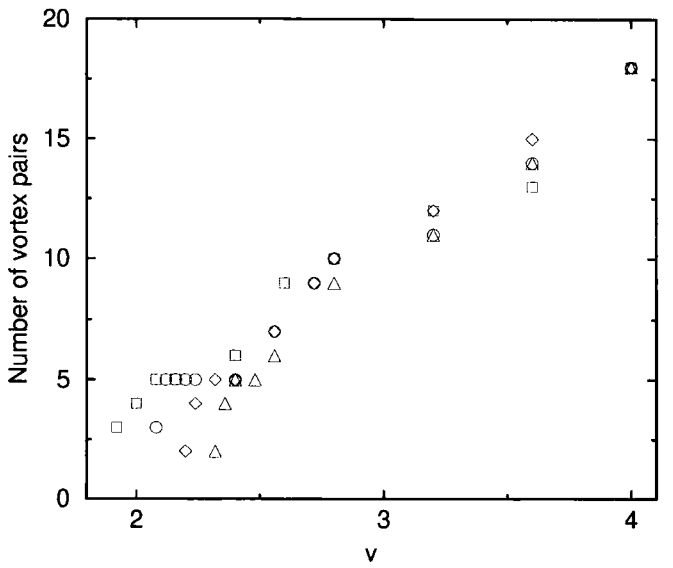

Figure 6.5: Number of vortex pairs created up to $t = 10$ against beam velocity, v. Simulation parameters are the same as in Fig. 6.1, with $\alpha = 4$ and $C = 2000$ (squares), $C = 3000$ (circles), $C = 4000$ (diamonds), and $C = 5000$ (triangles).

function of C in Fig. 6.6 (inset). The energy of a vortex pair in an homogeneous condensate is given by:

$$E_{\text{pair}} = \frac{2\pi\rho\hbar^2}{m} \ln\left(\frac{d}{\xi}\right), \tag{6.3}$$

where ξ is the healing length and d is the distance between the vortices. Equation (6.3) is valid for the inhomogeneous condensate when $\xi \ll d \ll R$, where R is the radial extent of the condensate. Eq. (6.3) with $d = 2\tilde{w}_0$ is plotted in Fig. 6.6 (inset), and is found to agree with the numerical data. Recall that the vortex pair separates immediately after formation, when the pair still resides within the density minimum created by the object. The pair also moves in the direction of the object motion: however, it is slower, and is eventually left behind. At this point, it has an energy approximately equal to E_{pair}, and the formation process is complete. The heating rate can be expressed as $dE/dt = E_{\text{pair}} f_s$ [45]. As the shedding frequency, f_s is approximately proportional to v, then this accounts for the linear dependence of the energy transfer rate.

The subsequent vortex dynamics involve interplay between velocity fields induced by other vortices, and effects arising from the condensate inhomogeneity. In the absence of the object, an isolated pair follows a trajectory similar in character to that of a vortex ring (Sec. 5.3), culminating in self-annihilation. However, the object moves back through its wake, interacting with the original pairs and creating

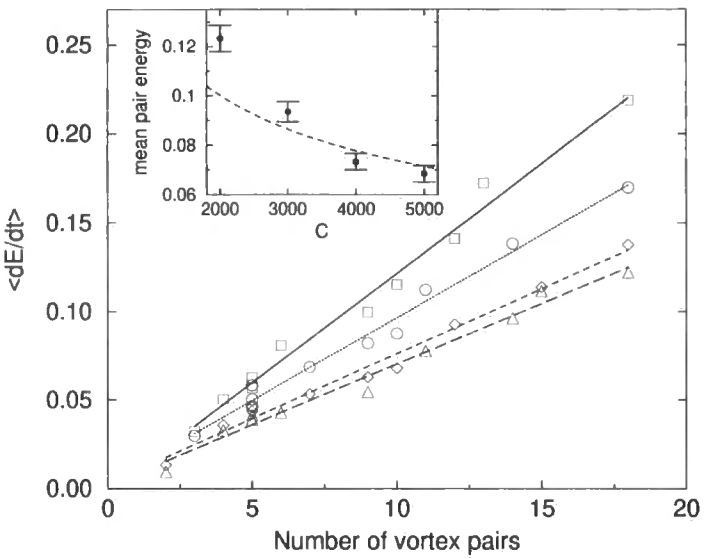

Figure 6.6: Number of vortex pairs created up to $t = 10$ against rate of energy transfer. Simulation parameters and symbols are the same as in Fig. 6.5, with $C = 2000$ (fit with a solid linear regression line), $C = 3000$ (dotted line), $C = 4000$ (dashed), and $C = 5000$ (long dashed). The data points closely follow the regression lines, suggesting a constant energy for each vortex pair. Inset: the average pair energy against C, where the dashed line shows the pair energy predicted by (6.3).

more vortices. The circulation of a pair depends upon the direction of the object motion when it is created (Sec. 3.2). This means that vortex pairs of opposite circulation are formed and interact when sufficiently close. This leads to situations where vortices annihilate or move towards the edge. The number of vortices remaining within the condensate bulk is found to reach an equilibrium value.

The critical velocity for vortex formation, v_c, as a function of potential height and nonlinear coefficient is shown in Fig. 6.7. The critical velocity is not as well defined as in the homogeneous case [84, 85, 86] for a number of reasons. First, a density inhomogeneity along the direction of motion leads to a variation in c_s, and therefore v_c. However, this is less than $\sim 3\%$ in the simulations considered here. The oscillatory nature of the object motion is important. The time taken for a vortex pair to form diverges to infinity as v approaches v_c from above. So, the measured value of v_c increases from its true value as α decreases. In addition, the object travels through its own low-density wake, where c_s is lower. Vortices can therefore be formed after the first half-oscillation, when v is slightly below v_c. Nevertheless, we can obtain a good estimate for v_c by choosing intermediate values of the amplitude (e.g. $\alpha = 4$) and considering only vortex formation during the first half-cycle. Fig. 6.7 demonstrates that v_c decreases as a function of increasing object potential height, $U_{\rm ob}$, allowing an experimental diagnostic for vortex formation at

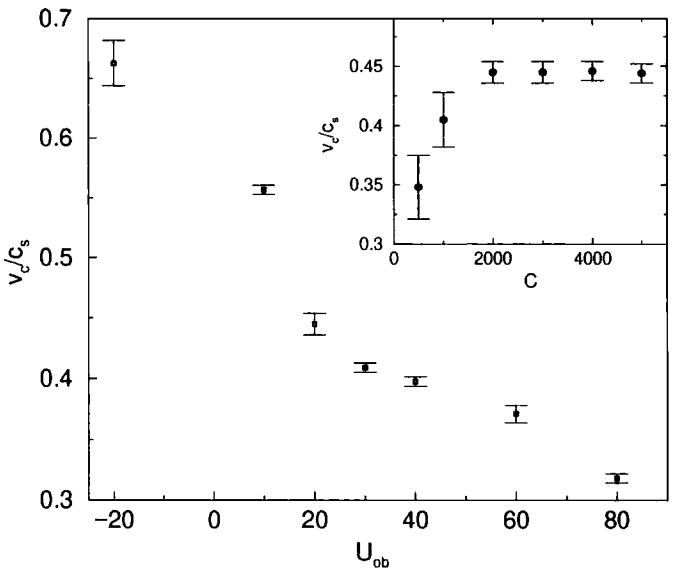

Figure 6.7: Critical velocity for vortex formation at $C = 2000$ as a function of potential height $U_{\rm ob}$, expressed as a fraction of the speed of sound at the condensate centre, c_s. Inset: critical velocity plotted against C, with $U_{\rm ob} = 20$. The other parameters in both plots are $\alpha = 4$ and $\tilde{w}_0 = 1$.

varying beam intensities. This behaviour agrees with simulations of 1D soliton creation [133] and vortex ring formation in 3D [60]. We have also studied the case of $U_{\rm ob} < 0$, which corresponds to a red detuned laser. Fig. 6.7 (inset) shows v_c as a function of C. The critical velocity tends to a constant value as C increases.

Simulations were also performed in 3D. Isosurface stills are shown in Fig. 6.8. We see the condensate immediately after the beam has turned at the extremum ($\alpha = 3$) and an emitted sound wave propagating towards the bottom of the page is clearly evident. A vortex pair is also in the process of formation, where the nucleated lines are highly curved. This is because the beam intersects the condensate edge where the speed of sound is lower. Accordingly, vortex lines first appear in these regions and penetrate into the centre, as shown for a lower v in Fig. 6.9. This leads to a much smaller critical velocity in 3D than in 2D, as shown in Fig. 6.10 where the mean energy transfer rate as a function of velocity is plotted. This conclusion agrees with the experiment [45], where a relatively low critical velocity was measured. Note that to simulate the experiment directly, the appropriate parameters would be: $\epsilon \simeq 0.077$, $\tilde{w}_0 \simeq 3.5$, $U_{\rm ob} \simeq 220$, and $C \simeq 3.6 \times 10^5$. Such simulations require large grid sizes, making them computationally intensive. We therefore attempt to gain some insight by increasing the value of C while keeping the ratio $U_{\rm ob}/\mu_{\rm TF}$ constant and equal to the experimental value $\simeq 6.2$. We see in Fig. 6.10 (inset) that the critical velocity slowly tends to a constant value as C

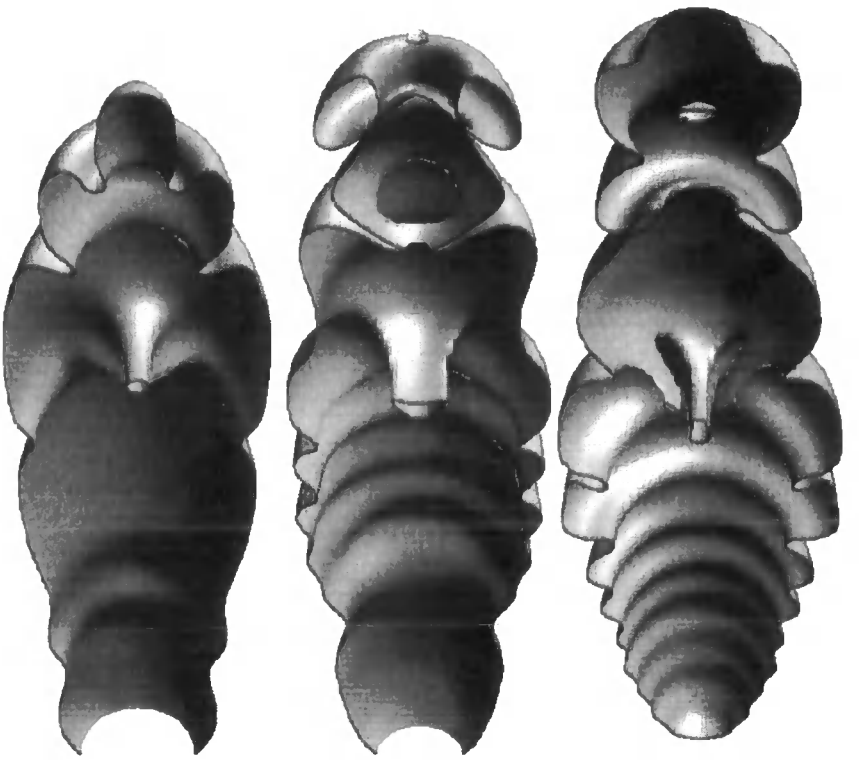

Figure 6.8: Isosurface plots at $|\Psi|^2 = 6 \times 10^{-5}$ showing the creation of a curved vortex pair by a moving object (centre of each picture). Time-frames are shown for (left to right) $t = 10.8$, $t = 12.0$, and $t = 13.2$. The simulation parameters are $v = 1.2$ (*c.f.* speed of sound at the condensate centre, $c_s = 2.54$), $C = 1000$, and $U_{\text{ob}} = 20$.

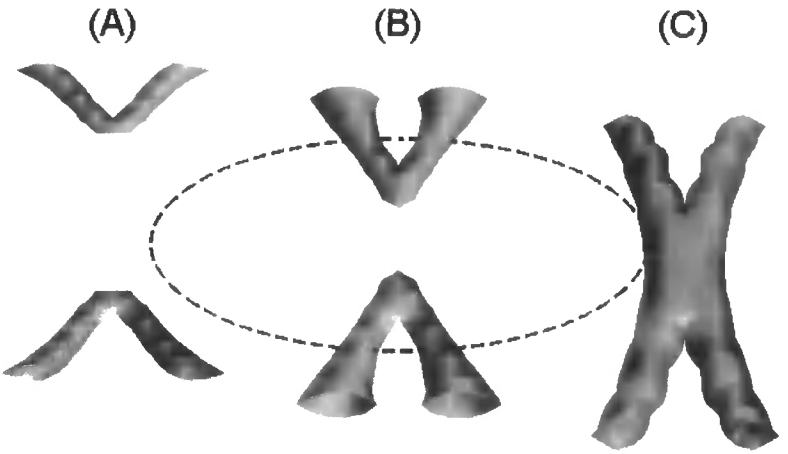

Figure 6.9: Isosurface plots at $v_s^2 = 10^3$, where $\mathbf{v}_s$ is the superfluid velocity, showing the evolution of the vortices at (A) $t = 6.8$, (B) $t = 7.6$, and (C) $t = 8.4$. Also shown in (B) is a dashed circle in the $x - y$ plane with the Thomas-Fermi radius, $R_{\mathrm{TF}} = 3.59$. The direction of beam motion is normal to the circle (i.e. into the paper and towards the bottom). Vortices are seen to nucleate at the condensate edge as half-rings, before penetrating into the bulk to eventually reconnect as a vortex pair. Simulation parameters are the same as in Fig. 6.8, apart from a velocity of $v = 0.6$.

increases. The values are roughly in agreement with the measured $v_c \simeq 0.25c_s$ in the first MIT experiment [45], though improved calorimetric techniques in a more recent experiment [134] suggest a much lower critical velocity of $v_c \sim 0.1c_s$. The difference might be explained by the asymptotic behaviour of v_c as a function of C and U_{ob}: recall that in 2D the v_c-C curve tends to flatten while the v_c-U_{ob} does not. Similar behaviour in 3D might account for the low critical velocity. In addition, dependence of v_c on the beam waist w_0 may be important. In 3D we also see an enhanced heating for $v_c > c_s$, due to phonon emission between the extrema. This difference between 2D and 3D is also apparent in the drag curve plotted in Fig. 6.4.

The experimental system included a significant thermal cloud, which presumably is also heated by scattering from the moving beam. However, the implicit assumption in this chapter (and the experiment) is that the density of the normal component, and therefore the overlap with the beam, is so low that the heating is negligible. We test this supposition by performing a Monte Carlo simulation (see Chapter 7) to model an oscillating laser beam in a classical gas of ^{23}Na, at twice the transition temperature. To compare with our 3D simulations of a condensate, we model $N = 26500$ atoms (equivalent to $C = 1000$) at $T = 110\,\mathrm{nK}$, in a trap with parameters $\omega_x = \omega_y = 2\pi \times 65\,\mathrm{Hz}$ and $\epsilon = 0.0625$, and a beam height

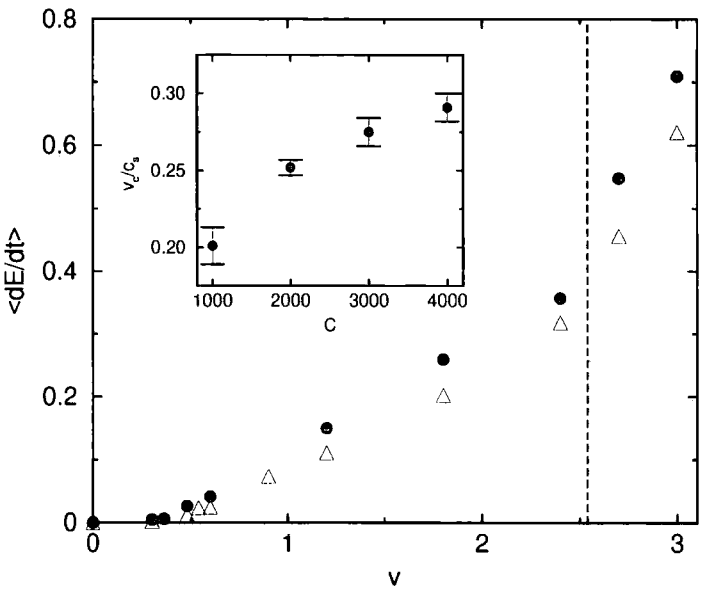

Figure 6.10: Mean rate of energy change versus velocity, for 3D simulations with grid spacing 0.234 ($256 \times 64 \times 64$ points). Parameters are $C = 1000$, $\eta = 0.0625$, $\epsilon = 1$, $\alpha = 3.0$, $\tilde{w}_0 = 1$, and $\lambda \simeq 0.281$. The speed of sound at the condensate centre $c_s \simeq 2.54$ is represented by the dashed line. For $U_{\rm ob} = 40$ (bullets) the critical velocity is $v_c \simeq 0.13 c_s$, while for $U_{\rm ob} = 20$ (triangles) it is $v_c \simeq 0.20 c_s$. Inset: critical velocity as a function of C, where the potential height is adjusted so that the ratio $U_{\rm ob}/\mu_{\rm TF} \simeq 6.2$ is constant.

equivalent to $U_{\rm ob} = 20$. We find from our simulations for $v = 2.4$ h.o.u. over 0.5 s that $\langle {\rm d}E/{\rm d}t \rangle = 2.08 \times 10^{-32}\,{\rm Js}^{-1}$ per atom, which is over two orders of magnitude smaller than the corresponding energy transfer for the condensate, $5.60 \times 10^{-30}\,{\rm Js}^{-1}$ per atom. We expect these conclusions to be unchanged for a Bose gas under the transition temperature. We also see that heating of the thermal cloud and phonon heating of the condensate occur at comparable rates. Thus, to observe phonon heating experimentally one must use clouds at very low temperatures where the thermal fraction is negligible.

6.2 A discussion on critical velocities

We conclude this chapter by discussing other models that claim to account for the experimental observations of critical velocities. We also expand our discussion of vortex formation by reviewing the existing literature on the process in homogeneous systems, showing that vortex nucleation is a general consequence of instabilities in nonlinear Schrödinger flow.

So far theories have focused on the observation of a low critical velocity relative to both the Landau criterion for phonons and the 2D result for uniform flow past a cylinder [84, 85, 86]. In our 3D simulations we have demonstrated that the small value is due to intersection of the beam with low density regions of the condensate where vortices nucleate first. Nore *et al.* [135] simulated 3D uniform flow past a cylinder with a vortex already attached. 'Dissipation' below the 2D critical velocity arises from vortex stretching, where energy from the flow is transferred to the vortex. However, the line always remains fixed to the cylinder so that the process is in principle reversible. Another objection is that the model does not explain how the vortex is created in the first place. The authors suggest thermal or quantum fluctuations may be responsible for nucleation at subcritical velocities. The impact of the non-condensed component on the formation process is very much an open question; however, it is probable that the thermal fraction in the experiment is too low for this effect to be significant.

An alternative explanation for the low critical velocity is that vortices are not responsible at all. The spatial inhomogeneity of the condensate means that sound waves with wavevector $k \sim 1/R$ possess group velocities significantly smaller than c_s [66]. Fedichev and Shlyapnikov [136] solved the Bogoliubov equations in an infinitely long cylindrical condensate to obtain a dispersion curve for phonons. This yielded $v_c < c_s$, where the critical velocity decreased with increasing interaction strengths. For the experimental parameters the authors find that $v_c \approx 0.42 c_s$, which is much

larger than the experimental value. The authors also do not consider the presence of the beam, which is likely to change the modes significantly for these wavelengths. It is not clear whether the modes can be excited by the moving object, or whether they would contribute significantly to the energy transfer. We have found no evidence in our simulations that sound is emitted during constant motion at subsonic speeds.

Two recent papers have recently attempted to find analytical estimates for the critical velocity. Crescimanno *et al.* [137] calculated the energy and momentum of a vortex pair at a separation d, and used the Landau criterion to estimate v_c. As we have seen, vortex pairs emerge from a point near to the axis of a penetrable object, meaning that according to the analysis v_c would diverge to infinity. Their expression for v_c is also largely independent of the density, in contrast to results of simulations and recent experiments [134], and yields a numerical value much lower than that observed. This approach highlights the danger of using the Landau criterion, in that it is a simple energetic argument which provides a lower bound to v_c but ignores completely the nucleation mechanism. As we saw in Chapter 3, vortex formation is a culmination of a complicated process involving evolution of density and phase fields in the region of the object. The important point is that there is a continuous evolution between states without and with vorticity, so that nucleation requires different criteria to that of a simple energy 'jump'. This behaviour is manifest in the dispersion curve for objects in homogenous superflow in two [85] and three [60] dimensions. Laminar flow and vortex solutions occupy different branches separated by an energy barrier, but are joined at the critical velocity by a saddle-node bifurcation. Vorticity can therefore emerge as a continuous trajectory along the curve, with an intermediate state involving a localised low density pulse with no vorticity (termed a 'rarefaction pulse' in the context of freeflow by Jones and Roberts [138]).

A more fruitful approach may be to consider instead the *dynamic stability* of the flow. By performing a linear stability analysis, one can determine the growth rates of the modes in the system. Above criticality the amplitude of one of the modes is found to increase exponentially, signalling instability of the system. This is the basis of the analysis by Stiessberger and Zwerger [139], where the lowest unstable mode is found to be purely complex, corresponding to phase fluctuations which create vortices. Note that stability analyses have also been employed to study vortex formation in superflow past a wall [140] and in a rotating vessel [141], where agreement with numerical simulations is excellent. For uniform flow past a cylinder or sphere, the authors of [139] found that $v_c \propto \hbar/mR$, where R is the radius of the object. Hence, similarly to Crescimanno *et al.* [137], they find that

the critical velocity is independent of the speed of sound. The R dependence is also in disagreement with other work [60, 142, 143], which predicts that the critical velocity is equal to the speed of sound for $R = 0$, while tending to a constant value for $R \to \infty$. These anomalies may arise in their assumption of incompressible flow, in that although it is possible that $v \ll c_s$ at infinity, it is not necessarily true in the region of the obstacle.

We see from the previous discussion that deriving a critical velocity for the experimental situation is in fact a very complex problem, open to many subtleties and misconceptions. Progress has been made, in contrast, on the 'simplified' scenario of uniform flow past an impenetrable cylinder and sphere. The idea here is that vortices nucleate when the flow velocity exceeds the speed of sound *locally* [84]. The flow speed at the equator of the object is a maximum and exceeds the velocity at infinity, accounting for the fact that $v_c < c_s$. This picture must be modified to include the 'quantum pressure', which arises from the curvature of the wavefunction near to the object surface and tends to stabilise the flow. Vortices first appear when the the flow becomes locally supersonic *and* the quantum pressure term is zero at some point a few healing lengths from the surface [144]. This stabilising effect of the wavefunction curvature is responsible for the dependence of v_c on the object radius, as discussed in [142].

A particularly intriguing question is the possible connection, suggested in [145], between the vortex formation in superfluids and the Eckhaus instability in pattern forming systems [146, 147]. In the latter, an order parameter can be defined in terms of an amplitude and phase in a similar manner to a superfluid. The gradient of the phase yields the 'wavevector', $\mathbf{k}$, which remains stable to small perturbations so long as its magnitude remains within a range of values, the 'Busse balloon'. Above the upper limit (the Eckhaus instability boundary, k_E) the system becomes unstable, and a pair of singularities appear and separate. This removes 2π of phase from the pattern, bringing the wavevector back to within the stable range. Although the two systems differ in some respects (pattern forming systems tend to be dissipative, while superfluids as described by the Gross-Pitaevskii equation are conservative), the similarities to the vortex pair formation process in superfluids and between k_E and v_c are compelling. However, quantitative extension of these ideas to more general conditions (e.g. a penetrable obstacle) for comparison to experiment remains a considerable challenge for the future.

Chapter 7

Finite temperature dynamics

Up until now in this thesis we have looked at the dynamics of Bose condensates at low temperatures within the framework of the Gross-Pitaevskii equation. This culminated in the previous chapter in a model of an oscillating laser beam, where we demonstrated that energy is transferred to the condensate by vortex creation. Our analysis, however, is incomplete. Recall that in the MIT experiment [45] heating is observed by a reduction in the condensate fraction. Experimentally, energy (and atoms) must therefore be transferred from the condensate to the thermal cloud. Hence, the observed heating involves the indirect transfer of energy from the object to the thermal atoms, with the condensate acting as an intermediary (recall from Chapter 6 that direct heating is negligible because of the small thermal cloud density). Transfer from the condensate to the thermal cloud is facilitated by damping of excitations; i.e. by decay of moving vortices, or phonons produced by vortex pair annihilation or at the object motion extrema.

The above example highlights the importance in some dynamical scenarios of including finite temperature effects. We touched on vortex decay in Chapter 5, where *mutual friction* [22] between the condensate and non-condensate results in dissipation [119]. Another problem, which has attracted considerable experimental and theoretical attention, is that of the damping of collective excitations. This may be explained in terms of mean-field interactions between the condensate and thermal component, which leads to Landau and Balieav damping. At higher densities, collisions between condensed and non-condensed atoms may also be important. Atoms are transferred between the two components when they are not in diffusive thermal equilibrium with each other, resulting in damping of low-energy excitations of the condensate. This effect is discussed in terms of a hydrodynamic model in [148, 165, 166].

In general, the finite temperature problem is a very difficult one to solve com-

pletely. Approximations must be made in order to render the problem amenable to analytical and numerical treatments. A popular approach involves solving the Hartree-Fock-Bogoliubov (HFB) equations [effectively generalised versions of (3.2) and (3.3)] in order to find the mode frequencies of the condensate in the presence of the thermal component. As we shall discuss later, this method becomes inconsistent at higher temperatures because it neglects the motion of the thermal cloud. In this chapter we account for this by modelling the thermal component using a Monte Carlo approach. The condensate is simulated using the Gross-Pitaevskii equation, which now includes a mean-field from the thermal cloud. In effect, we use a two-fluid model, where the high-energy quasiparticles are treated as a Bose gas within the semi-classical, Hartree-Fock, and random phase approximations, while the low-energy collective excitations are described together with the condensate by the GP equation. This dichotomy between high and low-lying excitations is the essence of our approach. After describing the model, we use it to study mean-field damping of collective modes, and find that our results compare favourably to experimental and theoretical results. We conclude by suggesting future extensions.

7.1 Equations of motion

We begin our discussion of finite temperature dynamics by sketching the derivation of the equations of motion for the condensate and thermal cloud. Further details can be found in e.g. [52, 148]. Our starting point is the system Hamiltonian (2.8), where we again substitute the pseudopotential $\mathcal{U} = g\delta(\mathbf{r}-\mathbf{r}')$. Using the Heisenberg equation of motion and the Bose commutation relations for the field operators:

$$i\hbar\frac{\partial}{\partial t}\hat{\psi}(\mathbf{r},t) = \left(-\frac{\hbar^2}{2m}\nabla^2 + V(\mathbf{r},t)\right)\hat{\psi}(\mathbf{r},t) + g\hat{\psi}^\dagger(\mathbf{r},t)\hat{\psi}(\mathbf{r},t)\hat{\psi}(\mathbf{r},t). \tag{7.1}$$

We now follow Eq. (2.11) by separating the field operator into a condensate part, $\Psi(\mathbf{r},t) = \langle\hat{\psi}(\mathbf{r},t)\rangle$ (recalling that the non-zero ensemble average reflects the underlying broken gauge symmetry) and non-condensate part, $\tilde{\psi}(\mathbf{r},t)$. Substituting (2.11) into (7.1) and taking the expectation value yields an equation of motion for the condensate:

$$i\hbar\frac{\partial\Psi}{\partial t} = \left[-\frac{\hbar^2}{2m}\nabla^2 + V + g(n_c + 2\tilde{n})\right]\Psi + g\tilde{m}\Psi^* + g\langle\tilde{\psi}^\dagger\tilde{\psi}\tilde{\psi}\rangle. \tag{7.2}$$

Subtracting (7.2) from (7.1) gives the equation for the non-condensate field operator:

$$\begin{aligned} i\hbar\frac{\partial\tilde{\psi}}{\partial t} = \left[-\frac{\hbar^2}{2m} + V + 2gn\right]\tilde{\psi} - 2g\tilde{n}\tilde{\psi} + g\Psi^2\tilde{\psi}^\dagger + g\Psi^*(\tilde{\psi}\tilde{\psi} - \tilde{m}) \\ +2g\Psi(\tilde{\psi}^\dagger\tilde{\psi} - \tilde{n}) + g(\tilde{\psi}^\dagger\tilde{\psi}\tilde{\psi} - \langle\tilde{\psi}^\dagger\tilde{\psi}\tilde{\psi}\rangle). \end{aligned} \tag{7.3}$$

The condensate and non-condensate densities are given by $n_c(\mathbf{r},t) = |\Psi(\mathbf{r},t)|^2$ (where Ψ is normalised to N_c in this case) and $\tilde{n}(\mathbf{r},t) = \langle\tilde{\psi}^\dagger(\mathbf{r},t)\tilde{\psi}(\mathbf{r},t)\rangle$, while $n(\mathbf{r},t) = n_c(\mathbf{r},t) + \tilde{n}(\mathbf{r},t)$ defines the total density and $\tilde{m}(\mathbf{r},t) = \langle\tilde{\psi}(\mathbf{r},t)\tilde{\psi}(\mathbf{r},t)\rangle$ is the 'anomalous' off-diagonal non-condensate density. Equations (7.2) and (7.3) form the basis of our discussion of finite temperature dynamics. In the next section we introduce approximations that make the equations more amenable to solution. Note that (7.2) reduces to the GP equation in the absence of the non-condensate ($\tilde{\psi} = 0$).

7.2 Approximations

7.2.1 Hartree-Fock-Bogoliubov (HFB) and Popov approximations

We now take a slight detour by briefly discussing the HFB equations, as they are of particular importance in the finite temperature literature [149, 150, 151, 152, 153]. These are akin to the Bogoliubov equations (3.2) and (3.3) apart from the inclusion of $\tilde{n}$ and $\tilde{m}$, which are neglected within the Bogoliubov approximation. The derivation is similar to that outlined in Sec. 3.1.1 [149], starting from the grand canonical Hamiltonian $\hat{K} = \hat{H} - \mu\hat{N}$, where $\hat{H}$ is given by (2.8), and performing the decomposition (2.11). The key simplification of the HFB mean-field approximation is its treatment of terms cubic and quartic in $\tilde{\psi}$:

$$\tilde{\psi}^\dagger\tilde{\psi}\tilde{\psi} \simeq 2\tilde{n}\tilde{\psi} + \tilde{m}\tilde{\psi}^\dagger, \tag{7.4}$$

$$\tilde{\psi}^\dagger\tilde{\psi}^\dagger\tilde{\psi}\tilde{\psi} \simeq 4\tilde{n}\tilde{\psi}^\dagger\tilde{\psi} + \tilde{m}\tilde{\psi}^\dagger\tilde{\psi}^\dagger + \tilde{m}^*\tilde{\psi}\tilde{\psi}. \tag{7.5}$$

The expanded Hamiltonian can then be diagonalised with the Bogoliubov transformation (3.1), so that:

$$\hat{K}_{\mathrm{HFB}} = \int \mathrm{d}\mathbf{r}\Psi^*(\mathbf{r})\left[-\frac{\nabla^2}{2m} + V + \frac{g}{2}|\Psi(\mathbf{r})|^2\right]\Psi(\mathbf{r}) - \sum_j E_j \int \mathrm{d}\mathbf{r}|v_j(\mathbf{r})|^2 + \sum_j E_j\hat{\alpha}_j^\dagger\hat{\alpha}_j, \tag{7.6}$$

when $u_j(\mathbf{r})$ and $v_j(\mathbf{r})$ satisfy the coupled HFB equations:

$$\begin{pmatrix} \hat{\mathcal{L}} & gm \\ -gm^* & -\hat{\mathcal{L}} \end{pmatrix}\begin{pmatrix} u_j \\ -v_j \end{pmatrix} = E_j\begin{pmatrix} u_j \\ -v_j \end{pmatrix}. \tag{7.7}$$

Here the operator is $\hat{\mathcal{L}} = -\hbar^2\nabla^2/2m + V(\mathbf{r}) - \mu + 2gn(\mathbf{r})$, while $m(\mathbf{r}) = \Psi^2(\mathbf{r}) + \tilde{m}(\mathbf{r})$. Using (3.1) one can verify that:

$$\tilde{n}(\mathbf{r}) = \sum_j \{[|u_j(\mathbf{r})|^2 + |v_j(\mathbf{r})|^2]N(E_j) + |v_j(\mathbf{r})|^2\}, \tag{7.8}$$

$$\tilde{m}(\mathbf{r}) = -\sum_j u_j(\mathbf{r})v_j^*(\mathbf{r})[2N(E_j) + 1], \tag{7.9}$$

where,

$$N(E_j) \equiv \langle \hat{\alpha}_j^\dagger \hat{\alpha}_j \rangle = \frac{1}{e^{\beta E_j} - 1}, \tag{7.10}$$

is the Bose distribution for the quasiparticle excitations. In principle, equations (7.7)-(7.10) can be solved self-consistently with the time independent version of (7.2):

$$[\hat{\mathcal{L}} - gn_c(\mathbf{r})\Psi(\mathbf{r})] + g\tilde{m}(\mathbf{r})\Psi^*(\mathbf{r}) = 0, \tag{7.11}$$

where $\langle \tilde{\psi}^\dagger \tilde{\psi} \tilde{\psi} \rangle = 0$ in the mean-field approximation. We see from (7.8) that the HFB approximation equates the thermal cloud with the spectrum of quasiparticle excitations upon a static ground state condensate. Note also that the thermal density is non-zero even at zero temperatures due to the $|v_j(\mathbf{r})|^2$ term. Physically this is the *quantum depletion* which is so important in liquid ^{4}He. However, in dilute Bose-condensed gases the quantum depletion is very small: less than 1% in current experiments [7].

The HFB approximation satisfies the usual conservation laws for quasiparticle number, energy and momentum [149]. However, according to the Hugenholtz-Pines theorem, the HFB quasiparticle spectrum possesses a gap in the limit of long wavelengths. In other words, $E \neq 0$ at $\mathbf{k} = 0$, where E and $\mathbf{k}$ are the energy and wavevector of the excitation respectively. This is clearly unphysical, but can be remedied by simply setting $\tilde{m} = 0$ in (7.7)-(7.10). This *Popov* approximation is valid at high temperatures ($\tilde{n} \gg \tilde{m}$) and at very low temperatures where both $\tilde{n}$ and $\tilde{m}$ are negligible. The Popov approximation not only yields a 'gapless' spectrum, but also simplifies the self-consistent solution of the HFB equations, and has been used to calculate the excitation frequencies of the condensate at finite temperatures [150, 151]. Note that gapless spectra can also be obtained by variational expansion to higher terms than in the first-order HFB approximation, or by renormalisation of the coupling constant, g [154, 155, 156].

Another limitation of the HFB approximation is of particular importance to our discussion. The approximation treats excitations in the condensate, but neglects collective motion of the non-condensed thermal cloud. This can lead to unphysical

behaviour at higher temperatures where the thermal component is large. For example in Refs. [150, 151] the frequency of the centre-of-mass dipole mode was found to deviate slightly away from the trap frequency as the temperature increased. This is in defiance of the generalised Kohn theorem [157], which states that a cloud in a harmonic potential undergoes rigid-body oscillations at the trap frequency. This limitation is also of considerable importance when comparing frequencies and damping rates to experiments [4, 109, 158], as coupling between the condensate and thermal cloud is expected to play an important role at temperatures approaching the transition. We shall return to this point later.

7.2.2 Semi-classical approximation

To solve the HFB equations, one must solve a set of $2j+1$ equations self-consistently up to some cut-off energy. This is time-consuming but can be simplified greatly by using a semi-classical approximation [159], where in a harmonic trap of frequency ω_0 the discrete energy levels can be replaced by a continuous function $\epsilon_{\rm HF} = p^2/2m + V(\mathbf{r}) + 2gn(\mathbf{r}) - \mu$ (which corresponds to the energy of a single particle moving within the mean-field). As discussed in Sec. 2.1.1, the semi-classical approximation is expected to be valid under the condition that $k_B T \gg \hbar\omega_0$ and when the number of trapped atoms is large. Indeed, results of the semi-classical approximation agree favourably with those of a comprehensive path-integral Monte Carlo calculation [160]. The calculations also rely upon the local density approximation, under which the condensate is assumed to vary sufficiently slowly so that the thermal density $\tilde{n}(\mathbf{r},t)$ is determined entirely by the local potential and temperature, and can therefore be treated locally as if the gas were homogeneous. Note that $\epsilon_{\rm HF}$ represents the Hartree-Fock spectrum, which neglects low-lying collective modes. However, here we shall consider the thermodynamic properties in equilibrium, where single-particle excitations are overwhelmingly more important [7]

In the Popov approximation, Eq. (7.2) reduces to:

$$i\hbar\frac{\partial}{\partial t}\Psi(\mathbf{r},t) = \left(-\frac{\hbar^2\nabla^2}{2m} + V(\mathbf{r},t) + gn_c(\mathbf{r},t) + 2g\tilde{n}(\mathbf{r},t)\right)\Psi(\mathbf{r},t), \tag{7.12}$$

which is similar to the Gross-Pitaevskii equation, but with an additional term $\tilde{n}(\mathbf{r},t)$ representing the non-condensate density. Within the semi-classical approximation the summation in (7.8) can be replaced by an integration $\sum_j \rightarrow \int \mathrm{d}\mathbf{p}(2\pi\hbar)^{-3}$, so that:

$$\tilde{n}(\mathbf{r}) = \frac{1}{(2\pi\hbar)^3}\int \frac{\mathrm{d}\mathbf{p}}{z^{-1}\mathrm{e}^{\beta p^2/2m} - 1}, \tag{7.13}$$

where the fugacity $z = \exp[-\beta\{V(\mathbf{r}) + 2gn(\mathbf{r}) - \mu\}]$. Integrating yields:

$$\tilde{n}(\mathbf{r}) = \frac{1}{\lambda_T^3} g_{3/2}(z), \tag{7.14}$$

where $\lambda_T = (2\pi\hbar^2/mk_BT)^{1/2}$ is the thermal wavelength, and $g_\alpha(z) = \sum_{l=1}^{\infty} z^l/l^\alpha$. The total number of atoms in the system is then given by $N = N_c + \int \tilde{n} d\mathbf{r} = N_c + \tilde{N}$, where N_c and $\tilde{N}$ are the numbers in the condensate and thermal cloud respectively.

Self-consistent solution of (7.12) and (7.14) yields good approximations for the condensate and non-condensate densities at equilibrium. The following numerical procedure is implemented:

(i) Eq. (7.12) is solved for a particular N_c and with $\tilde{n} = 0$, using imaginary time propagation. This yields $n_{c0}(\mathbf{r})$ and μ_0.

(ii) Eq. (7.14) is evaluated for a particular value of T, with $n_{c0}(\mathbf{r})$ and μ_0 from step (i). This yields new values for $\tilde{n}(\mathbf{r})$ (discretised on the same grid as the GP equation) and $\tilde{N}$.

(iii) Step (i) is repeated with the new value for $\tilde{n}(\mathbf{r})$. This then yields new values of $n_c(\mathbf{r})$ and μ for step (ii), and so on. Iteration continues until μ and $\tilde{N}$ converge to a predetermined tolerance, typically $\text{Error}(\mu) < 10^{-7}$ and $\text{Error}(\tilde{N}) < 10^{-3}$.

(iv) To obtain a desired value of $N = N_c + \tilde{N}$, a further level of iteration is utilised. After obtaining $\tilde{N}$ from steps (i)-(iii), $\tilde{N}$ and N_c are rescaled thus: $\tilde{N} = \tilde{N}/N$ and $N_c = N_c/N$. Steps (i)-(iii) are repeated, and iteration continued until constant N is achieved to a tolerance: $\text{Error}(N) < 10^{-2}$.

For a particular N, the initial value of N_c may be found using the relation for the condensate fraction as a function of temperature (2.7) for non-interacting atoms in the thermodynamic limit. However, a more accurate initial condition is yielded by including mean-field interactions between condensed atoms. An analytical estimate can be derived from the semi-classical approximation, but with interactions between the thermal atoms neglected [161]:

$$\frac{N_c}{N} = 1 - \left(\frac{T}{T_c^0}\right)^3 - \frac{\zeta(2)}{2[\zeta(3)]^{2/3}}(15N^{1/6}a)^{2/5}\left(\frac{T}{T_c^0}\right)^2\left[1 - \left(\frac{T}{T_c^0}\right)^3\right]^{2/5}. \tag{7.15}$$

Results of the calculations for 20000 ^{87}Rb atoms in a spherical trap are plotted in Fig. 7.1. The density plots in Fig. 7.1(a) show that the thermal cloud is more spatially extended and less dense than the condensate, tending to occupy a 'shell' around the condensate. Fig. 7.1(b) plots the condensate fraction as a function of temperature: the condensate can be seen to be depleted at all temperatures due to interactions. The numerical data also follow closely the result of (7.15), where

a Newton-Raphson iteration was used to evaluate the condensate fraction at each temperature. Note that there are no numerical results at temperatures just below T_c: this is due to divergence of the Bose function ($z > 1$) at the condensate surface where the density is small.

Figures 7.2 and 7.3 show results for a cylindrically symmetric condensate with similar parameters to the first JILA experiments: $N = 20000$, $\omega_x = \omega_y = 2\pi \times 131\text{Hz}$ and $\omega_z = \omega_x/\sqrt{8}$ [1, 162]. Fig. 7.2 shows the same dependence of condensate fraction on T as Fig. 7.1(b), while Fig. 7.3 displays the column densities: $n_{\text{col}}(x, z)$ (with the probe beam directed along the y-axis). The plot shows the familiar sequence of images as the gas cools: just below T_c there appears a bimodal distribution with a parabolic condensate superimposed upon an extended thermal cloud, where the latter disappears at lower T. The plots also show that there is a substantial column density of thermal cloud near to the trap centre for higher temperatures.

7.2.3 The kinetic equation

The HFB-Popov equations discussed in Sec. 7.2.1 have been successfully solved to find the collective mode frequencies of the condensate at finite temperatures [150, 151]. However, as mentioned in our discussion, this approximation neglects the dynamics of the thermal cloud, which is of particular importance when addressing higher temperatures. Bijlsma and Stoof [163] have utilised a variational method to include coupling between the condensed and non-condensed fractions in the collisionless regime, while Zaremba, Nikuni and Griffin [148, 164, 165, 166] have considered the hydrodynamical regime and derived coupled equations analogous to the Landau two-fluid equations. Initially only collisions between thermal atoms were included in this treatment [164], corresponding to the case where the two fractions are in local equilibrium with each other. However, in [148, 165, 166] the model was extended to include collisions between condensed and thermal atoms (i.e. exchange of atoms between the two components). This was used to predict hybridisation between the collective modes of the two components, which may be responsible for the anomalous behaviour of the condensate quadrupole frequencies at high temperatures [109].

While the hydrodynamical equations are of considerable interest when studying high density systems such as ^{4}He, experimental Bose-condensed gases tend to reside in the collisionless regime [5], or between the collisionless and hydrodynamical regimes [4]. It would therefore be useful to have a model which is not dependent upon assumptions about collision times or local equilibrium conditions. One ap-

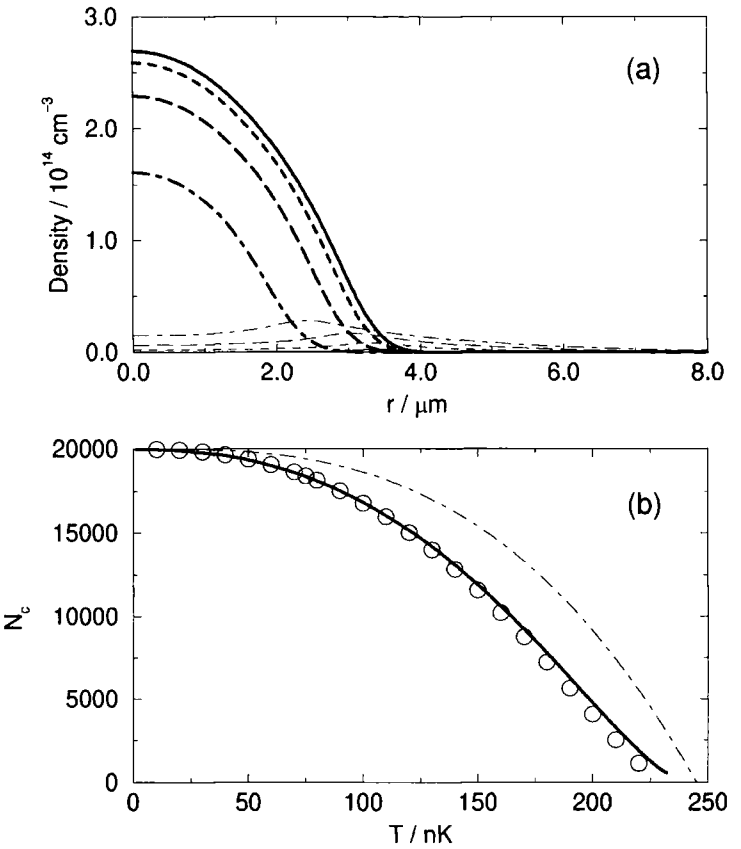

Figure 7.1: (a) The condensate (bold) and non-condensate (faint) densities for $N = 20000$ ^{87}Rb atoms in a spherical trap of frequency $\omega = 2\pi \times 200$ Hz, at temperatures $T = 50$nK (solid), $T = 100$nK (dashed line), $T = 150$nK (long dashed), and $T = 200$nK (dot-dashed), where $T_c^0 = 245\,\mathrm{nK}$. (b) The number of atoms in the condensate as a function of temperature. Circles plot the numerical results, while the lines plot the analytical functions: (dot-dashed line) in the non-interacting limit (2.7), and (solid line) with interactions between condensate atoms (7.15).

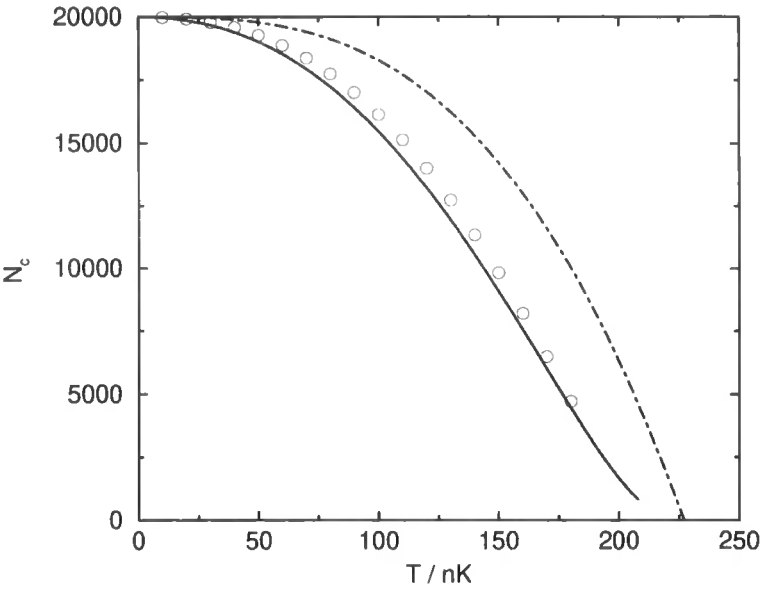

Figure 7.2: The number of condensate atoms as a function of temperature, for $N = 20000$ atoms in a cylindrically symmetric trap. As in Fig. 7.1(b), the circles, dot-dashed and solid lines represent numerical results, Eqs. (2.7) and (7.15) respectively.

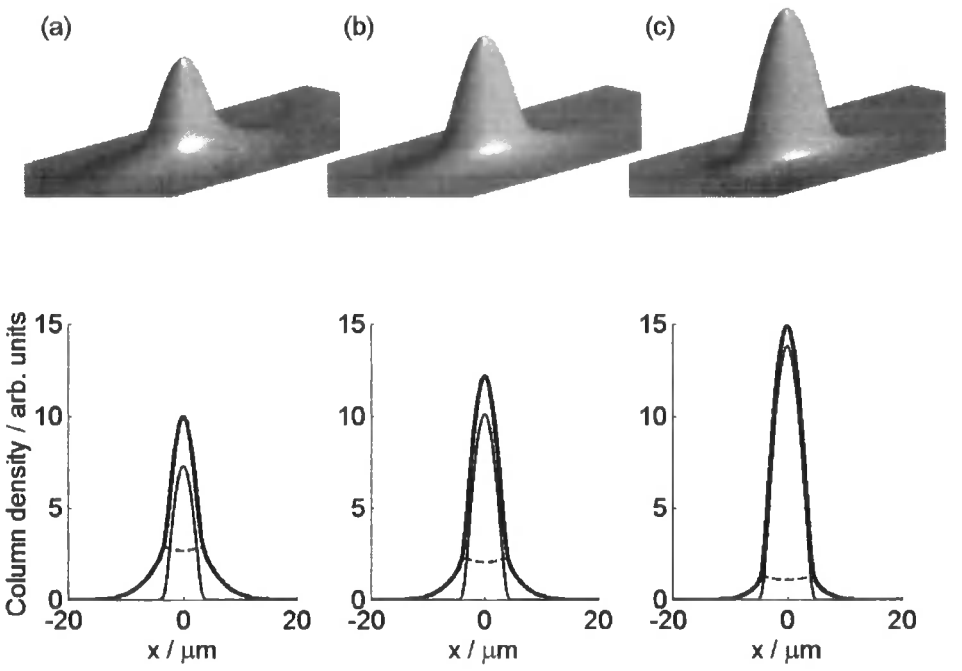

Figure 7.3: Column densities for (a) $T = 180\,\mathrm{nK}$, (b) $T = 160\,\mathrm{nK}$, and (c) $T = 120\,\mathrm{nK}$. The total densities in x and z are shown in the top plots, while cross-sections are shown in bold in the bottom plots. In addition, the condensate and non-condensate column densities are plotted with solid and dashed lines respectively.

proach is to consider thermal cloud dynamics in terms of transport processes using a Boltzmann kinetic equation, which includes stimulated Bose scattering to reflect the quantum nature of the gas. The kinetic equation can be derived from the equation of motion (7.3) under the semi-classical approximation. The starting point is the Wigner function:

$$f(\mathbf{p},\mathbf{r},t) = \int \mathrm{d}\mathbf{r}' \mathrm{e}^{i\mathbf{p}\cdot\mathbf{r}'/\hbar} \left\langle \tilde{\psi}^{\dagger}\left(\mathbf{r}+\frac{\mathbf{r}'}{2},t\right)\tilde{\psi}\left(\mathbf{r}-\frac{\mathbf{r}'}{2},t\right)\right\rangle, \tag{7.16}$$

which defines a quantum mechanical analogue of the classical distribution function. Accordingly, the non-condensate density is given by:

$$\tilde{n}(\mathbf{r},t) = \int \frac{\mathrm{d}\mathbf{p}}{(2\pi\hbar)^3} f(\mathbf{p},\mathbf{r},t). \tag{7.17}$$

Assuming that $U_{\mathrm{eff}}(\mathbf{r},t) = V(\mathbf{r},t)+2gn(\mathbf{r},t)$ varies slowly in space (where excitation energies are considered on the level of the Hartree-Fock approximation) one can derive a kinetic equation for the gas:

$$\frac{\partial f(\mathbf{p},\mathbf{r},t)}{\partial t} + \frac{\mathbf{p}}{m}\cdot\nabla f(\mathbf{p},\mathbf{r},t) - \nabla U_{\mathrm{eff}}\cdot\nabla_{\mathbf{p}} f(\mathbf{p},\mathbf{r},t) = \left.\frac{\partial f}{\partial t}\right|_{\mathrm{coll}}. \tag{7.18}$$

The second and third terms on the left-hand side define the so-called free-streaming operator, while the right-hand term gives the scattering rate out of state $\mathbf{p}$. The collisionless Boltzmann equation ($\partial f/\partial t|_{\mathrm{coll}} = 0$) can be readily derived *via* a Green's function analysis within the Hartree-Fock approximation (see e.g. Chapter 7 of Ref. [52]). This is equivalent to (7.3) with only the term in square brackets on the right-hand side. The particles in the HF approximation travel without colliding through a potential consisting of external fields and the mean-field from the other atoms. It is important to note that here we consider the thermal gas to be composed of atoms rather than quasiparticle excitations as in the Bogoliubov picture. Indeed, in the HF approximation the two approaches are equivalent, as one treats only the high-energy single particle excitations. As a result, the particle and quasiparticle distribution functions coincide [159]. This treatment of the thermal cloud as a gas of particles is the basis of our Monte Carlo simulations, as described later.

The derivation of the collision integrals on the right-hand side of (7.18) is more difficult, involving evaluation of higher-order terms in the equation of motion (7.3) (see Appendix A of Ref. [148] for details). Using the notation of [148] the collisional term can be written:

$$\left.\frac{\partial f}{\partial t}\right|_{\mathrm{coll}} = C_{12}[f] + C_{22}[f]. \tag{7.19}$$

The second term represents two-body collisions between atoms in the thermal cloud within the Born approximation [52]:

$$C_{22}[f] = \frac{2g^2}{(2\pi)^5\hbar^7}\int d\mathbf{p}_2 \int d\mathbf{p}_3 \int d\mathbf{p}_4 \delta(\mathbf{p}+\mathbf{p}_2-\mathbf{p}_3-\mathbf{p}_4) \times\delta(\tilde{\epsilon}_p+\tilde{\epsilon}_{p_2}-\tilde{\epsilon}_{p_3}-\tilde{\epsilon}_{p_4})[(1+f)(1+f_2)f_3f_4 - ff_2(1+f_3)(1+f_4)], \quad (7.20)$$

with $f \equiv f(\mathbf{p},\mathbf{r},t)$ and $f_i \equiv f(\mathbf{p_i},\mathbf{r},t)$. Locally, an excited atom has the HF energy $\tilde{\epsilon}_p(\mathbf{r},t) = p^2/2m + U_{\rm eff}(\mathbf{r},t)$. We immediately see that this is the ordinary Boltzmann equation for a Bose gas in the absence of the condensate (see also Chapter 9 of [52] for a derivation). The collision integral here differs from that of a classical gas [31] by the inclusion of $(1+f_i)$ factors that represent Bose enhancement of scattering into occupied states. The first collision integral in (7.19) involves a condensate atom:

$$C_{12}[f] = \frac{2g^2 n_c}{(2\pi)^2\hbar^4}\int d\mathbf{p}_1 \int d\mathbf{p}_2 \int d\mathbf{p}_3 \delta(m\mathbf{v}_c+\mathbf{p}_1-\mathbf{p}_2-\mathbf{p}_3) \times\delta(\epsilon_c+\tilde{\epsilon}_{p1}-\tilde{\epsilon}_{p2}-\tilde{\epsilon}_{p3})[\delta(\mathbf{p}-\mathbf{p}_1)-\delta(\mathbf{p}-\mathbf{p}_2)-\delta(\mathbf{p}-\mathbf{p}_3)] \times[(1+f_1)f_2f_3 - f_1(1+f_2)(1+f_3)], \quad (7.21)$$

where a condensate atom locally has energy $\epsilon_c(\mathbf{r},t) = \mu_c(\mathbf{r},t) + \frac{1}{2}mv_c^2(\mathbf{r},t)$. Note that condensate atoms can be excited by collision with a thermal atom, and vice-versa. Thus there is an exchange of atoms, which in the absence of local equilibrium between the two components leads to damping. The generalised Gross-Pitaevskii equation then includes a dissipative term:

$$i\hbar\frac{\partial}{\partial t}\Psi(\mathbf{r},t) = \left(-\frac{\hbar^2}{2m}\nabla^2 + V(\mathbf{r},t) + g[2\tilde{n}(\mathbf{r},t)+n_c(\mathbf{r},t)] - i\Lambda(\mathbf{r},t)\right)\Psi(\mathbf{r},t), \quad (7.22)$$

where,

$$\Lambda(\mathbf{r},t) = \frac{\hbar}{2n_c}\int \frac{d\mathbf{p}}{(2\pi\hbar)^3} C_{12}[f]. \quad (7.23)$$

In Refs. [148, 164, 165, 166], moments of the kinetic equation (7.18) were taken to yield hydrodynamical equations [31]. These can be solved explicitly under certain conditions using a variational method [148]. An alternative approach is to solve (7.18) directly. In general, this is very difficult owing to the six-dimensional nature of phase-space. One possibility is to work under the *assumption of sufficient ergodicity*. Ergodicity assumes that the distribution of atoms in phase-space depends only on their energy. Then (7.18) reduces to an equation of motion for $f(\epsilon)$. This assumption is well-known in the literature and has been used to model evaporative cooling [167, 168] and condensate growth [169, 170, 171] in Bose gases.

However, ergodicity assumes that any deformation in momentum or position space is isotropic, or that the ergodic mixing time is shorter than the elastic collision time. In general, non-equilibrium situations (e.g. vortex and collective mode dynamics) this assumption is not valid. In addition, we are primarily interested in the gas dynamics in position space and its coupling to the condensate. Hence, a Monte Carlo technique [172, 173, 174] is more appropriate here. In particular, we utilise a direct simulation Monte Carlo (DSMC) method, as performed to model evaporative cooling in Bose gases [173, 174], and described in detail for classical gas dynamics in [175]. We will discuss our extension of this model to simulate the thermal cloud coupled to the condensate in the next section.

7.3 Monte Carlo simulations

7.3.1 Classical gases and evaporative cooling

The direct simulation Monte Carlo method was first developed by Bird to describe classical gas flows [175]. It is equivalent to solving the Boltzmann equation in phase-space, except that it recognises the discrete nature of the gas on a microscopic level. In principle, the trajectory of each atom could be followed at all times, so that the state of the system is completely described by storing $(\mathbf{r}, \mathbf{v})$ for all atoms. However, the calculation becomes unfeasible in the presence of interparticle collisions. Bird's method makes the key assumption that the free particle motion and collisions are uncoupled over a short time interval, Δt. This provides an accurate description of the gas so long that $\Delta t \ll \tau_{\rm coll}$, where $\tau_{\rm coll}$ is the mean collision time. Hence the DSMC method is most appropriate for describing gases in the Knudsen regime, where the mean free length is much larger than the size of the system. The technique is therefore well suited to dilute alkali gases.

We will first describe the method for the classical case, where the generalisation to quantum gases is discussed in the next subsection. First, the atoms are moved over distances appropriate to their velocity components, $\mathbf{v}_n$, such that $\mathbf{r}_{n+1} = \mathbf{r}_n + \mathbf{v}_n \Delta t$, before collisions are treated. To ensure that collisions only take place between near neighbours, position space is divided into cubic cells of a size much smaller than the dimensions of the cloud. The number of atoms is counted in each cell to furnish the local density $\tilde{n}(\mathbf{r})$. Pairs of atoms in a cell are then chosen at random, and the following algorithm is used to decide whether they collide. First, the mean number of collisions locally in time Δt is calculated using:

$$\bar{\eta}(\mathbf{r}) = \tilde{n}(\mathbf{r}) \sigma v_r F \Delta t, \tag{7.24}$$

where $\sigma = 8\pi a^2$ is the scattering cross-section for bosons in a hard sphere model, and $v_r = |\mathbf{v}_2 - \mathbf{v}_1|$ is the relative velocity of the two atoms. A 'quantum scattering factor', F, is also included, although here $F = 1$ (note that the indistinguishability of the bosons is treated here, but the quantum enhancement of scattering is not). The number of collisions follows a Poisson distribution. As $\bar{\eta}(\mathbf{r}) \ll 1$, then the collision probability is given by:

$$P_{\text{coll}} = 1 - \mathrm{e}^{-\bar{\eta}(\mathbf{r})}. \tag{7.25}$$

A random number, R_0, is compared to P_{coll}. If $R_0 > P_{\text{coll}}$ then nothing happens, and the algorithm moves on to the next pair in the cell. On the other hand, if $R_0 < P_{\text{coll}}$ then a collision takes place. To account for energy and momentum conservation the collision is most conveniently treated in the centre-of-mass frame of the atoms. Two further random numbers, R_1 and R_2, are chosen to determine the scattering angles $\phi = 2\pi R_1$ and $\cos\theta = 1 - 2R_2$, where $R_{1,2} \in [0, 1]$. Note that the collision products are distributed isotropically, corresponding to s-wave scattering. Once this procedure has been repeated for all of the atoms in each cell, the final part of the time-step involves updating the atom velocities to account for gradients in the external potential, $\mathbf{v}_{n+1} = \mathbf{v}_n + \Delta\mathbf{v}_n$, where:

$$\Delta\mathbf{v}_n = -\frac{\partial_n U_{\text{eff}}(\mathbf{r})}{m}\Delta t. \tag{7.26}$$

In this case, $U_{\text{eff}}(\mathbf{r}) = V(\mathbf{r}) = m\omega^2 r^2/2$, while the gradient operator is evaluated computationally using central differencing.

A good test of the classical model described here is to simulate evaporative cooling [173]. Recall that this is an experimental scheme to cool gases down to ultralow temperatures, and has been used to reach the phase-space densities required for quantum degeneracy. We model the RF 'scalpel' by removing ^{87}Rb atoms at position $x^2 + y^2 \geq r_{\text{cut}}^2$, where $r_{\text{cut}}(t) = \mathrm{e}^{-t/\tau_{\text{evap}}}$. This '2D forced evaporation' roughly corresponds to experimental realisations. Our initial condition is a Maxwell-Boltzmann distribution of $N = 10^5$ atoms at $T = 90\,\mu$K in an isotropic harmonic trap with $\omega = 2\pi \times 240\,$Hz. The initial cut is made at $r_{\text{init}} = 300\,\mu$m, and is ramped down over $t = 40\,$s with a time constant $\tau_{\text{evap}} = 30\,$s. The total energy of the gas can be simply calculated using $E_{\text{tot}} = \sum_\alpha E_\alpha$ ($\alpha \in \{x, y, z\}$), where $E_\alpha = (m/2)\sum_n v_{\alpha n}^2 + \omega_\alpha^2 \alpha_n^2$ is summed over all atoms. This yields the effective temperature $T = E_{\text{tot}}/3Nk_B$, as plotted in Fig. 7.4(a). We also define effective temperatures along each dimension $T_\alpha = E_\alpha/Nk_B$ shown in Fig. 7.4(b). Note that T_z tends to lag behind T_x and T_y, reflecting the time required for collisional relaxation. This justifies our suspicion of the ergodic approximation in this situation

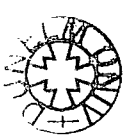

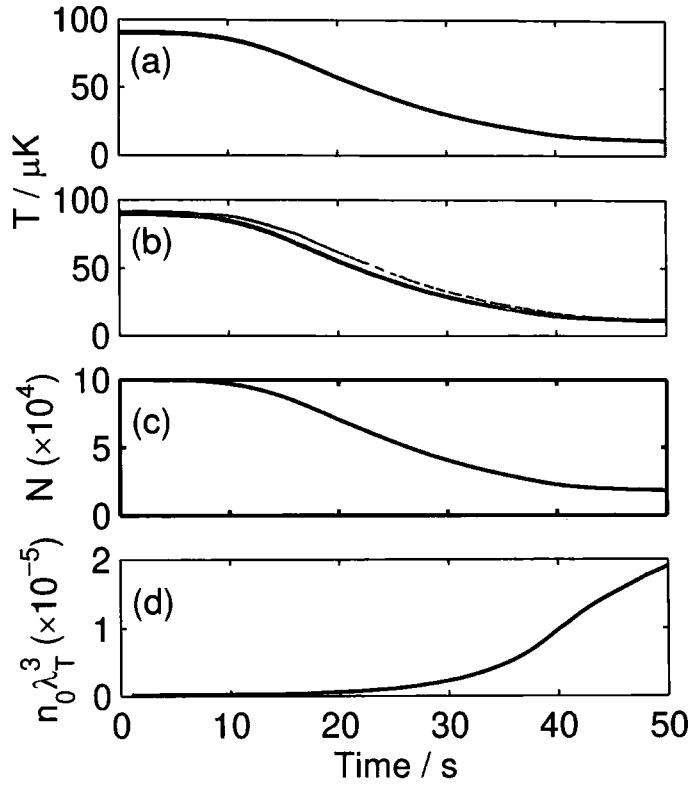

Figure 7.4: Results of a classical Monte Carlo model of evaporative cooling. (a) shows the effective temperature, T, as a function of time, while (b) plots the effective temperature along each dimension: T_x and T_y (solid) and T_z (dashed); (c) gives the number of remaining atoms, while (d) plots the phase-space density. The radius of evaporation is ramped down from $r_{\rm cut} = 300\,\mu$m over $t = 40\,$s with a time constant of $\tau_{\rm ramp} = 30\,$s. For $t > 40\,$s the cut radius remains at $r_{\rm cut} \simeq 79\,\mu$m.

(the same is true of the quadrupolar oscillations treated later in this chapter). Once the forced evaporation ramp has been stopped the three directions re-equilibrate after a few collision times. This relaxation time accounts for the further decrease in temperature after $t = 40\,$s. Over the time-scale of our simulation we find that the number of atoms in the trap [Fig. 7.4(c)] has dropped to $N = 18160$ at a final temperature of $T = 11.3\,\mu$K. The phase-space density $n_0\lambda_T^3$ can be estimated using the peak density of a Maxwell-Boltzmann distribution at equilibrium: $n_0 = N\omega^3(m/2\pi k_B T)^{3/2}$. We find [Fig. 7.4(d)] that the phase-space density increases by two orders of magnitude from 2.1×10^{-7} to 1.9×10^{-5}, compared to a one order of magnitude decrease in the number of atoms. This scaling behaviour is characteristic of evaporative cooling, indicating its utility in creating Bose-Einstein condensates in the laboratory.

7.3.2 Bose gases

We can extend our Monte Carlo method to account for Bose enhancement of scattering. This effect is represented in the collision integral (7.20) by $1 + f_i$ factors, indicating that in a Bose gas the probability of scattering into states that are already occupied is increased (similarly $1 - f_i$ factors are responsible for 'Pauli blocking' in Fermi-degenerate gases). We include this consequence of Bose statistics into our simulations by setting $F = [1+f(\mathbf{p}_3,\mathbf{r},t)][1+f(\mathbf{p}_4,\mathbf{r},t)]$ in (7.24), where $\mathbf{p}_3$ and $\mathbf{p}_4$ are the momenta of the collision products. The distribution function can be estimated by counting the number of atoms within subcells in momentum space, which in turn are subdivisions of the positional cells mentioned in the previous section. Strictly speaking, each phase-space subcell should have a volume of h^3, which is the minimum value allowed by the uncertainty principle. However, the computational time required to sort the atoms increases linearly with the total number of subcells, and can become prohibitively large without some form of coarse graining (which indeed is the definition of f inherent in the Boltzmann equation description). We therefore count the number of atoms $\mathcal{N}_{\rm sc}$ within larger subcells, which is renormalised to yield:

$$f(\mathbf{p},\mathbf{r},t) = \mathcal{N}_{\rm sc}\frac{h^3}{\mathcal{V}_{\rm p}\mathcal{V}_{\rm r}}, \tag{7.27}$$

where $\mathcal{V}_{\rm p}$ and $\mathcal{V}_{\rm r}$ are the volumes of cells in momentum and position space respectively. We find that our results are largely independent of the number of cells and subcells for sufficiently large numbers. For example, for the computations described below we use 8000 cells subdivided into 9261 subcells. Note that to calculate the collision probability (7.25) the momenta of the products must now be known in advance. Thus, the scattering angles for each pair are chosen *a priori* and the collision accepted or rejected on the basis of the collision probability.

We can look at the effect of the Bose enhancement factors by beginning with a Maxwell-Boltzmann distribution at some temperature T, then allowing the gas to relax to a new equilibrium. Our results are shown in Fig. 7.5, where we simulate $N = 10^5$ ^{87}Rb atoms in a spherical harmonic trap of frequency $\omega = 2\pi \times 150\,\mathrm{Hz}$, corresponding to a critical temperature of $T_c^0 = 314\,\mathrm{nK}$. We look at the atomic distribution in position space and energy by plotting histograms, where the energy is expressed in terms of $k_B T$ (note that T now represents an 'effective' temperature associated with the initial classical distribution). For $T \gtrsim 300\,\mathrm{nK}$, the distribution remains classical. However, for $T < 300\,\mathrm{nK}$ a peak appears at low energies and near to the centre of the trap in position space, as would be expected from Bose statistics. A further consequence, as shown in Fig. 7.6, is that the mean collision rate increases

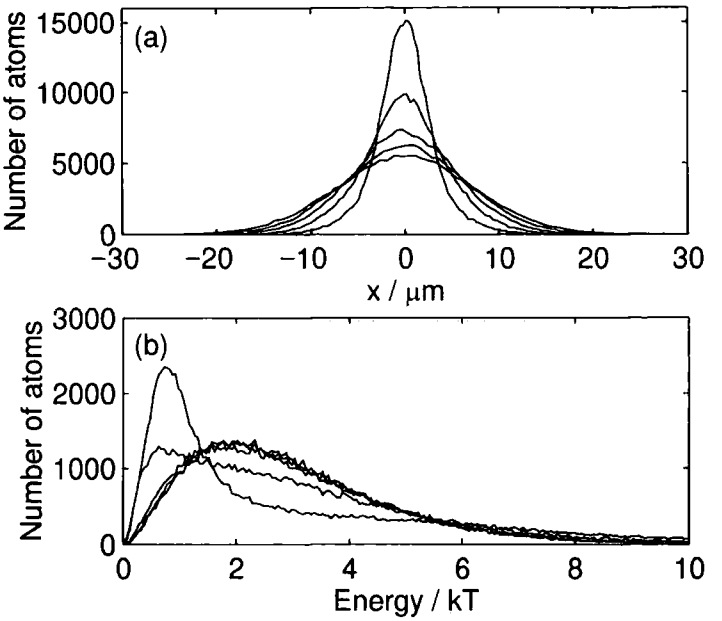

Figure 7.5: The impact of Bose statistics on the equilibrium position and energy distributions, where $N = 10^5$ ^{87}Rb atoms are modelled in a spherical trap. (a) shows a histogram of the number of atoms against x for five effective temperatures: (from top to bottom) $T = 100\,\text{nK}$, $200\,\text{nK}$, $300\,\text{nK}$, $400\,\text{nK}$, and $500\,\text{nK}$. Energy histograms for the same temperatures are plotted in (b), where one sees the characteristic low-energy enhancement of atom number at low temperatures.

with the respect to the classical result $1/\tau_{\text{coll}} = \sqrt{2}\bar{n}\sigma\bar{v}$, where $\bar{v} = \sqrt{8k_bT/\pi m}$ is the mean atomic velocity while $\bar{n} = n_0/\sqrt{8}$. This effect is due to the enhanced density in low momentum regions of the gas, and contributions from higher order terms in the collision integral [172].

7.3.3 Coupled Monte Carlo and GP simulations

Given that we can model the thermal atoms, we are now in a position to couple our Monte Carlo simulations to the Gross-Pitaevskii equation for the condensate. As a first approximation we will consider here only mean-field coupling between the components, while neglecting collisions which remove atoms from the condensate (i.e. $C_{12} = 0$ and $C_{22} \neq 0$). The simulations then become a matter of performing alternating Monte Carlo and GP propagation steps during each time-step, Δt, where the condensate propagates in a potential $V(\mathbf{r},t)+g[2\tilde{n}(\mathbf{r},t)+n_c(\mathbf{r},t)]$, while thermal atoms move in an effective potential:

$$U_{\text{eff}}(\mathbf{r},t) = V(\mathbf{r},t) + 2n(\mathbf{r},t). \tag{7.28}$$

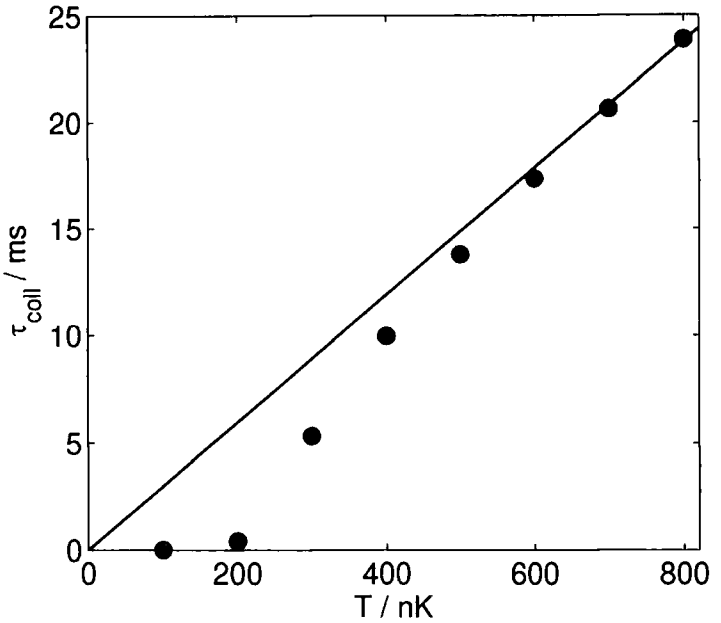

Figure 7.6: Effect of Bose statistics on the mean collision time, $\tau_{\rm coll}$, for the same parameters as Fig. 7.5. From the measured data (bullets) one sees a sharp decrease in the collision time at low temperatures, while at higher temperatures the data tends towards the classical result $\tau_{\rm coll} = 1/(\sqrt{2}\tilde{n}\sigma\bar{v})$

The thermal gas density is calculated at each point by counting atoms in each cell. The cells do not necessarily correspond to the GP grid, so cubic spline interpolation is used to smooth $\tilde{n}$. This is to avoid discontinuities in the mean-field potential, that may lead to instabilities in the FFT method used to propagate the condensate wavefunction.

The first stage of the simulation is to find the initial state for a prescribed temperature, T. The numbers of condensate and thermal atoms are found by the semi-classical algorithm described in Sec. 7.2.2. The equilibrium condensate density evaluated by this method, as well as a Maxwell-Boltzmann distribution for the thermal atoms, are used as an initial state for the MC-GP algorithm. The condensate is propagated through imaginary time while the thermal cloud relaxes to equilibrium. A time dependent trap potential $V(\mathbf{r}, t)$ is then applied and the system allowed to propagate in real time. This allows simulations of many different dynamical scenarios. An application to modelling quadrupole collective excitations is discussed in the next section.

7.4 Damping of collective excitations

Amongst the most compelling evidence for the validity of the GP equation for low temperatures is its quantitative agreement with experiment for the low-energy collective modes. However, consistent theoretical descriptions at higher temperatures have proved much more elusive, where experiments have demonstrated marked frequency shifts and damping of the condensate modes in the presence of a significant non-condensed component [109, 158]. Studies have tended to concentrate on one of two regimes, depending upon the density and temperature of the system. At high densities, where collisions are sufficiently rapid to force the system into local equilibrium, the system can be described by a set of coupled hydrodynamical equations [148, 164, 165, 166]. Damping mechanisms in this case are of a dissipative type (i.e. viscosity and thermal relaxation). For very dilute systems at low temperatures the mean free path of the elementary excitations become comparable to the size of the system and collisions play only a minor role. Damping in this regime is not related to thermalisation processes but to coupling between excitations, and can be described within the framework of mean-field theories (see [108] and references therein). The collisionless regime may be appropriate for the JILA experiments [5, 109] while the MIT experiments lie between the collisionless and hydrodynamical regimes [4, 158]. One of the advantages of our model is that we can study this intermediate region.

We simulate collective excitations using 40000 atoms in a disk-shaped trap ($\omega_x = \omega_y = 2\pi \times 131\,\mathrm{Hz}$, $\omega_z = \sqrt{8}\omega_x$). These are similar parameters to the JILA experiment [109]. We first find our initial condition for a given temperature using the method described in the previous section. A quadrupole mode is then excited using a sudden change in the trap parameters at $t = 0$.[1] We study the $m = 0$ mode, which is excited by a 10% increase in the radial frequencies, ω_x and ω_y. The subsequent condensate oscillations are shown in Fig. 7.7. We clearly observe damping at higher temperatures, which is absent at $T = 20\,\mathrm{nK}$. Note that we determine the widths of both the components by calculating the standard deviation $\sigma_x = \sqrt{\langle x^2\rangle - \langle x\rangle^2}$, where we use $\langle x^n\rangle = \int \mathrm{d}^3\mathbf{r}\, x^n |\Psi|^2$ for the condensate and $\langle x^n\rangle = \sum_i x_i^n/N$ for the thermal cloud. To avoid large statistical fluctuations in the normal cloud, especially at low temperatures, we simulate ten times the physical number of atoms (equivalent to repeatedly running our simulations: a time-consuming process). For consistency the density and phase-space density of the gas are rescaled appropriately.

[1] A 'softer' drive is also imposed by varying the trap frequencies over several oscillations. We find that our results are largely independent of the form of the excitation, apart from a slight dependence on the oscillation amplitude for large values.

We use a least squares method to fit the condensate widths along x and y to an exponentially decaying sine function:

$$\sigma_i(t) = A\mathrm{e}^{-\Gamma t}\cos\omega t + B. \tag{7.29}$$

The condensate decay rate, Γ, and frequency, ω, are plotted against temperature in Fig. 7.8. The damping increases from zero at low temperatures, before tending towards a linear dependence at intermediate values ($T < 0.7T_c^0$). This is in agreement with the expected behaviour of Landau damping in homogeneous and trapped condensates, where in the limit of zero temperature the damping has a $\Gamma \sim T^4$ dependence, while at higher temperatures $\Gamma \sim T$ [105, 107, 108, 177]. We also observe quantitative agreement with previous theory [107, 177, 178] and experiment in this regime. For example, at $T = 200\,\mathrm{nK}$ ($T/T_c^0 \simeq 0.7$) we find that $\Gamma \simeq 45.3\,\mathrm{s}^{-1}$, in fair agreement with the experimental value of $90 \pm 40\,\mathrm{s}^{-1}$ [109]. We note that Landau damping is a purely mean-field effect. This is evident in a particularly transparent treatment by Giorgini [108] who showed that Landau damping is due to mean-field coupling between fluctuations in the condensate wavefunction, $\delta\Psi$, and in the non-condensate density, $\delta\tilde{n}$. Physically this is equivalent to absorption of a quantum of the collective mode by a thermal excitation (4.4). Note that we find no damping at low temperatures, implying that Balieav damping is not observed. This mechanism involves the decay of the collective mode into two lower frequency excitations, and occurs even at zero temperature. It is equivalent to coupling between $\delta\Psi$ and fluctuations in the anomalous density, $\delta\tilde{m}$ [108], which are neglected in our model. However, this decay mechanism is expected to be suppressed in trapped condensates due to the discrete nature of the levels at low energy.

We observe a dip of the damping rate in the region $0.7T_c^0 < T < 0.8T_c^0$. This is related to an interesting 'beating' effect in the condensate oscillation. In this temperature range the oscillations are seen to damp rapidly at early times, before reviving at a smaller amplitude after approximately ten oscillations. As a result, the fitting function (7.29) tends to under-estimate the damping rate. As shown in Fig. 7.9, the condensed and normal components oscillate at slightly different frequencies due to their weak coupling, and the condensate is much more highly damped than the thermal gas. The latter is a consequence of the more massive thermal cloud at this temperature (so that the back-action from Landau damping has less of an impact) and the small 'internal' damping of the cloud from thermalisation processes. As a result the thermal cloud acts as a kind of energy reservoir. When the oscillations of the two components are in anti-phase the condensate oscillations are strongly damped; however, when they are in phase the thermal cloud tends to

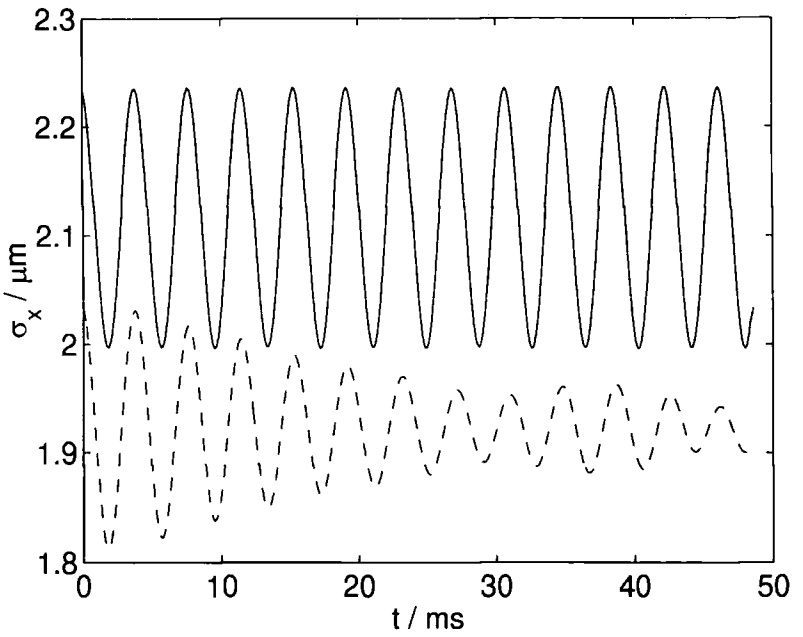

Figure 7.7: Quadrupole ($l = 2$, $m = 0$) oscillations of a condensate at $T = 20\,\mathrm{nK}$ (solid) and $T = 160\,\mathrm{nK}$ (dashed). The width of the condensate is represented by the standard deviation along x, σ_x. Damping is observed at higher temperatures due to coupling with the non-condensed thermal cloud.

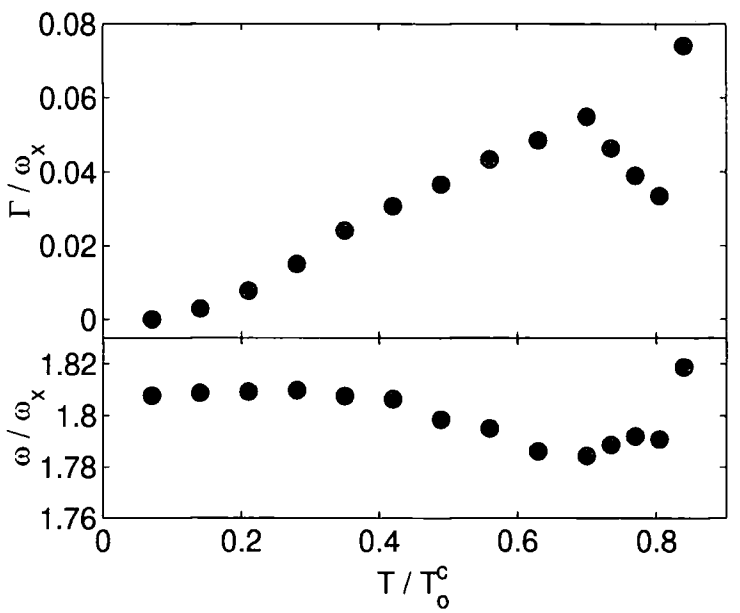

Figure 7.8: The damping rate, Γ (top) and frequency ω (bottom) of quadrupole $m = 0$ oscillations in a cloud of 40000 atoms. The x-axis is plotted as function of temperature, T/T_c^0, where $T_c^0 = 286\,\mathrm{nK}$ is the ideal critical temperature, while the y-axes are plotted with respect to the trap frequency $\omega_x = 2\pi \times 131\,\mathrm{Hz}$.

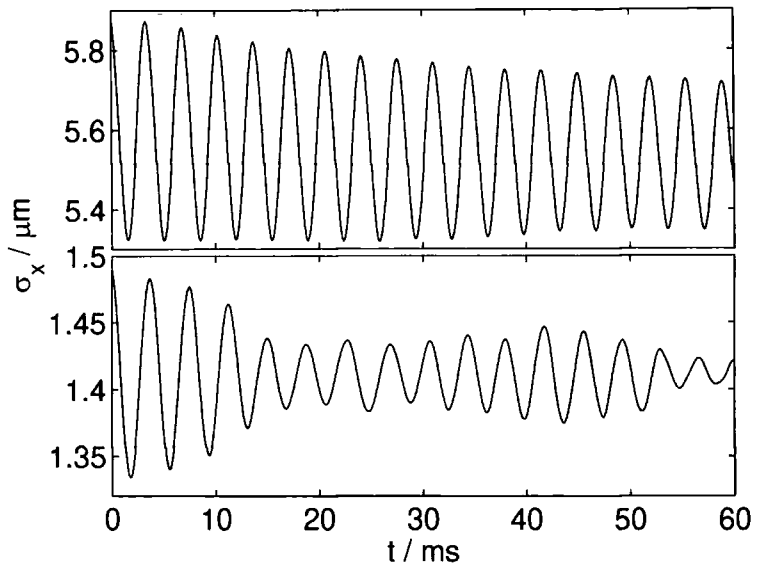

Figure 7.9: Quadrupolar oscillations in the thermal cloud (top) and condensate (bottom) at $T = 240\,\mathrm{nK}$. A revival of the condensate oscillations occurs at $t \simeq 40\,\mathrm{ms}$.

drive the condensate oscillations. This beating effect is most noticeable when one component is significantly larger than the other. Correspondingly, we see the same effect in the thermal cloud at low temperatures, though this is not evident in Fig. 7.8.

The condensate oscillation frequencies are also plotted in Fig. 7.8. The figure shows a small downward shift in frequency for $T < 0.6T_c^0$ [109, 178]. An increase in frequency above $0.6T_c^0$ is also observed; however, this is not as large as that seen in the JILA experiment [109], where the frequency approaches $2\omega_x$ in this region. A possible explanation for this behaviour was provided by Bijlsma and Stoof [163], who suggested a cross-over between normal modes where the two components oscillate in phase and anti-phase. However, as noted previously we find that the components oscillate at slightly different frequencies, and this description is inappropriate here. We may be able to see this effect at higher temperatures, though unfortunately the condensate in this regime is small and more sensitive to local fluctuations in the thermal cloud density, leading to unacceptable errors. The experimental data also suffers from large errors in this region, making a direct comparison difficult.

To summarise, in this section we have studied frequency shifts and Landau damping due to mean-field coupling between the condensate and the thermal cloud. This should not be confused with the C_{12} damping mechanism discussed in Sec. 7.2.3, which is due to collisions between thermal and condensate atoms. For exam-

ple, Landau damping is a three excitation process as opposed to the four excitations involved in collisional damping. Our approach is justified as a first approximation because for our parameters the magnitude of collisional damping is significantly smaller than Landau damping [176]. The next step would be the inclusion of the C_{12} collisions in our Monte Carlo simulations. In addition to an accurate modelling of collective excitations, this could also be used to study condensate formation in systems far from equilibrium. Another application of the model would be to study vortex dynamics at finite temperatures. A vortex in this case would be an 'obstacle' in the mean-field experienced by non-condensed particles, leading to scattering and hence a net force on the vortex. This should result in a drift of the vortex to the condensate edge, as expected, and allow direct determinations of vortex lifetimes. Similar models could also facilitate a fully consistent description of the dissipative processes discussed in Chapter 6.

Chapter 8

Conclusion

In this thesis we have studied the theory of Bose-Einstein condensation in trapped alkali gases. We have particularly focused on the dynamics of Bose condensates, mainly in the limit of very low temperatures where the evolution of the condensate wavefunction can be described by a nonlinear Schrödinger equation, or Gross-Pitaevskii equation. The nonlinear nature of this equation allows a rich tapestry of behaviour, including the existence of topological defects such as solitons and quantised vortices. Most of this thesis has concentrated on the properties of vortices. We have demonstrated that vortices can be nucleated by local disturbances within the condensate, produced, for example, by moving obstacles through the fluid. We suggest that in experiments obstacles could be produced by focused far-detuned laser beams or by tightly confined condensates of a different species. We have also related vortex formation to drag and energy dissipation, and shown that these effects arise only above a critical velocity. Recent experiments on critical velocities in Bose-condensed gases [45, 70, 134] have begun to address these questions, and provide evidence of the link between dissipation and vortices. However, many interesting problems remain for the future, especially in relation to a fundamental understanding of the vortex formation process, and evaluation of the critical velocity for penetrable objects in spatially inhomogeneous condensates.

The experimental creation and observation of vortex states in Bose-Einstein condensates defined an important landmark in the development of the field [43, 72]. Much of the future work will concentrate on the dynamics and stability of vortex lines, which have been connected together by previous studies. In this thesis we have studied vortex dynamics using numerical simulations, and explained the motion using an intuitive physical picture involving the Magnus effect. We have also demonstrated that the link between vortex line precession and decay is also true of more complex configurations such as vortex rings.

The existence of quantised vortices is intimately related to the phenomenon of superfluidity. Generally speaking, vortices in homogeneous quantum fluids are stable, so that the fluid circulation demonstrates the superfluid property of persistent currents. The response of the condensate to an external probe is also a fundamental manifestation of superfluidity. No dissipation is evident at low flow speeds, but arises above a critical velocity due to vortex formation. One may hope that the observation of these effects in trapped gases, as well as other consequences of superfluidity, may shed light on other systems such as liquid helium as well as being interesting in their own right. However, care must be taken as previous definitions of superfluidity have usually dealt with large systems rather than inhomogeneous trapped gases with relatively small numbers of atoms. One may imagine that future experiments will facilitate studies of much larger condensates; nevertheless in the meantime we must contend with finite vortex lifetimes (albeit long ones) and the need to oscillate objects due to the small length-scale of the condensate, producing excitations even at very low velocities. More general definitions are needed in order to include trapped condensates. In effect, this extension is similar to that required for the phenomena of ODLRO and phase coherence in finite condensates.

As well as the low temperature case, we have also studied the dynamics at higher temperatures where the non-condensed component is no longer negligible. We simulate the non-condensed cloud using a direct Monte Carlo method, which is coupled *via* mean-fields to the condensate (described by a generalised Gross-Pitaevskii equation). In common with other finite temperature studies, we simulate quadrupole oscillations in the system, and measure damping rates and frequency shifts as a function of temperature. So far most finite temperature theories have attempted to explain these effects in collective modes, which reflects the relative simplicity of the system as well as the availability of experimental data for comparative purposes. The focus of future work will be to model more complex systems, such as vortex states. One would expect that finite temperature condensate dynamics will be even more rich than its low temperature counterpart. The challenge is to describe the new physics in terms of existing fundamental theories. The flexibility of our approach in modelling the system under a wide range of conditions makes it ideally placed to meet this challenge.

As discussed in the Introduction, Bose-Einstein condensation is of great importance in a wide range of phenomena. To understand BEC is to understand a major part of physics. Conversely, many specialised topics must be combined when studying BEC. We have touched on some of these in this thesis: statistical mechanics, quantum mechanics and quantum field theory, atomic physics and atom optics, fluid

mechanics, and condensed matter physics. However, the frenzy of experimental and theoretical work over the last five years has established the study of BEC in trapped gases as a subject in its own right, and one that is certain to fascinate researchers for a long time to come.

Appendix

Numerical methods

In this appendix we describe some of the numerical methods that can be employed to solve the nonlinear Schrödinger equation in time dependent and time independent cases. The split-step Fast Fourier Transform (FFT) and Crank-Nicholson methods both make unitary numerical approximations to the evolution operator, facilitating numerical propagation of the wavefunction. They can also be readily applied to finding stationary solutions of the time independent equation using imaginary time. We also describe how the FFT method can be extended to cylindrical and spherical coordinates, and to include an angular momentum operator in a rotating frame.

A.1 Split-step FFT method

We begin our discussion at Eq. (2.23) for the evolution of the wavefunction over a short time-step Δt. By expansion one can readily prove that:

$$e^{-iH_I\Delta t} = e^{-iV\Delta t}e^{-iT\Delta t} + \mathcal{O}(\Delta t^2), \tag{A.1}$$

$$e^{-iH_I\Delta t} = e^{-iV\Delta t/2}e^{-iT\Delta t}e^{-iV\Delta t/2} + \mathcal{O}(\Delta t^3), \tag{A.2}$$

where V and T are the potential and kinetic parts of the Hamiltonian. The expressions (A.1) and (A.2) correspond to full-step and half-step expansions respectively, where the errors in Δt are due to the non-commutability of the V and T operators. We use the half-step scheme throughout this thesis. The potential operators (including the trap and interaction potentials) are relatively easy to apply, simply corresponding to the phase shifts of the wavefunction. The kinetic step, in contrast, involves expansion on a Fourier basis.

The numerical procedure begins with discretisation on a spatial grid of N points with spacing Δx in the interval $[-A, A)$ (for illustrative purposes we consider only 1D at this stage). The wavefunction at each point is then multiplied by the first

potential half-step, i.e. $f_j(t) = \mathrm{e}^{-iV(j\Delta x - A,t)\Delta t/2}\Psi_j(t)$. The function is transformed to momentum space using a Fast Fourier Transform (FFT) routine [179]:

$$\tilde{f}_k(t) = \frac{1}{\sqrt{N}} \sum_{j=0}^{N-1} f_j \mathrm{e}^{-2\pi ijk/N}; \qquad k = -\frac{N}{2}, \ldots, 0, \ldots, \frac{N}{2} - 1. \tag{A.3}$$

The function is then multiplied by a phase factor corresponding to free particle propagation in momentum space: $\tilde{f}_k(t + \Delta t) = \mathrm{e}^{i\pi^2 k^2 \Delta t/A^2}\tilde{f}_k$. We inverse FFT back to position space:

$$f_j(t + \Delta t) = \frac{1}{\sqrt{N}} \sum_{k=-N/2}^{N/2-1} \tilde{f}_k(t + \Delta t)\mathrm{e}^{2\pi ijk/N}. \tag{A.4}$$

Finally, the function is multiplied by the second potential half-step: $\Psi_j(t + \Delta t) = \mathrm{e}^{-iV(j\Delta x - A,t)\Delta t/2} f_j(t + \Delta t)$. The extension to multiple dimensions is straightforward using the appropriate FFT routines. We find that the FFT method is very efficient for these multi-dimensional problems. However, the method is not appropriate for modelling hard-edged potential (e.g. an impenetrable obstacle) due to the creation of high energy excitations in Fourier space. Excitations can also arise for high C as a result of mode mixing, leading to instabilities in the wavefunction that can become significant over long propagation times. We find that coarser grids (i.e. larger Δx) and smaller time-steps help to combat these instabilities. The simulations discussed in this thesis typically use time-steps of around $\Delta t = 10^{-3}$.

A.2 Crank-Nicholson method

An alternative route to the split-step operator technique is to use finite differences. To represent the evolution operator, *Cayley's form* is used:

$$\mathrm{e}^{-iH_I\Delta t} = \frac{1 - iH_I\Delta t/2}{1 + iH_I\Delta t/2} + \mathcal{O}(\Delta t^3), \tag{A.5}$$

which is unconditionally stable and unitary. Discretising the wavefunction in 1D space as well as time ($x = j\Delta_x - A$, $t = n\Delta t$) gives:

$$\left(1 + \frac{1}{2}iH_I^{n+1}\Delta t\right)\Psi_j^{n+1} = \left(1 - \frac{1}{2}iH_I^n\Delta t\right)\Psi_j^n. \tag{A.6}$$

The Hamiltonian can now be represented using finite differences:

$$\begin{aligned}\Psi_j^{n+1} - \frac{i\Delta t}{2(\Delta x)^2}\left(\Psi_{j+1}^{n+1} - 2\Psi_j^{n+1} + \Psi_{j-1}^{n+1}\right) + \frac{i\Delta t}{2}U_j^{n+1}\Psi_j^{n+1} \\ = \Psi_j^n + \frac{i\Delta t}{2(\Delta x)^2}\left(\Psi_{j+1}^n - 2\Psi_j^n + \Psi_{j-1}^n\right) - \frac{i\Delta t}{2}U_j^n\Psi_j^n,\end{aligned} \tag{A.7}$$

where $U_j^n = V_j^n + C|\Psi_j^n|^2$. We see immediately that this may be represented by the matrix equation $\mathbf{A} \cdot \boldsymbol{\Psi}^{n+1} = \mathbf{B} \cdot \boldsymbol{\Psi}^n$, where $\boldsymbol{\Psi}^n$ is the column vector $(\Psi_1^n, \Psi_2^n, \ldots)$, and $\mathbf{A}$ and $\mathbf{B}$ are the tridiagonal matrices:

$$\mathbf{A} = \begin{pmatrix} 1+\lambda+\chi U_j^{n+1} & -\lambda/2 & 0 & \cdots \\ -\lambda/2 & \ddots & \ddots & \\ 0 & \ddots & \ddots & \ddots \\ \vdots & & \ddots & \ddots \end{pmatrix}, \tag{A.8}$$

$$\mathbf{B} = \begin{pmatrix} 1-\lambda-\chi U_j^{n} & \lambda/2 & 0 & \cdots \\ \lambda/2 & \ddots & \ddots & \\ 0 & \ddots & \ddots & \ddots \\ \vdots & & \ddots & \ddots \end{pmatrix}, \tag{A.9}$$

where $\lambda = i\Delta t/(\Delta x)^2$ and $\chi = i\Delta t/2$. The problem then reduces to matrix inversion of $\mathbf{A}$, which can readily performed using standard methods [179]. Note that evaluation of U_j^{n+1} requires knowledge of the wavefunction at time $t + \Delta t$. For time dependent simulations an iterative procedure is required, where for each time-step the above process is repeated until the wavefunction converges to an appropriate tolerance level.

For multiple dimensions, alternating direction implicit (ADI) methods are used. These are discussed in more detail in e.g. [179]. However, the basic idea involves splitting the Hamiltonian into operators that difference in each direction. For example, in 2D we can write $H_I = H_x + H_y$, so to first order:

$$\left(1 + \frac{i\Delta t}{2} H_I\right) \simeq \left(1 + \frac{i\Delta t}{2} H_x\right)\left(1 + \frac{i\Delta t}{2} H_y\right). \tag{A.10}$$

The problem now consists of solving the 1D matrix equation in the x-direction for each fixed y, then solving in y to find Ψ_{jk}^{n+1}.

Both the FFT and Crank-Nicholson methods can be extended to finding stationary solutions of the GP equation using imaginary time propagation, where one simply substitutes $\Delta t \to -i\Delta\tilde{t}$ in the above equations. This basically corresponds to artificially changing the conservative system to one that is purely dissipative, so that the initial condition relaxes after some time to the ground state (minimum energy) solution.

A.3 Cylindrical and spherical coordinates

The FFT method discussed in Sec. A.1 is valid for Cartesian coordinate space, where the computational time grows rapidly with the number of dimensions. It is

therefore desirable to exploit any symmetries in the problem to effectively reduce the number of dimensions. For example, in cylindrical symmetric simulations one can use polar coordinates $r = \sqrt{x^2 + y^2}$, z. The Hamiltonian operator in a trap, $\epsilon = \omega_z^2/\omega_x^2$, then becomes:

$$H_I = \underbrace{-\frac{1}{r}\frac{\partial \Psi}{\partial r}}_{H_1} \underbrace{-\frac{\partial^2 \Psi}{\partial r^2} - \frac{\partial^2 \Psi}{\partial z^2} + \frac{1}{4}(r^2 + \epsilon z^2) + C|\Psi(r,z)|^2}_{H_2}. \tag{A.11}$$

We use a split-step technique, i.e.:

$$\Psi(r, z, t + \Delta t) \simeq \mathrm{e}^{-iH_1 \Delta t}\{\mathrm{e}^{-iH_2 \Delta t}\Psi(r, z, t)\}, \tag{A.12}$$

where H_2 is treated simply using the FFT method described in Sec. A.1, while H_1 is approximated with finite differences ($r = j\Delta r$):

$$-\frac{1}{r}\frac{\partial \Psi}{\partial r} \simeq \begin{cases} -2\left(\frac{\Psi_1 - \Psi_0}{(\Delta r)^2}\right) & r = 0, \\ -\left(\frac{\Psi_{j+1} - \Psi_{j-1}}{2j(\Delta r)^2}\right) & r \neq 0. \end{cases} \tag{A.13}$$

The second expression is simply the central differencing approximation, which however diverges at $r = 0$. For this case we use the relation for an even function: $(1/r)\partial_r f|_{r=0} = f''(0)$ (which can proven simply using a Maclauren series expansion in δr and taking the limit $\delta r \to 0$). Using $\Psi(\Delta r) = \Psi(-\Delta r)$ then yields the first equation in (A.13). The spherically symmetric case, $\nabla^2 = (2/r)\partial_r + \partial_{rr}$, can be treated in exactly the same way. We find good agreement between polar and 3D Cartesian coordinates for both time dependent and time independent calculations. As an example, we evaluated the stationary state for a $C = 500$ spherical condensate using imaginary time. In cylindrical coordinates we found that $\mu = 4.529628$ (where $\Delta t = 10^{-3}$, $\Delta r = 0.0390625$, and $\Delta z = 0.15625$), while in full 3D we found $\mu = 4.529618$. Note that small Δr is required, as the approximations (A.13) are accurate only to first order.

A.4 Rotating frame

To consider the condensate in a frame rotating around the z-axis requires an additional term in the Hamiltonian $-\Omega L_z$, where L_z is the angular momentum operator [see Eq. (5.7)]. In a similar manner to the polar coordinate case (above) we split the Hamiltonian, where H_2 is dealt with using FFT while H_1 is approximated by:

$$H_1 = i\Omega[k\Delta y \delta_x - j\Delta x \delta_y]. \tag{A.14}$$

Central differencing in x and y are represented here by δ_x and δ_y, where $\delta_x = (\Psi_{j+1,k} - \Psi_{j-1,k})/2\Delta x$. Cayley's form is then used to propagate over a partial time-step Δt, with $(1 + iH_1\Delta t/2)$ given by:

$$1 - \frac{\Omega\Delta t}{2}(k\Delta y\delta_x - j\Delta x\delta_y) \simeq \left[1 + \frac{j\Delta x\Delta t\Omega\partial_y}{2}\right]\left[1 - \frac{k\Delta y\Delta t\Omega\partial_x}{2}\right]. \qquad \text{(A.15)}$$

The problem is therefore solved using a two dimensional ADI procedure.

Bibliography

[1] M. H. Anderson, J. R. Ensher, M. R. Matthews, C. E. Wieman, and E. A. Cornell, "Observation of Bose-Einstein condensation in a dilute atomic vapor," Science **269**, 198 (1995).

[2] K. B. Davis, M. -O. Mewes, M. R. Andrews, N. J. van Druten, D. S. Durfee, D. M. Kurn, and W. Ketterle, "Bose-Einstein condensation of a gas of sodium atoms," Phys. Rev. Lett. **75**, 3969 (1995).

[3] C. C. Bradley, C. A. Sackett, J J. Tollett, and R. G. Hulet, "Evidence of Bose-Einstein condensation in an atomic gas with attractive interactions," Phys. Rev. Lett. **75**, 1687 (1995).

[4] W. Ketterle, D. S. Durfee, and D. M. Stamper-Kurn, in *Proceedings of the International School of Physics "Enrico Fermi" Course CXL*, edited by M. Inguscio, S. Stringari, and C. Wieman (IOS Press, Amsterdam, 1999).

[5] E. A. Cornell, J. R. Ensher, and C. E. Wieman, *ibid.*

[6] See e.g. http://amo.phy.gasou.edu:80/bec.html/popular.html.

[7] F. Dalfovo, S. Giorgini, L. P. Pitaevskii, and S. Stringari, "Theory of Bose-Einstein condensation in trapped gases," Rev. Mod. Phys. **71**, 463 (1999).

[8] C. S. Adams and E. Riis, "Laser cooling and trapping of neutral atoms," Prog. Quantum Elect. **21**, 1 (1997).

[9] D. Kleppner, T. J. Greytak, T. C. Killian, D. G. Fried, L. Willmann, D. Landhuis, and S. C. Moss, in [4]

[10] D. G. Fried, T. C. Killian, L. Willmann, D. Landhuis, S. C. Moss, D. Kleppner, and T. J. Greytak, "Bose-Einstein condensation of atomic hydrogen," Phys. Rev. Lett. **81**, 3811 (1998).

[11] H. F. Hess, "Evaporative cooling of magnetically trapped and compressed spin-polarised hydrogen," Phys. Rev. B **34**, 3476 (1986).

[12] W. Ketterle and N. J. van Druten in *Advances in Atomic, Molecular, and Optical Physics*, edited by B. Bederson and H. Walther (Academic Press, San Diego, 1996), No. 37, p181.

[13] A. Griffin in [4].

[14] P. Kapitza, "Viscosity of liquid helium below the λ-point," Nature **141**, 74 (1938).

[15] J. F. Allen and A. D. Misener, "Flow of liquid helium II," Nature **141**, 75 (1938).

[16] F. London, "The λ-phenomenon of liquid helium and the Bose-Einstein degeneracy," Nature **141**, 643 (1938).

[17] S. N. Bose, "Plancks Gesetz und Lichtquanten-Hypothese," Z. Phys **26**, 178 (1924).

[18] A. Einstein, "Quantentheorie des Einatomigen Idealen Gases," Sitzber. Kgl. Preuss. Akad. Wiss. (1925), p.3.

[19] L. Tisza, "Transport phenomena in helium II," Nature **141**, 913 (1938).

[20] L. Landau, "The theory of superfluidity of helium II," J. Phys. (USSR) **5**, 71 (1941).

[21] D. V. Osborne, "The rotation of liquid helium II," Proc. Phys. Soc. A **63**, 909 (1950).

[22] R. J. Donnelly, *Quantized Vortices in Helium II* (Cambridge University Press, Cambridge, 1991).

[23] R. P. Feynman in *Progress in Low Temperature Physics, vol. 1* (North-Holland, Amsterdam, 1955).

[24] S. V. Iordanskii, "Mutual friction force in a rotating Bose gas," Zh. Éksp. Teor. Fiz. **49**, 225 (1965) [Sov. Phys. JETP **22**, 160 (1966)].

[25] I. M. Khalatnikov, *Introduction to the Theory of Superfluidity* (Addison-Wesley, Redwood City, 1989).

[26] D. R. Tilley and J. Tilley, *Superfluidity and Superconductivity, 3rd Edition* (IOP, Bristol, 1990).

[27] A. L .Fetter and J. D. Walecka, *Quantum Theory of Many-Particle Systems* (McGraw-Hill, San Francisco, 1971).

[28] E. P. Gross, "Unified theory of interacting bosons," Phys. Rev. **106**, 161 (1957).

[29] V. L. Ginzburg and L. P. Pitaevskii, "On the theory of superfluidity," Zh. Éksp. Teor. Fiz. **34**, 1240 (1958) [Sov. Phys. JETP **7**, 858 (1958)].

[30] A. Griffin, D. W. Snoke, and S. Stringari (editors), *Bose-Einstein Condensation* (Cambridge University Press, Cambridge, 1995).

[31] K. Huang, *Statistical Mechanics, 2nd Edition* (Wiley, New York, 1987).

[32] T. W. B. Kibble, "Topology of cosmic domains and strings ," J. Phys. A: Math. Gen. **9**, 1387 (1976).

[33] W. H. Zurek, "Cosmological experiments in condensed matter systems," Phys. Rep. **276**, 177 (1996).

[34] J. R. Anglin and W. H. Zurek, "Vortices in the wake of rapid Bose-Einstein condensation," Phys. Rev. Lett. **83**, 1707 (1999).

[35] D. M. Stamper-Kurn, M. R. Andrews, A. P. Chikkatur, S. Inouye, H. -J. Miesner, J. Stenger, and W. Ketterle, "Optical confinement of a Bose-Einstein condensate," Phys. Rev. Lett **80**, 2027 (1998).

[36] M. R. Andrews, C. G. Townsend, H. -J. Miesner, D. S. Durfee, D. M. Kurn, and W. Ketterle, "Observation of interference between two Bose condensates," Science **275**, 637 (1997).

[37] M. -O. Mewes, M. R. Andrews, D. M. Kurn, D. S. Durfee, C. G. Townsend, and W. Ketterle, "Output coupler for Bose-Einstein condensed atoms," Phys. Rev. Lett. **78**, 582 (1997).

[38] I. Bloch, T. W. Hänsch, and T. Esslinger, "Atom laser with a cw output coupler," Phys. Rev. Lett. **82**, 3008 (1999).

[39] E. W. Hagley, L. Deng, M. Kozuma, J. Wen, K. Helmerson, S. L. Rolston, and W. D. Phillips, "A well-collimated quasi-continuous atom laser," Science **283**, 1706 (1999).

[40] C. J. Myatt, E. A. Burt, R. W. Ghrist, E. A. Cornell, and C. E. Wieman, "Production of two overlapping Bose-Einstein condensates by sympathetic cooling," Phys. Rev. Lett. **78**, 586 (1997).

[41] M. R. Matthews, D. S. Hall, D. S. Jin, J. R. Ensher, C. E. Wieman, E. A. Cornell, F. Dalfovo, C. Minniti, and S. Stringari, "Dynamical response of a Bose-Einstein condensate to a discontinuous change in internal state," Phys. Rev. Lett. **81**, 243 (1998).

[42] D. S. Hall, M. R. Matthews, J. R. Ensher, C. E. Wieman, and E. A. Cornell, "The dynamics of component separation in a binary mixture of Bose-Einstein condensates," Phys. Rev. Lett. **81**, 1539 (1998).

[43] M. R. Matthews, B. P. Anderson, P. C. Haljan, D. S. Hall, C. E. Wieman, and E. A. Cornell, "Vortices in a Bose-Einstein condensate," Phys. Rev. Lett. **83**, 2498 (1999).

[44] J. E. Williams and M. J. Holland, "Preparing topological states of a Bose-Einstein condensate," Nature **401**, 568 (1999).

[45] C. Raman, M Köhl, R. Onofrio, D. S. Durfee, C. E. Kuklewicz, Z. Hadzibabic, and W. Ketterle, "Evidence of a critical velocity in a Bose-Einstein condensed gas," Phys. Rev. Lett. **83**, 2502 (1999).

[46] M. J. Holland, D. S. Jin, M. L. Chiofalo, and J. Cooper, "Emergence of interaction effects in Bose-Einstein condensates," Phys. Rev. Lett. **78**, 3801 (1997).

[47] D. S. Jin, J. R. Ensher, M. R. Matthews, C. E. Wieman, and E. A. Cornell, "Collective excitations of a Bose-Einstein condensate in a dilute gas," Phys. Rev. Lett. **77**, 420 (1996).

[48] M. -O. Mewes, M. R. Andrews, N. J. van Druten, D. M. Kurn, D. S. Durfee, C. G. Townsend, and W. Ketterle, "Collective excitations of a Bose-Einstein condensate in a magnetic trap," Phys. Rev. Lett. **77**, 988 (1996).

[49] M. Edwards, P. A. Ruprecht, K. Burnett, R. J. Dodd, and C. W. Clark, "Collective excitations of atomic Bose-Einstein condensates," Phys. Rev. Lett. **77**, 1671 (1996).

[50] S. Stringari, "Collective excitations of a trapped Bose-condensed gas," Phys. Rev. Lett. **77**, 2360 (1996).

[51] T. Ido, Y. Isoya, and H. Katori, "Optical-dipole trapping of Sr atoms at a high phase-space density," Phys. Rev. A **61**, 061403(R) (2000).

[52] L. P. Kadanoff and G. Baym, *Quantum Statistical Mechanics* (Addison-Wesley, Redwood City, 1989).

[53] M. Naraschewski and R. J. Glauber, "Spatial coherence and density correlations of trapped Bose gases," Phys. Rev. A **59**, 4595 (1999).

[54] I. Bloch, T. W. Hänsch and T. Esslinger, "Measurement of the spatial coherence of a trapped Bose gas at the phase transition," Nature **403**, 166 (2000).

[55] R. K. Pathria, *Statistical Mechanics* (Pergamon, Oxford, 1972).

[56] P. A. Ruprecht, M. J. Holland, K. Burnett, and M. Edwards, "Time-dependent solution of the nonlinear Shrödinger equation for Bose-condensed trapped neutral atoms," Phys. Rev. A **51**, 4704 (1995).

[57] G. Baym and C. J. Pethick, "Ground-state properties of magnetically trapped Bose-condensed Rubidium gas," Phys. Rev. Lett. **76**, 6 (1996).

[58] G. B. Arfken and H. J. Weber, *Mathematical Methods for Physicists, 4th Edition* (Academic Press, San Diego, 1995).

[59] D. L. Feder, M. S. Pindzola, L. A. Collins, B. I. Schneider, and C. W. Clark, "Dark soliton states of Bose-Einstein condensates in anisotropic traps," preprint, cond-mat/0004449.

[60] T. Winiecki, J. F. McCann, and C. S. Adams, "Vortex structures in dilute quantum fluids," Europhys. Lett. **48**, 475 (1999).

[61] R. J. Ballagh, K. Burnett, and T. F. Scott, "Theory of an output coupler for Bose-Einstein condensed atoms," Phys. Rev. Lett. **78**, 1607 (1997).

[62] H. Steck, M. Naraschewski, and H. Wallis, "Output of a pulsed atom laser," Phys. Rev. Lett. **80**, 1 (1998).

[63] W. Zhang and D. F. Walls, "Gravitational and collective effects in an output coupler for a Bose-Einstein condensate in an atomic trap," Phys. Rev. A **57**, 1248 (1998).

[64] L. I. Schiff, *Quantum Mechanics, 3rd Edition* (McGraw-Hill, Singapore, 1968).

[65] N. N. Bogoliubov, "On the theory of superfluidity," J. Phys. (USSR) **11**, 23 (1947).

[66] E. Zaremba, "Sound propagation in cylindrical Bose-condensed gases," Phys. Rev. A **57**, 518 (1998).

[67] S. Stringari, "Dynamics of Bose-Einstein condensed gases in highly deformed traps," Phys. Rev. A **58**, 2385 (1998).

[68] M. R. Andrews, D. M. Kurn, H. J. Miesner, D. S. Durfee, C. G. Townsend, S. Inouye, and W. Ketterle, "Propagation of sound in a Bose-Einstein condensate," Phys. Rev. Lett. **79**, 553 (1997).

[69] F. Dalfovo, S. Giorgini, M. Guillemas, L. Pitaevskii, and S. Stringari, "Collective and single-particle excitations of a trapped Bose gas," Phys. Rev. A **56**, 3840 (1997).

[70] A. P. Chikkatur, A. Gorlitz, D. M. Stamper-Kurn, S. Inouye, S. Gupta, and W. Ketterle, "Suppression and enhancement of impurity scattering in a Bose-Einstein condensate," Phys. Rev. Lett. **85**, 483 (2000).

[71] H. Lamb, *Hydrodynamics, 6th Edition* (CUP, Cambridge, 1932).

[72] K. W. Madison, F. Chevy, W. Wohlleben, and J. Dalibard, "Vortex formation in a stirred Bose-Einstein condensate," Phys. Rev. Lett. **84**, 806 (2000).

[73] K. W. Madison, F. Chevy, W. Wohlleben, and J. Dalibard, "Vortex lattices in a stirred Bose-Einstein condensate," preprint, cond-mat/0004037.

[74] B. P. Anderson, P. C. Haljan, C. E. Wieman, and E. A. Cornell, "Vortex precession in Bose-Einstein condensates: observations with filled and empty cores," preprint, cond-mat/0005368.

[75] F. Chevy, K. Madison, and J. Dalibard, "Measurement of the angular momentum of a rotating Bose-Einstein condensate," preprint, cond-mat/0005221.

[76] K. -P. Marzlin and W. Zhang, "Quantised circular motion of a trapped Bose-Einstein condensate: coherent rotation and vortices," Phys. Rev. A **57**, 4761 (1998).

[77] K. -P. Marzlin, W. Zhang, and E. M. Wright, "Vortex coupler for atomic Bose-Einstein condensates," Phys. Rev. Lett. **79**, 4728 (1997).

[78] E. L. Bolda and D. F. Walls, "Creation of vortices in a Bose-Einstein condensate by a Raman technique," Phys. Lett. A **246**, 32 (1998).

[79] R. Dum, J. I. Cirac, M. Lewenstein, and P. Zoller, "Creation of dark solitons and vortices in Bose-Einstein condensates," Phys. Rev. Lett. **80**, 2972 (1998).

[80] L. Dobrek, M. Gadja, M. Lewenstein, K. Sengstock, G. Birkl, and W. Ertmer, "Optical generation of vortices in trapped Bose-Einstein condensates," Phys. Rev. A **60**, R3381 (1999).

[81] S. Burger, K. Bongs, S. Dettmer, W. Ertmer, K. Senstock, A. Sanpera, G. V. Shylapnikov, and M. Lewenstein, "Dark solitons in Bose-Einstein condensates," Phys. Rev. Lett. **83**, 5198 (1999).

[82] J. Denschlag, J. E. Simsarian, D. L. Feder, C. W. Clark, L. A. Collins, J. Cubizolles, L. Deng, E. W. Hegley, K. Helmerson, W. P. Reinhardt, S. L. Rolston, B. I. Schneider, and W. D. Phillips, "Generating solitons by phase engineering of a Bose-Einstein condensate," Science **287**, 97 (2000).

[83] B. M. Caradoc-Davies, R. J. Ballagh, and K. Burnett, "Coherent dynamics of vortex formation in trapped Bose-Einstein condensates," Phys. Rev. Lett. **83**, 895 (1999).

[84] T. Frisch, Y. Pomeau, and S. Rica, "Transition to dissipation in a model of superflow," Phys. Rev. Lett. **69**, 1644 (1992).

[85] C. Huepe and M. -É. Brachet, "Solutions de nucléation tourbillonnaires dans un modèle d'écoulement superfluide," C. R. Acad. Sci. Ser. IIb: Mec., Phys., Chim., Astron. **325**, 195 (1997).

[86] T. Winiecki, J. F. McCann, and C. S. Adams, "Pressure drag in linear and nonlinear quantum fluids," Phys. Rev. Lett. **82**, 5186 (1999).

[87] P. W. Milonni in *Atomic, Molecular, and Optical Physics Handbook,* edited by G. W. F. Drake (AIP Press, New York, 1996).

[88] M. R. Andrews, M. -O. Mewes, N. J. van Druten, D. S. Durfee, D. M. Kurn, and W. Ketterle, "Direct, nondestructive observation of a Bose condensate," Science **273**, 84 (1996).

[89] E. Lundh, C. J. Pethick, and H. Smith, "Vortices in Bose-Einstein condensed atomic clouds," Phys. Rev. A **58**, 4816 (1998).

[90] F. Dalfovo and M. Modugno, "Free expansion of Bose-Einstein condensates with quantized vortices," Phys. Rev. A **61**, 023605 (2000).

[91] G. W. Rayfield and F. Reif, "Quantized vortex rings in superfluid helium," Phys. Rev. **136**, 1194 (1964).

[92] J. Stenger, S. Inouye, D. M. Stamper-Kurn, H. -J. Miesner, A. P. Chikkatur, and W. Ketterle, "Spin domains in ground-state Bose-Einstein condensates," Nature **396**, 345 (1998).

[93] H. -J. Miesner, D. M. Stamper-Kurn, J. Stenger, S. Inouye, A. P. Chikkatur, and W. Ketterle, "Observation of metastable states in spinor Bose-Einstein condensates," Phys. Rev. Lett. **82**, 2228 (1999).

[94] D. S. Hall, M. R. Matthews, C. E. Wieman, and E. A. Cornell, "Measurements of relative phase in two component Bose-Einstein condensates," Phys. Rev. Lett. **81**, 1543 (1998).

[95] D. S. Hall, J. R. Ensher, D. S. Jin, M. R. Matthews, C. E. Wieman, and E. A. Cornell, "Recent experiments with Bose-condensed gases at JILA," Proc. SPIE **3270**, 98 (1998).

[96] T. -L. Ho and V. B. Shenoy, "Binary mixtures of Bose condensates of alkali atoms," Phys. Rev. Lett. **77**, 3276 (1996).

[97] H. Pu and N. P. Bigelow, "Properties of two-species Bose condensates," Phys. Rev. Lett. **80**, 1130 (1998).

[98] B. D. Esry, C. H. Greene, J. P. Burke Jr., and J. L. Bohn, "Hartree-Fock theory for double condensates," Phys. Rev. Lett. **78**, 3594 (1997).

[99] C. K. Law, H. Pu, N. P. Bigelow, and J. H. Eberly, " 'Stability signature' in two-species dilute Bose-Einstein condensates," Phys. Rev. Lett. **79**, 3105 (1997).

[100] B. D. Esry and C. H. Greene, "Spontaneous spatial symmetry breaking in two-component Bose-Einstein condensates," Phys. Rev. A **59**, 1457 (1999).

[101] A. Smerzi and S. Fantoni, "Large amplitude oscillations of a Bose condensate," Phys. Rev. Lett. **78**, 3589 (1997).

[102] F. Dalfovo, C. Minniti, and L. P. Pitaevskii, "Frequency shift and mode coupling in the nonlinear dynamics of a Bose-condensed gas," Phys. Rev. A **56**, 4855 (1997).

[103] S. A. Morgan, S. Choi, K. Burnett, and M. Edwards, "Nonlinear mixing of quasiparticles in an inhomogeneous Bose condensate," Phys. Rev. A **57**, 3818 (1998).

[104] S. Choi, S. A. Morgan, and K. Burnett, "Phenomenological damping in trapped atomic Bose-Einstein condensates," Phys. Rev. A **57**, 4057 (1998).

[105] L. P. Pitaevskii and S. Stringari, "Landau damping in dilute Bose gases," Phys. Lett. A **235**, 398 (1997).

[106] W. V. Liu, "Theoretical study of the damping of collective excitations in a Bose-Einstein condensate," Phys. Rev. Lett. **79**, 4056 (1997).

[107] P. O. Fedichev, G. V. Shylapnikov, and J. T. M. Walraven, "Damping of low-energy excitations of a trapped Bose-Einstein condensate at finite temperatures," Phys. Rev. Lett. **80**, 2269 (1998).

[108] S. Giorgini, "Damping in dilute Bose gases: a mean-field approach," Phys. Rev. A **57**, 2949 (1998).

[109] D. S. Jin, M. R. Matthews, J. R. Ensher, C. E. Wieman, and E. A. Cornell, "Temperature-dependent damping and frequency shifts in collective excitations of a dilute Bose-Einstein condensate," Phys. Rev. Lett. **78**, 764 (1997).

[110] A. Sinatra, P. O. Fedichev, Y. Castin, J. Dalibard, and G. V. Shlyapnikov, "Dynamics of two interacting Bose-Einstein condensates," Phys. Rev. Lett. **82**, 251 (1999).

[111] E. A. Cornell (personal communication).

[112] L. D. Landau and E. M. Lifshitz, *Fluid Mechanics, 2nd Edition* (Pergamon, Oxford, 1987).

[113] R. J. Dodd, K. Burnett, M. Edwards, and C. W. Edwards, "Excitation spectroscopy of vortex states in dilute Bose-Einstein condensed gases," Phys. Rev. A **56**, 587 (1997).

[114] T. Isoshima and K. Machida, "Bose-Einstein condensation in a confined geometry with and without a vortex," J. Phys. Soc. Jpn. **66**, 3502 (1997).

[115] J. J. Garcia-Ripoll and V. M. Perez-Garcia, "Stability of vortices in inhomogeneous Bose condensates subject to rotation: a three-dimensional analysis," Phys. Rev. A **60**, 4864 (1999).

[116] A. A. Svidzinsky and A. L. Fetter, "Stability of a vortex in a trapped Bose-Einstein condensate," Phys. Rev. Lett. **84**, 5919 (2000).

[117] M. Linn and A. L. Fetter, "Stability of a vortex in a small trapped Bose-Einstein condensate," Phys. Rev. A **60**, 4910 (1999).

[118] D. S. Rokhsar, "Vortex stability and persistent currents in trapped Bose gases," Phys. Rev. Lett. **79**, 2164 (1997).

[119] P. O. Fedichev and G. V. Shlyapnikov, "Dissipative dynamics of a vortex state in a trapped Bose-condensed gas," Phys. Rev. A **60**, R1779 (1999).

[120] S. Sinha, "Semiclassical analysis of collective excitations in Bose-Einstein condensate," Phys. Rev. A **55**, 4325 (1997).

[121] A. A. Svidzinsky and A. L. Fetter, "Normal modes of a vortex in a trapped Bose-Einstein condensate," Phys. Rev. A **58**, 3168 (1998).

[122] Y. S. Kivshar, J. Christou, V. Tikhonenko, B. Luther-Davies, and L. M. Pismen, "Dynamics of optical vortex solitons," Opt. Commun. **152**, 198 (1998).

[123] D. L. Feder, C. W. Clark, and B. I. Schneider, "Vortex stability of interacting Bose-Einstein condensates confined in anisotropic harmonic traps," Phys. Rev. Lett. **82**, 4956 (1999).

[124] E. B. Sonin, "Vortex oscillations and hydrodynamics of rotating superfluids," Rev. Mod. Phys. **59**, 87 (1987).

[125] E. B. Sonin, "Magnus force in superfluids and superconductors," Phys. Rev. B **55**, 485 (1997).

[126] Y. N. Ovchinnikov and I. M. Sigal, "Long-time behaviour of Ginzburg-Landau vortices," Nonlinearity **11**, 1295 (1998).

[127] E. A. Cornell, "Quantum meteorology: dynamics of a BEC vortex," presentation at "Workshop on rotating Bose-Einstein condensates," Trento, Italy, June 11-13, 2000.

[128] P. H. Roberts and J. Grant, "Motions in a Bose condensate I. The structure of a large circular vortex," J. Phys. A: Gen. Phys. **4**, 55 (1971).

[129] L .M. Pismen and A. A. Nepomnyashchy, "Stability of vortex rings in a model of superflow," Physica D **69**, 163 (1993).

[130] T. Isoshima and K. Machida, "Vortex stabilization in Bose-Einstein condensate of alkali-metal atom gas," Phys. Rev. A **59**, 2203 (1999).

[131] F. Zambelli and S. Stringari, "Quantised vortices and collective oscillations of a trapped Bose-Einstein condensate," Phys. Rev. Lett. **81**, 1754 (1998).

[132] O. M. Maragò, S. A. Hopkins, J. Arlt, E. Hodby, G. Hechenblaikner, and C. J. Foot, "Observation of the scissors mode and evidence for superfluidity of a trapped Bose-Einstein condensed gas," Phys. Rev. Lett. **84**, 2056 (2000).

[133] V. Hakim, "Nonlinear Schrödinger flow past an obstacle in one dimension," Phys. Rev. E **55**, 2835 (1997).

[134] R. Onofrio, C. Raman, J. M. Vogels, J. Abo-Shaeer, A. P. Chikkatur, and W. Ketterle, "Observation of superfluid flow in a Bose-Einstein condensed gas," preprint, cond-mat/0006111.

[135] C. Nore, C. Huepe, and M. E. Brachet, "Subcritical dissipation in three-dimensional superflows," Phys. Rev. Lett. **84**, 2191 (2000).

[136] P. O. Fedichev and G. V. Shlyapnikov, "Critical velocity in cylindrical Bose-Einstein condensates," preprint, cond-mat/0004039.

[137] M. Crescimanno, C. G. Koay, R. Peterson, and R. Walsworth, "Analytical estimate of the critical velocity for vortex pair creation in trapped Bose condensates," preprint, cond-mat/0001163.

[138] C. A. Jones and P. H. Roberts, "Motions in a Bose condensate: IV. Axisymmetric solitary waves," J. Phys. A: Math. Gen. **15**, 2599 (1982).

[139] J. S. Stiessberger and W. Zwerger, "Critical velocity of superfluid flow past large obstacles in Bose-condensates," preprint, cond-mat/0006419.

[140] P. I. Soininen and N. B. Kopnin, "Stability of superflow," Phys. Rev. B **49**, 12087 (1994).

[141] I. Aranson and V. Steinberg, "Spin-up and nucleation of vortices in superfluid ^{4}He," Phys. Rev. B **54**, 13072 (1996).

[142] C. Josserand, Y. Pomeau, and S. Rica, "Vortex shedding in a model of superflow," Physica D **134**, 111 (1999).

[143] C. Huepe and M. -E. Brachet, "Scaling laws for vortical nucleation solutions in a model of superflow," Physica D **140**, 126 (2000).

[144] T. Winiecki, B. Jackson, J. F. McCann, and C. S. Adams, "Vortex shedding and drag in dilute Bose-Einstein condensates," J. Phys. B: At. Mol. Opt. Phys. **33**, 4069 (2000).

[145] A. C. Newell and Y. Pomeau, "Phase diffusion and phase propagation: interesting connections," Physica D **87**, 216 (1995).

[146] C. Bowman and A. C. Newell, "Natural patterns and wavelets," Rev. Mod. Phys. **70**, 289 (1998).

[147] L. M. Pismen, *Vortices in Nonlinear Fields* (Oxford University Press, Oxford, 1999).

[148] E. Zaremba, T. Nikuni, and A. Griffin, "Dynamics of trapped Bose gases at finite temperatures," J. Low Temp. Phys. **116**, 277 (1999).

[149] A. Griffin, "Conserving and gapless approximations for an inhomogeneous Bose gas at finite temperatures," Phys. Rev. B **53**, 9341 (1996).

[150] D. A. W. Hutchinson, E. Zaremba, and A. Griffin, "Finite temperature excitations of a trapped Bose gas," Phys. Rev. Lett. **78**, 1842 (1997).

[151] R. J. Dodd, M. Edwards, C. W. Clark, and K. Burnett, "Collective excitations of Bose-Einstein-condensed gases at finite temperatures," Phys. Rev. A **57**, R32 (1998).

[152] R. J. Dodd, K. Burnett, M. Edwards, and C. W. Clark, "Trapped Bose-Einstein condensates at finite temperature: a two-gas model," Acta Physica Polonica A **93**, 45 (1998).

[153] T. Bergeman, D. L. Feder, N. L. Balazs, and B. I. Schneider, "Bose condensates in a harmonic trap near the critical temperature," Phys. Rev. A **61**, 063605 (2000).

[154] D. A. W. Hutchinson, R. J. Dodd, and K. Burnett, "Gapless finite-T theory of collective modes of a trapped gas," Phys. Rev. Lett. **81**, 2198 (1998).

[155] N. P. Proukakis, S. A. Morgan, S. Choi, and K. Burnett, "Comparison of gapless mean field theories for trapped Bose-Einstein condensates," Phys. Rev. A **58**, 2435 (1998).

[156] S. A. Morgan, "A gapless theory of Bose-Einstein condensation in dilute gases at finite temperatures," J. Phys. B: At. Mol. Opt. Phys. **33**, 3847 (2000).

[157] J. F. Dobson, "Harmonic-potential theorem—implications for approximate many-body theories," Phys. Rev. Lett. **73**, 2244 (1994).

[158] D. M. Stamper-Kurn, H. J. Miesner, S. Inouye, M. R. Andrews, and W. Ketterle, "Collisionless and hydrodynamic excitations of a Bose-Einstein condensate," Phys. Rev. Lett. **81**, 500 (1998).

[159] S. Giorgini, L. P. Pitaevskii, and S. Stringari, "Thermodynamics of a trapped Bose-condensed gas," J. Low Temp. Phys. **109**, 309 (1997).

[160] M. Holzmann, W. Krauth, and M. Naraschewski, "Precision Monte Carlo test of the Hartree-Fock for a trapped Bose gas," Phys. Rev. A **59**, 2956 (1999).

[161] M. Naraschewski and D. M. Stamper-Kurn, "Analytical description of a trapped semi-ideal Bose gas at finite temperatures," Phys. Rev. A **58**, 2423 (1998).

[162] J. R. Ensher, D. S. Jin, M. R. Matthews, C. E. Wieman, and E. A. Cornell, "Bose-Einstein condensation in a dilute gas: measurement of energy and ground-state occupation," Phys. Rev. Lett. **77**, 4984 (1996).

[163] M. J. Bijlsma and H. T. C. Stoof, "Collisionless modes of a trapped Bose gas," Phys. Rev. A **60**, 3973 (1999).

[164] E. Zaremba, A. Griffin, and T. Nikuni, "Two-fluid hydrodynamics for a trapped weakly interacting Bose gas," Phys. Rev. A **57**, 4695 (1998).

[165] T. Nikuni, E. Zaremba, and A. Griffin, "Two-fluid dynamics for a Bose-Einstein condensate out of local equilibrium with the noncondensate," Phys. Rev. Lett. **83**, 10 (1999).

[166] T. Nikuni, A. Griffin, and E. Zaremba, "Two-fluid hydrodynamics of a Bose gas including damping from normal fluid transport coefficients," preprint, cond-mat/9911336.

[167] O. J. Luiten, M. J. Reynolds, and J. T. M. Walraven, "Kinetic theory of the evaporative cooling of a trapped gas," Phys. Rev. A **53**, 381 (1996).

[168] M. Holland, J. Williams, and J. Cooper, "Bose-Einstein condensation: kinetic evolution obtained from simulated trajectories," Phys. Rev. A **55**, 3670 (1997).

[169] D. W. Snoke and J. P. Wolfe, "Population dynamics of a Bose gas near saturation," Phys. Rev. B **39**, 4030 (1989).

[170] D. V. Semikoz and I. I. Tkachev, "Kinetics of Bose condensation," Phys. Rev. Lett. **74**, 3093 (1995).

[171] M. J. Bijlsma, E. Zaremba, and H. T. C. Stoof, "Condensate growth in trapped Bose gases," preprint, cond-mat/0001323.

[172] T. Lopez-Arias and A. Smerzi, "Kinetic properties of a Bose-Einstein gas at finite temperature," Phys. Rev. A **58**, 526 (1998).

[173] H. Wu and C. J. Foot, "Direct simulation of evaporative cooling," J. Phys. B: At. Mol. Opt. Phys. **29**, L321 (1996).

[174] H. Wu, E. Arimondo, and C. J. Foot, "Dynamics of evaporative cooling for Bose-Einstein condensates"- Phys. Rev. A **56**, 560 (1997).

[175] G. A. Bird, *Molecular gas dynamics and the direct simulation of gas flows* (OUP, Oxford, 1994).

[176] J. E. Williams and A. Griffin, "New damping mechanism of collective excitations at finite temperatures in the collisionless region," preprint, cond-mat/0003481.

[177] M. Guilleumas and L. P. Pitaevskii, "Temperature-induced resonances and Landau damping of collective modes in Bose-Einstein condensed gases in spherical traps," Phys. Rev. A **61**, 013602 (2000).

[178] J. Reidl, A. Csordás, R. Graham, and P. Szépfalusy, "Shifts and widths of collective excitations in trapped Bose gases determined by the dielectric formalism," Phys. Rev. A **61**, 043606 (2000).

[179] W. H. Press, S. A. Teukolsky, W. T. Vetterling, and B. P. Flannery, *Numerical Recipes in FORTRAN, 2nd Edition* (Cambridge University Press, Cambridge, 1992).